

CHARACTERISING GAS HYDRATE DEPOSITS ON NEW
ZEALAND'S SOUTHERN HIKURANGI MARGIN USING
SEISMIC REFLECTION DATA

Hanyan Wang

A thesis submitted in partial fulfilment of requirements for the

Degree of Masters in Petroleum Geoscience

2016

School of Geography, Environment and Earth Science

Victoria University of Wellington

Abstract

Reprocessed Bruin 2D seismic data (recorded in 2006) from New Zealand Hikurangi Margin are presented and analyzed to show the presence of gas hydrates. We choose six seismic lines that each showed bottom-simulating reflections (BSRs) that are important indicators for the presence of gas hydrate. The aim is to obtain a higher resolution image of the shallow subsurface structures and determine the nature of the gas hydrate system in this area.

To further investigate the presence of Gas Hydrates was undertaken. There is a strong correlation between anomalous velocities and the depths of BSRs, which supports the presence of gas hydrates in the research area and is useful for detecting areas of both free gas and gas hydrate along the seismic lines.

The combination of high-resolution seismic imaging and velocity analysis is the key method for showing the distribution of gas hydrates and gas pockets in our research area. The results indicate that the distribution of both free gas and gas hydrate is strongly localized. The Discussion Chapter gives several concentrated gas hydrate deposits in the research area. Idealized scenarios for the formation of the gas hydrates are proposed. In terms of identifying concentrated gas hydrate deposits we propose the identification of the following key seismic attributes: 1) existence of BSRs, 2) strong reflections above BSRs in the gas hydrate stability zone, 3) enhanced reflections related to free gas below BSRs, 4) appropriate velocity anomalies (i.e. low velocity zones beneath BSRs and localized high-velocity zones above BSRs).

This study contributes to the understanding of the geological conditions and processes that drives the deposition of concentrated gas hydrate deposits on this part of the Hikurangi Margin.

Acknowledgements

Throughout the course of this research, I have had the pleasure of knowing a number of people who made contribution to my research. It is a pleasure to convey my gratitude to them all in my acknowledgements.

I would like to thank my supervisors, Prof. Tim Stern and Dr. Gareth Crutchley for their supervision and encouragement during the course of this study. I would like to thank Dr. Gareth Crutchley for his supervision, advice and guidance. He has been patient to explain and answer all my questions about gas hydrate and seismic processing. I also would like to acknowledge Prof. Tim Stern for providing me invaluable encouragement and support during my Master study. His advice and reviews have contributed greatly to improve this project.

I would like to thank many people from GNS for their time; Suzanne Bull and Hai Zhu for their invaluable advice and discussion on the seismic interpretation.

I would like to thank many people from Victoria University of Wellington; Dr. Dave Bennett and Dr. Warren Dickinson for their discussion and their invaluable advices. I would also acknowledge Ningsheng Wang and Kate King for their support and help.

And finally, I wish to thank my family for their support and understanding. They have given me courage and support to pursue my dreams. I also would like to thank my girlfriend, Lei who has supported me during the two years of my Master study.

Table of Contents

1	THESIS STRUCTURE.....	1
2	INTRODUCTION	2
2.1	What are gas hydrates?.....	2
2.1.1	Chemical architecture	2
2.1.2	Brief history and development of gas hydrates	3
2.1.3	Gas hydrate stability zone	4
2.1.4	Importance of gas hydrate.....	6
2.2	Seismic expressions of gas hydrates	9
2.2.1	Enhanced and blanking seismic reflection.....	11
2.3	Gas hydrate in New Zealand	12
2.4	Objectives of this study.....	13
3	GEOLOGICAL SETTING	14
3.1	Tectonic setting of Hikurangi Margin	14
3.2	Tectonic-sediment interaction	15
3.3	Gas hydrate system.....	16
3.3.1	Source rocks	16
3.3.2	Reservoirs.....	16
4	METHODOLOGY	18
4.1	Data acquisition.....	18
4.2	Data processing	21
4.2.1	Introduction.....	21
4.2.2	Multichannel seismic data processing	21

4.2.3	Seismic velocity analysis	26
5	RESULTS	31
5.1	Distribution of BSRs	31
5.2	Observation of BR05-37	32
5.3	Observation of BR05-33	32
5.4	Observation of BR05-27	32
5.5	Observation of BR05-23	33
5.6	Observation of BR05-19	33
5.7	Observation of BR05-02	45
5.7.1	Section 1 (CDP 746-3394) of BR05-02	45
5.7.2	Section 2 (CDP 3395-6043) of BR05-02	45
5.7.3	Section 3 (CDP 6044-8692) of BR05-02	46
5.7.4	Section 4 (CDP 8693-11341) of BR05-02	46
5.7.5	Section 5 (CDP 11342-14186) of BR05-02	46
6	DISCUSSION	55
6.1	Double-BSRs system.....	55
6.2	Indication of concentrated gas hydrate deposits	57
6.3	Importance of dipping strata and faulting in the formation of gas hydrate ...	59
6.3.1	Dipping strata	59
6.3.2	Faulting	60
6.4	Distinguishing gas hydrate-derived velocity anomalies from lithologically- derived anomalies	61
6.5	Gas Hydrate deposits in turbidite sequences.....	63
6.6	Blanking zone and amplitude variation.....	64

6.7	Idealized scenarios for the formation of concentrated gas hydrate	65
7	CONCLUSIONS.....	69
8	REFERENCE.....	72

Table of Figures

Figure 2.1:	Natural gas hydrate structures after Sloan and Koh (2008).	3
Figure 2.2:	Gas hydrate stability zone	5
Figure 2.3:	Distribution of known gas hydrate accumulations	6
Figure 2.4:	Cartoon of geophysical features related to gas hydrate.....	7
Figure 2.5:	A classic example of a BSR from Blake Ridge, east of Savannah, Georgia, USA.....	10
Figure 2.6:	Schematic of seismic amplitude response to free gas and gas hydrate-bearing sands as a function of gas or gas hydrate saturation	12
Figure 2.7:	Location map of Bruin seismic survey 2005.	13
Figure 3.1:	Diagram describing the tectonic setting of Hikurangi.....	15
Figure 4.1:	Base map of Bruin 2005 seismic survey.....	18
Figure 4.2:	Acquisition geometry of Bruin 2005 seismic survey	20
Figure 4.3:	Processing geometry of Line BR05-33.	22
Figure 4.4:	Variable area wiggle display of shot 1662.....	23
Figure 4.5:	Comparison between near trace stacked seismic section and seismic section after post-stack time migration.	24
Figure 4.6:	Comparison between original industry-processed seismic section and our reprocessed seismic section after pre-stack time migration.....	25
Figure 4.7:	Preparation for automatic velocity picking	28
Figure 4.8:	Converting stacking velocities to interval velocities.....	30
Figure 5.1:	The base map shows the distribution and amplitudes of BSRs on the chosen seismic lines.	31

Figure 5.2: High-resolution velocity analysis from BR05-37.	34
Figure 5.3: High-resolution velocity analysis from zoomed in zone of Figure 5.2.	35
Figure 5.4: High-resolution velocity analysis from BR05-33.	36
Figure 5.5: High-resolution velocity analysis from left red box in Figure 5.4 (Line BR05-33).....	37
Figure 5.6: High-resolution velocity analysis from right red box in Figure 5.4 (Line BR05-33).....	38
Figure 5.7: High-resolution velocity analysis from BR05-27.	39
Figure 5.8: High-resolution velocity analysis from zoomed in part of Figure 5.7 (Line BR05-27).....	40
Figure 5.9: High-resolution velocity analysis from BR05-23.	41
Figure 5.10: High-resolution velocity analysis from zoomed in part of Figure 5.9 (Line BR05-23).....	42
Figure 5.11: High-resolution velocity analysis from BR05-19.....	43
Figure 5.12: High-resolution velocity analysis from red box in Figure 5.11 (Line BR05-19).	44
Figure 5.13: High-resolution velocity analysis from BR05-02 section 1.	47
Figure 5.14: High-resolution velocity analysis from the red box in Figure 5.13 (part of BR05-02 section 1).	48
Figure 5.15: High-resolution velocity analysis from BR05-02 section 2.	49
Figure 5.16: High-resolution velocity analysis from red box in Figure 5.15 (part of BR05-02 section 2).	50
Figure 5.17: High-resolution velocity analysis from BR05-02 section 3.	51
Figure 5.18: High-resolution velocity analysis from red box in Figure 5.17 (part of BR05-02 section 3).	52
Figure 5.19: High-resolution velocity analysis from BR05-02 section 4.	53
Figure 5.20: High-resolution velocity analysis from BR05-02 section 5.	54
Figure 6.1: Double-BSRs system from BR05-37.	56

Figure 6.2: Interpreted concentrated gas hydrate deposit at an anticline structure on Line BR05-27.	58
Figure 6.3: Gas hydrate system in dipping strata of Line BR05-33.	59
Figure 6.4: Gas hydrate system at a fold structure on Line BR05-02.....	61
Figure 6.5: Gas hydrate at an anticline structure on Line BR05-33.	62
Figure 6.6: Gas hydrate system in turbidite deposits from BR05-02.	64
Figure 6.7: Concentrated gas hydrate deposit and low saturation gas hydrate deposits from BR05-23.	65
Figure 6.8: Cartoon for the formation of concentrated gas hydrate deposits that are based on Figure 6.3.	66
Figure 6.9: Cartoon for the formation of concentrated gas hydrate deposits within folded sediments characterised by flexural extensional faulting (based on observations in Figure 6.4).	67
Figure 7.1: The main gas hydrate deposition styles that we identified in our research region and their corresponding seismic expressions.....	71

1 THESIS STRUCTURE

Chapter 2 (Introduction) introduces gas hydrates provides background on the topic of gas hydrates in marine sediments, and gives description of seismic manifestations of gas hydrates, including bottom-simulating reflections (BSRs). Lastly, this chapter outlines the objectives for this thesis.

Chapter 3 (Geological Setting) outlines the tectonic setting of the Hikurangi margin and describes the depositional sequence including potential reservoirs for gas hydrates. This chapter also describes the tectonic-sediment interactions across the Hikurangi margin.

Chapter 4 (Methodology) gives an introduction to the seismic data and include the details for the acquisition system and parameters of the seismic data. This chapter also describes the methods of processing the multichannel seismic data. This includes the methods of high resolution velocity analysis that used to detect concentrated deposits of gas hydrates and the free gas beneath the hydrates.

Chapter 5 (Results) presents the distribution of BSRs over the study area, the processed seismic data and the results of high resolution velocity analysis.

Chapter 6 (Discussion) Interpretations of the results given in Chapter 5 are given and promising locations for concentrated gas hydrate deposits are indicated.

Chapter 7 (Conclusions) summarises the key findings of the thesis.

Chapter 8 References

2 INTRODUCTION

2.1 What are gas hydrates?

2.1.1 *Chemical architecture*

A gas hydrate is a solid clathrate compound in which a large amount of methane is trapped within a crystal structure of water, forming a solid similar to ice. Gas hydrates are stable at relatively low temperature and high pressure in the presence of sufficient methane and water. The crystal lattice of gas hydrates are an efficient gas storage unit; 1m³ of gas hydrate can contain up to 164 m³ of methane gas at standard conditions (Kvenvolden, 1993).

Gas hydrates normally have two basic crystal structures: Structure I and Structure II (Figure 2.1 A and B) (Kvenvolden, 1993). Structure I is a body-centered cubic structure, made up by small natural gas molecules, consequently, this kind of gas hydrates is formed from the biogenic gases containing mostly methane (Yamamoto, 2013). Structure II has a diamond-shaped lattice within a cubic framework, formed by natural gases or oil containing molecules larger than ethane but smaller than pentane. Structure II hydrates are believed to form from thermogenic gas sources (Boswell, 2013). A new hydrate structure was discovered and called Structure H (Figure 2.1C) in 1987 (Sassen and MacDonald, 1994). Structure H hydrates are rarely discovered in nature, but are known to exist in the Gulf of Mexico, where they are associated with the active vertical migration of oil and gas to the sea floor within the gas hydrate stability zone (Sassen and MacDonald, 1994; Sassen et al., 2001).

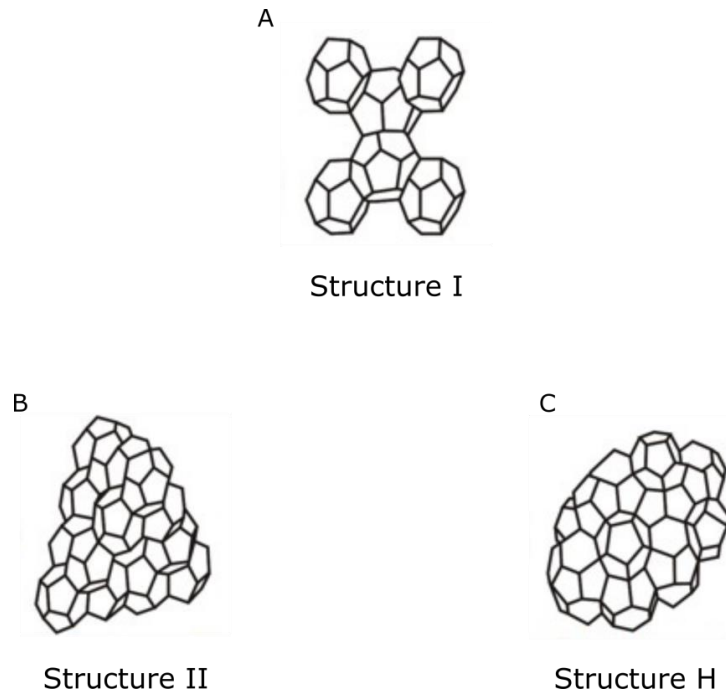


Figure 2.1: Natural gas hydrate structures after Sloan and Koh (2008). A) Structure I. The unit cell is a 12 Å cube consisting of 46 water molecules which surround two small pentagonal dodecahedra (5^{12}) cavities and six large tetradecahedra ($5^{12}6^2$) cavities. B) Structure II. The unit cell is a 17.3 Å cube with 136 water molecules that surround 16 small distorted 5^{12} cavities and 8 larger hexadecahedra ($5^{12}6^4$) cavities. C) Structure H. The unit cell is a hexagonal lattice with parameters $a = 12.26$ Å and $c = 10.17$ Å. It is formed from 34 water molecules that surround three different types of cavities: three small 5^{12} cavities, two medium irregular dodecahedra ($4^35^66^3$) cavities, and one large icosahedron ($5^{12}6^8$) cavity.

2.1.2 Brief history and development of gas hydrates

The history of our understanding of gas hydrates dates back to initial laboratory experiments carried out by Joseph Priestly in 1778 involving SO_2 and water at atmospheric pressure and low temperature (Makogon, 1981). Later (in 1881), Humphrey Davy discovered that by mixing chlorine gas with water under low temperature a solid gas hydrate substance was formed, which they called chlorine clathrate hydrate (Makogon, 1981). It wasn't until the 1930s that natural gas hydrate was given much attention, when the ice-like substance was considered a nuisance as it clogged oil and gas pipelines (Hammerschmidt, 1934). More recently, gas hydrate itself has been explored around the world for its potential as an alternative energy resource. Gas hydrates have been observed in variable geological environments, but it is thought that commercial gas hydrate reservoirs should be hosted in high-quality and highly

permeable sands, just as the case for conventional hydrocarbon reservoirs (Shipley, 1979). The most important recent news of gas hydrate development was the successful production test, which was operated by Japan in the Nankai Trough in 2013 (Boswell, 2013). This experiment showed that the production of gas from gas hydrate-bearing sediment is now technically feasible and that depressurization is an appropriate method for producing gas from the gas hydrate-bearing sediments. However, a few days after the testing began the production was terminated by the increase of sand production (Boswell, 2013).

2.1.3 Gas hydrate stability zone

Gas hydrate stability zone (GHSZ) is an environment with low temperature and high pressure. The appropriate low temperature is controlled by the circulation of ocean and the heat flow that are dependent on the tectonic setting. The gas hydrate stability zone in sediments can be delineated on a temperature versus pressure profile (Figure 2.2 A) with respect to the hydrothermal gradient, geothermal gradient and gas hydrate phase boundary of the particular environment. The position of gas hydrate phase boundary is primarily dependent on the composition of gas, but may also be controlled by pore fluid composition, pore size and possibly sediment mineralogy (Mestdagh, 2015). However, as the composition of gas is often not known, the position of the phase boundary is generally calculated under hydrostatic pressures for pure methane (CH_4) gas and seawater (Crutchley, 2009). Hydrothermal gradients (decrease with increasing water depth) and geothermal gradients (increase with increase subsurface depth) are locality variable, and can differ markedly with geographical location and tectonic setting. Therefore, the location of GHSZ is various around the world. In our study region the depth of GHSZ is 650 mbsl to ~2500 mbsl. This equates to a thickness of GHSZ in sediments of 0 to ~500 m.

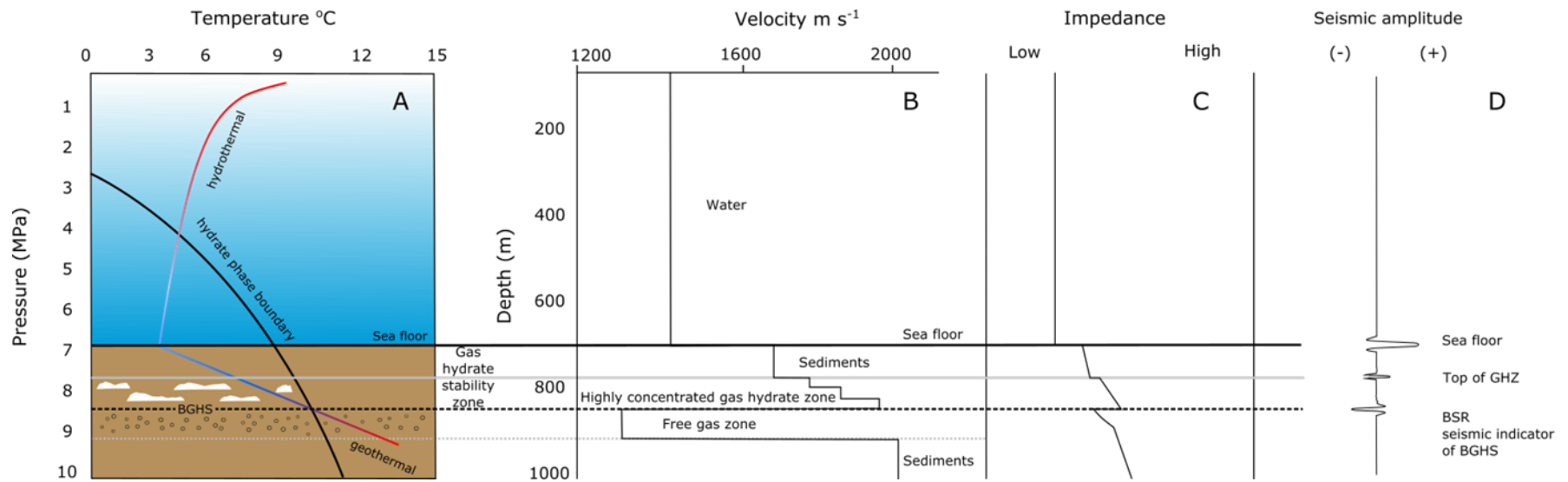


Figure 2.2: Gas hydrate stability zone. A) Profile of gas hydrate stability zone with respect to temperature and pressure in the marine environment, modified from Crutchley's figure (Crutchley, 2009). Gas hydrate phase boundary (black line) calculated for pure methane (CH₄). To left of the phase boundary curve is where the gas hydrate is stable. The red to blue gradient line is hydrothermal gradient in water column and geothermal gradient beneath the sea floor (horizontal black solid line). The black dashed line is the intersection of the geothermal gradient and the phase boundary curve, which marks the BGHS (base of gas hydrate stability). The region between the sea floor and the BGHS is the gas hydrate stability zone (GHSZ) within the sediments. B) A representation of a velocity model for gas hydrate deposits from the profile in (A). The velocity is constant for the water column. The velocity increases beneath the sea floor in sediments. The velocity increases markedly in highly concentrated gas hydrate zones as hydrate increases the propagation velocity of seismic wave. At the BGHS, the velocity decreases due to the existence of free gas in sediment. Finally, the velocity increases again in the sediment beneath the free gas zone. C) A schematic representation of impedance from profile (B), assuming constant impedance throughout water column. A strong positive impedance step occurs at sea floor, where density and velocity increase. Another positive step below represents the top of a (theoretical) highly-concentrated gas hydrate zone. The negative step is shown at the BGHS due to the reduction in velocity due to free gas. D) Schematic representation of a seismic trace with the impedance contrast shown in (C). A strong reflection forms at the sea floor and also at the BGHS. The reflection at the BGHS is of opposite polarity to the sea floor reflection. The reflection for the top of highly concentrated gas hydrate zone is reflectively weaker than the reflection of the sea floor due to the change in impedance being smaller.

2.1.4 Importance of gas hydrate

Most gas hydrate-related research focuses around three sectors:

1. The potential of gas hydrate as an alternative energy resource to conventional hydrocarbon deposits.
2. The importance of gas hydrates with respect to global climate change, as gas hydrate deposits contain huge amounts of the greenhouse gas CH_4 .
3. The implicated role of gas hydrates in continental slope stability and failure of sediments.

2.1.4.1 The potential of gas hydrates as energy resource

The distribution of gas hydrate is restricted to submarine sections of continental margins, onshore permafrost zones, and sedimentary sections beneath deep lakes because of the temperature and pressures requirements (Figure 2.3) (Kvenvolden and Rogers, 2005). However, detailed geological knowledge of the concentration of gas hydrate in sediments is limited. This leads to considerable uncertainty in estimations of the global gas hydrate resource (Klauda and Sandler, 2005; Kvenvolden et al., 1998; Milkov, 2004). However, according to Sloan's results (Sloan, 2003), even the most conservative estimates suggest that the amount of energy in hydrates is twice than that of all other fossil fuels combined.

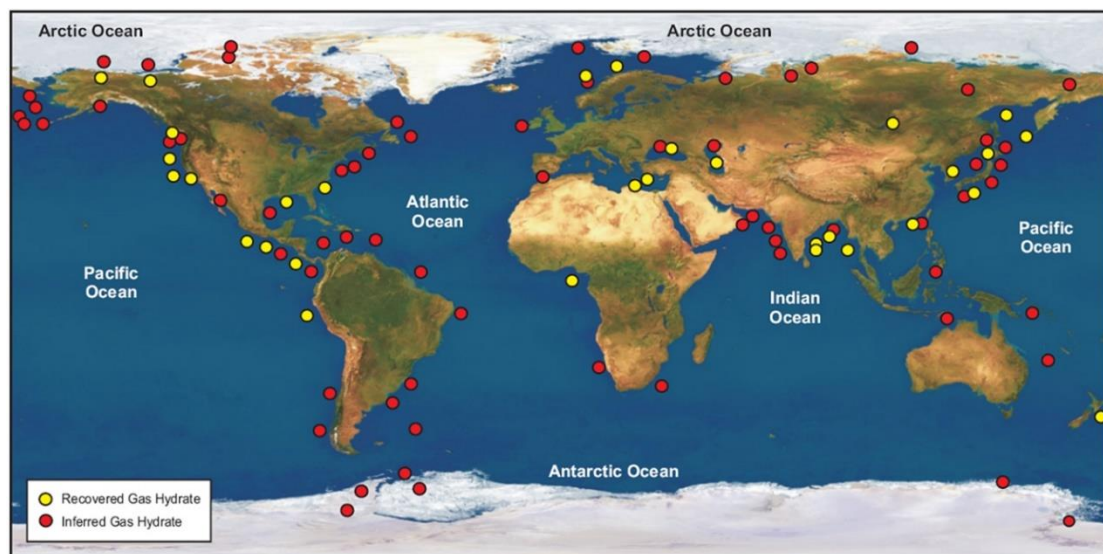


Figure 2.3: Distribution of known gas hydrate accumulations (courtesy of Council of Canadian Academies (2008), after Kvenvolden and Rogers (2005).

Geophysical features commonly observed in the shallow subsurface and their relationship to prospectivity for gas hydrate as an energy resource are shown in Figure 2.4, after (Boswell et al., 2014).

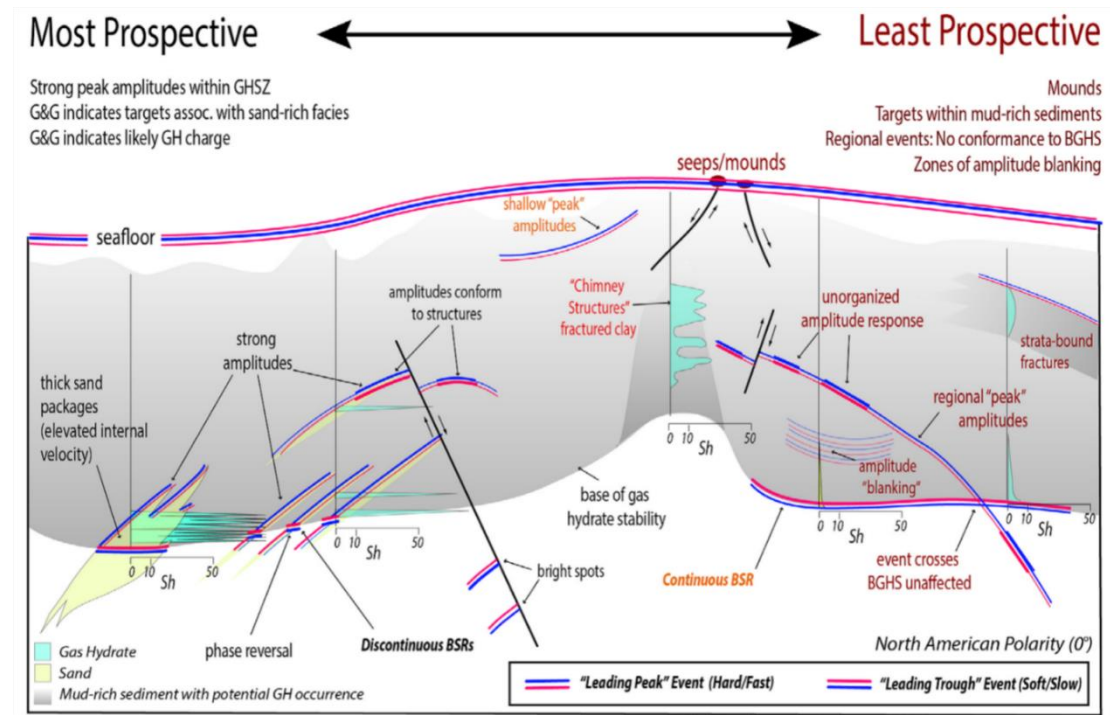


Figure 2.4: Cartoon of geophysical features commonly observed in the shallow subsurface and their relationship to prospectivity for gas hydrate resource evaluation (after Boswell et al. 2014).

Highly prospective gas hydrate deposits are expected to show polarity reversals, where seismic events cross BSRs. The resource potential of a given gas hydrate deposit is enhanced by the occurrence of sand-rich deepwater depositional facies (Boswell et al., 2014).

The current primary challenge in the development of gas hydrate as an energy resource is how to produce gas from gas hydrate with commercial methods. Methods for economic recovery of gas from gas hydrates normally follow these principles:

- 1) Decreasing the pressure below that of hydrate stability. For example, the method of depressurization was used by Japan Oil, Gas and Metal Corporation (JOGMC) in their successful gas hydrate production test (2013) in Nankai Trough (Boswell, 2013).
- 2) Increasing the temperature above that of hydrate stability by injecting hot water or steam into gas hydrate reservoir (Dallimore et al., 2005)

3) Using other molecules such as CO₂ and N₂ to replace the molecule of CH₄ within hydrates, for example, the ConocoPhillips gas hydrate production test that was completed in 2012 (Schoderbek et al., 2013).

Currently, the feasibility of the method of depressurization has been demonstrated by the production test conducted by JOGMEC in 2013 (Boswell, 2013). Furthermore, numerical simulations conducted in both the United States and Japan have shown that conventional well bores penetrating sand reservoirs can be used effectively to dissociate methane hydrate and gather the released methane at rates suitable for commercial production (USDE, 2011). However, the real wells for production of gas hydrate will be more complicated than most conventional gas wells (USDE, 2011).

2.1.4.2 Climate change

Methane (CH₄) is an important greenhouse gas and the release of large amounts of methane into the atmosphere could cause global warming, as the effect of one molecule of CH₄ is ~25 times that of one CO₂ molecule (Lelieveld et al., 1998). A change in the environment, such as increasing temperature or decreasing pressure, can induce the dissociation of hydrate, releasing methane gas from hydrate. A possible relationship between global warming at 15,000 years ago and methane gas released from hydrates was suggested by some publications (Kennett et al., 2003) and this is commonly called “the clathrate gun hypothesis”. Two primary mechanisms, including large slope failure events and background seepage, for free methane escaping into the atmosphere were proposed (Haq, 2000; Kvenvolden and Rogers, 2005). However, the evidence for methane from dissociating gas hydrate reaching the atmosphere is limited. Most of the places that atmospheric methane is observed are associated with the source of a petroleum system rather than a methane hydrate system (Sassen et al., 2001).

2.1.4.3 Submarine sediment failure

The most compelling concept for explaining the link between gas hydrate and the failure of submarine sediments is based on high pore fluid pressure induced by the release of gas and water from dissociation of gas hydrates (Sultan et al., 2004; Xu and Germanovich, 2006). The mechanism of failure can be well explained by Coulomb

failure criterion (King et al., 1994), which is described by normal stress and pore fluid pressure. Various environmental changes, including fall of sea level, tectonic uplift and ocean warming can influence the stability of a GHSZ, and thus cause the dissociation of gas hydrates. The effective normal stress is decreased, in parallel with an increase in fluid pressure, which is the result of dissociation of gas hydrate. This means that a smaller shear stress is required to trigger slopes to failure. Around the world, a number of submarine landslides have been associated with gas hydrate deposits. For example, Rock Garden, east of New Zealand's North Island, shows a remarkably flat top and this has been suggested to result from a cyclic fracturing mechanism in response to repeated hydrate association and dissociation (Pecher et al., 2005).

The strength of sediment hosting gas hydrates is greater than those that are free of hydrate or containing free gas due the increase in the friction coefficients that is a function of hydrate concentration (Sultan et al., 2007; Zhang et al., 1999). The presence of gas hydrate in sediments will make the sediments more resistant failure.

2.2 Seismic expressions of gas hydrates

Seismic Reflection techniques are often useful. Many gas hydrate studies are based on bottom simulating reflections (BSRs) (Figure 2.5), which is an important geophysical indicator of gas hydrate. Seismic reflections are generated by acoustic impedance contrasts (Figure 2.2 C) that are differences across horizons in the product of acoustic velocity and density. For near vertical ray paths the seismic reflection amplitude is only dependent on the P-wave speeds and density of each layer, but for non-zero incidence angles the amplitude of seismic reflections is a complex function of P and S-wave speeds, and densities, as described by the Zoepritz equations (Shuey, 1985).

Generally, impedance contrasts can represent the boundaries between different sedimentary units, for example, a lower density sandstone overlying a higher density mudstone. According to Sloan (1998) the P-wave velocity (V_p) of pure gas hydrate is $\sim 3300 \text{ ms}^{-1}$. This means that the presence of gas hydrate will make the V_p of sediment bearing gas hydrate higher than that of surrounding sediments. Consequently, sediments directly above the BGHS (bottom of gas hydrate stability zone) usually show

significantly higher impedance than those directly below the BGHS, which results in a significant impedance contrast across the BGHS, that generates the BSR (Figure 2.2 C and Figure 2.5).

The sea floor generates a positive impedance contrast while the BSR generates a negative impedance contrast. Therefore, compared to the sea floor reflection, a BSR will show a reversed waveform polarity (Figure 2.2 D).

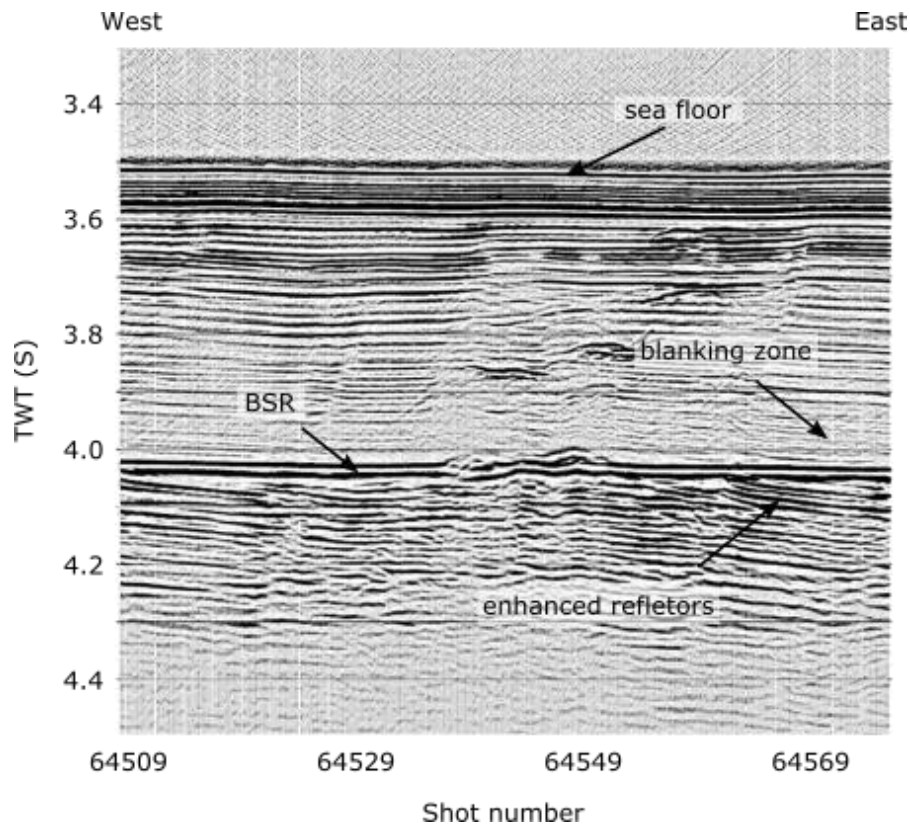


Figure 2.5: A classic example of a BSR from Blake Ridge, east of Savannah, Georgia, USA, modified after Hornbach (Hornbach et al., 2003).

Generally, BSRs also mimic the shape of sea floor as the depths of BSRs are a function of temperature and pressure, which both increase with depth beneath the sea floor. This character often makes BSRs easy to distinguish from background reflectivity as they can cross-cut other reflections.

Aside from gas hydrate-related BSRs, diagenesis-related BSRs have been observed in many places around the world. The generation of these reflectors is associated with mineralogical phase changes such as from opal-A to opal-CT, which can cause a sudden change of acoustic impedance (Berndt et al., 2004). However, these reflectors have a

polarity that is the same as that of seafloor, as a result of an increase in the impedance contrast. Likewise, their presence is normally beyond the depth of the BGHS (Thakur and Rajput, 2011).

2.2.1 Enhanced and blanking seismic reflection

P-wave energy can be significantly attenuated by free gas, and a small amount of free gas in the pores of sediments can decrease P-wave velocity dramatically (Domenico, 1977). The acoustic impedance (product of density and velocity) contrasts between sedimentary layers can be significantly increased by the presence of accumulation of gas beneath GHSZ, resulting in enhanced seismic amplitudes below the BSR (Figure 2.5). However, these enhanced reflections are localized and not laterally extensive and fade out rapidly with depth.

Suppressed seismic reflections (blanking) (Figure 2.5) in the hydrate zone are observed elsewhere around the world. The impedance contrast between low and high porosity regions can be reduced by low saturations of hydrates that can result in blanking (Holbrook et al., 2002). Recent studies (Boswell et al., 2014) suggest that loss of amplitude response (blanking), in sand rich sediments, can be attributed to low to moderate saturations of gas hydrate (Figure 2.6).

The result of Dillon and Max's model (2003) also showed that blanking increases with increasing the hydrate saturations. However, there is a lack of evidence from field studies for blanking as the prime indicator of presence of gas hydrates. Some studies have pointed out that blanking in the gas hydrate province is attributable to lithology, in regions such as in Kerala-Konkan region in India (Reddi, 2001). Wood and Ruppel also suggest that the blanking zone in seismic data may imply a paucity of horizontal reflectors, rather than lack of impedance contrast (Wood and Ruppel, 2000).

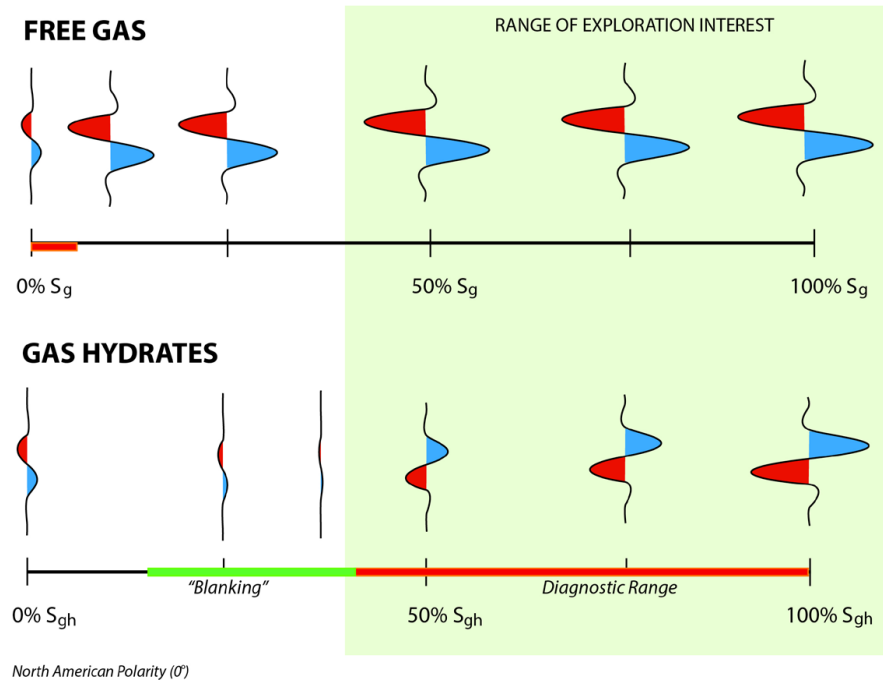


Figure 2.6: Schematic of seismic amplitude response to free gas and gas hydrate-bearing sands as a function of gas or gas hydrate saturation, after (Boswell et al., 2014)

2.3 Gas hydrate in New Zealand

Based on previous work, the largest potential gas hydrate province in New Zealand is considered to be the East Coast Basin that is located at the Hikurangi margin east of the North Island (Fohrmann and Pecher, 2012).

The presence of highly mobile fluids within the margin is demonstrated by the widespread gas seep sites and these fluids are considered to facilitate the formation of gas hydrate (Barnes et al., 2010). The formation mechanism could be refer to the model proposed by Hyndman and Davis (1992), which suggested the formation of gas hydrate was caused by the upward migration of pore fluids, which contain liquid and methane, into gas hydrate stability zone.

Previous work has shown that BSRs are widely distributed in the East Coast Basin (Henrys et al., 2009) and these BSRs are proposed to form by both upward fluid expulsion of deep gas sources (Pecher et al., 2010), and also upward migration of shallower, biogenically formed gas sources (Kroeger, 2015). On the Hikurangi margin, BSR reflectivity beneath structures like anticlines tends to be stronger than the reflectivity of BSRs beneath flat seafloor (Henrys et al., 2009). This is likely due to

these structures encouraging focused fluid flow towards the gas hydrate system (Henry et al., 2009).

2.4 Objectives of this study

In this study, re-processing of raw seismic data is undertaken from the southern portion of offshore East Coast Basin. The seismic data acquired in this area are part of the BRUIN survey (Figure 2.7). The primary objectives of this project are:

- 1) Carry out high-density seismic velocity analysis to yield more information about the distribution of gas and gas hydrate beneath the seafloor.
- 2) Generate higher-resolution seismic images of the gas hydrate system to improve the understanding of geological strata and structures that interact with the gas hydrate system.

These objectives are part of a larger motivation to explore the resource potential of individual gas hydrate deposits on the Hikurangi margin. Some previous work on gas hydrates has been published from this working area (Fohrmann and Pecher, 2012) but a broader (in a geographical sense) interpretation of long-offset seismic lines from the area has not been carried out.

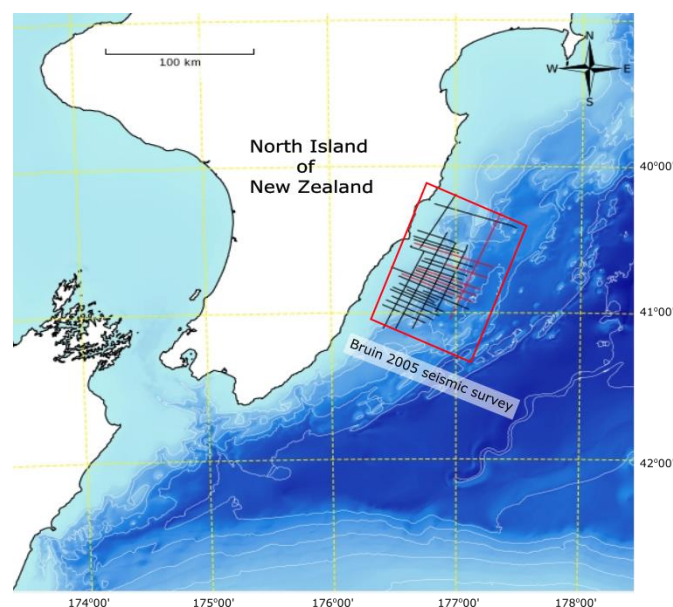


Figure 2.7: Location map of Bruin seismic survey 2005. Red lines are the seismic lines, which we used in our research.

3 GEOLOGICAL SETTING

3.1 Tectonic setting of Hikurangi Margin

The Hikurangi margin is at the southern end of the Tonga-Kermadec-Hikurangi subduction system (Figure 3.1). This margin is an ambiguous accretionary margin approximately 600-km-long off the eastern North Island (Barnes et al., 2002). The Hikurangi trench is shallower than the Kermadec Trench to the north and it has a flat floor, which is about 720 km in length and less than 70 km wide (Lewis et al., 1998). Hikurangi Margin marks the boundary between the obliquely convergent Pacific Plate and Australian Plate and the portion where oceanic crust of the Pacific Plate subducts beneath continental crust of the Australian Plate, New Zealand North Island (Barnes et al., 2010). Gravity models of the Hikurangi Plateau indicate that the area of oceanic plate being subducted beneath the North Island thicken from ~10 km in the north to ~15 km adjacent to the Chatham Rise and buoyant Hikurangi Plateau (Davy and Wood, 1994).

The Hikurangi Margin has been an active subduction margin since ~24 or 30 Ma and it has developed through the subduction of the Pacific plate (Stern et al., 2006). More than 80% of the margin-normal motion is accommodated on the subduction thrust (Nicol and Beavan, 2003) and most of the margin-parallel motion is accommodated in the upper plate including a combination of reverse faulting, strike-slip faulting, and vertical-axis clockwise rotations (Nicol et al., 2007).

The deformation styles of Hikurangi margin are complicated by its lateral response to many variables, including differences in convergence rates, convergence obliquity, sediment supply and smoothness of the subducting plate (Lewis et al., 1998). The northern Hikurangi margin includes numerous seamounts on the subducting Pacific plate and is characterised by a combination of tectonic erosion in the north and limited accretion (Pecher et al., 2005), and an imbricate thrust wedge with developed accretion further south (Lewis and Barnes, 1999). The southern end of Hikurangi margin represents a transition zone from oblique subduction to continental strike-slip

deformation (Barnes et al., 2010)

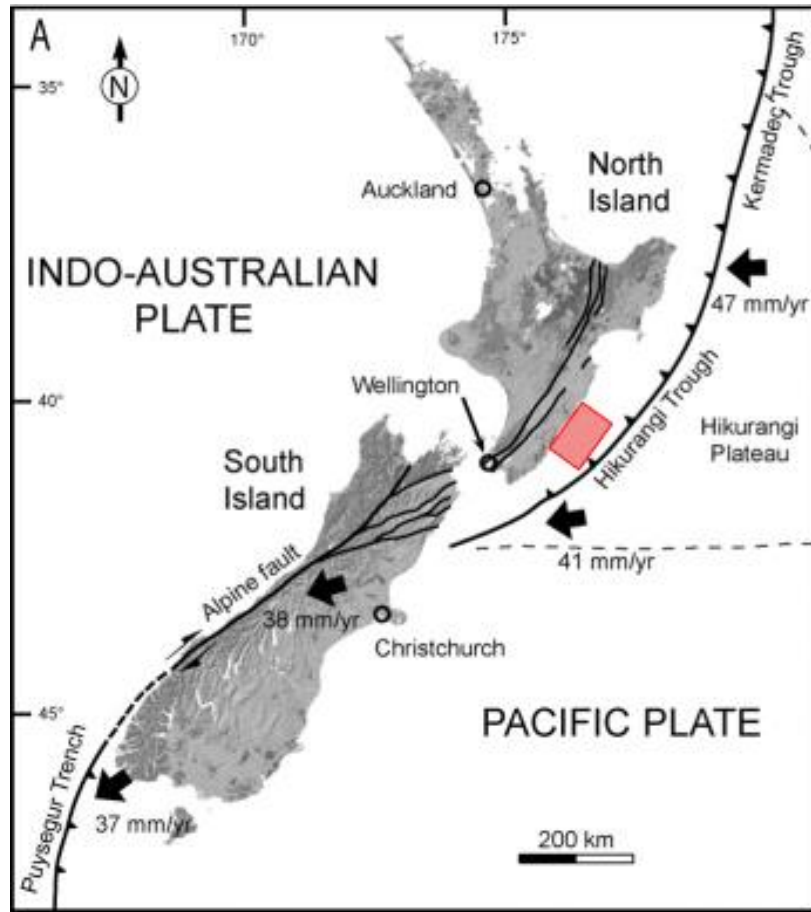


Figure 3.1: Diagram describing the tectonic setting of Hikurangi Margin after Bailleul et al. (2007). Red box represents our study area.

3.2 Tectonic-sediment interaction

The stratigraphy and structure of the Hikurangi margin contains both a Neogene subduction system and pre-subduction geological provinces (Barnes et al., 2010). The geology comprises an imbricated accretionary wedge, deforming against a Mesozoic basement of Torlesse terrane greywackes (Lewis and Pettinga, 1993). The wedge consists of three major stratigraphic groups: an inner foundation of pre-subduction rocks consisting of late Cretaceous and Paleogene rocks, an outer wedge of Pliocene to Pleistocene accreted trench filled turbidites, and a deforming cover sequence of Miocene to recent shelf and slope basin sediments (Barnes et al., 2010; Lewis and Pettinga, 1993). Numerous deformed rocks, which could be associated with active thrust faulting and folding, in Miocene were observed by Barnes et al. (2010) on seismic

images.

3.3 Gas hydrate system

The gas hydrate system study is similar to petroleum one (e.g. gas source, reservoir rocks and pathways for the migration of hydrocarbon), while it is necessary to have a good understanding of other factors such as geothermal gradient, composition of hydrates and pressures that control the stability of gas hydrate (Collett et al., 2009). In the following discussion the potential gas source and reservoir rocks within the study area will be reviewed.

3.3.1 *Source rocks*

Both biogenic and thermogenic gas are able to provide the sources for the formation of gas hydrate. (Collett, 2002). The low-TOC (total organic carbon) shales in Pliocene and Miocene within our study region (Uruski and Bland, 2011) are able to provide the biogenic methane. In this case abundant organic matter, however, is required for the in-situ formation of gas hydrate with biogenic gas (Finley and Krasen, 1989). Upward migration of methane from deeper sources (methane cycling) is likely to supply the additional methane for the formation of concentrated gas hydrate deposits (Paull et al., 1993).

In terms of thermogenic gas, the potential source rocks include the organic rich mudstones and shales in Late Cretaceous – Paleocene of the Whangai and Waipawa formations and the marine shales in Early Cretaceous (Rogers et al., 1999; Uruski and Bland, 2011). As our study area is located in a fore-arc basin that has low heat-flow, significant burial of the source rocks might be required to mature the source rock. In this case the marine shales in Early Cretaceous, which deposited across the basin floor (Uruski and Bland, 2011), have more potential to be the source rocks. Meanwhile, this is supported by the maturity modelling that was conducted by Uruski and Bland (2011)

3.3.2 *Reservoirs*

Currently, four primary play types of gas hydrate are known, but the most promising types for the future exploration are generally thought to be sand-dominated reservoirs and clay-dominated fractured reservoirs (Collett et al., 2009), which are able to provide

considerable permeability that is an important factor controlling the formation of highly concentrated gas hydrate deposits (Boswell, 2013).

The information about reservoirs within our study area is limited, as no wells were drilled in our study area. Two wells, Tawatawa-1 and Titihaoa-1, (Figure 4.1) that are nearest to the study area, however, could provide some information about the reservoir rocks. According to the petroleum report PR4326, the most potential reservoir rocks within our study area could be in Neogene turbidite sands. For example, Mid Miocene turbidites sands showed a good quality in porosity (17% to 24%), while the sands were encountered by Titihaoa-1 (Uruski and Bland, 2011). In addition to primary porosity, fractures that can increase porosity and permeability are important factor for the presence of concentrated gas hydrate deposits (Collett et al., 2009). Therefore, the potential gas hydrate reservoirs are likely to be distributed preferentially near faults and folds, which could be the pathways for the migration of gas from deeper sources and improve the quality of reservoir rocks.

4 METHODOLOGY

4.1 Data acquisition

The 2D seismic data used in this research are from the Bruin 2D seismic survey, which were recorded by Multiwave in the period of 30th January 2006 to 8th February 2006. A total of 1214.40 kilometres consisting of 29 seismic lines were acquired in the exploration licence of PEP 38333 & 38340 that is located in the East Coast Basin, North Island of New Zealand (Figure 4.1).

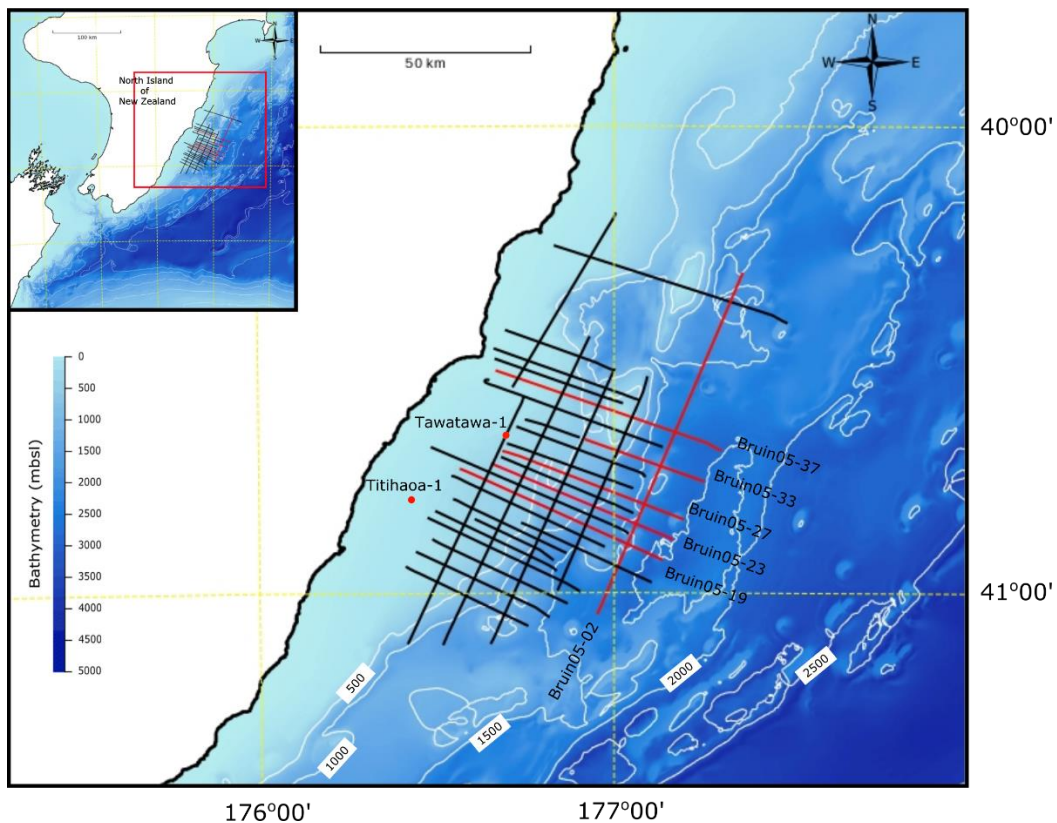


Figure 4.1: Base map of Bruin 2005 seismic survey. Red lines represent the seismic lines used in this research. Two wells are represented by red dot.

Six seismic lines (red lines in Figure 4.1) were chosen for re-processing in this research, depending on the observations and quality of BSRs on the seismic sections.

The main seismic acquisition parameters were as follows (details in the following table): Streamer length: 8100 m; number of channels: 648; group interval: 12.5 m; shot interval: 37.5 m; streamer depth: 7 m and source depth: 6 m (Fugro, 2006). The acquisition geometry is shown in Figure 4.2.

Description	Details
Data recorded by:	Multiwave CGG
Date recorded:	29 th Jan to 8 th Feb 2006
Vessel:	Pacific Titan
General:	
Field CDP Interval	12.5 m
Nominal Fold	108
Recording Format	SEG-D Rev 1, 8504 (3590 media)
Seismic source:	
Type	Airgun Array
Volume	4140 cu.in.
Pressure	2000pso +/- 10%
Depth	6 m
Shot interval	37.5 m
Gun delay	0 ms
Recording system:	
Type	SEAL
Record length	10000 ms
Sample interval	2ms
Number of Channels	648
Near Channel	1
Recording Delay	50 ms
Low Cut Filter	Out
High Cut Filter	200Hz @370 dB/ octave
Polarity	First break is negative
Receivers:	
Centre near group to centre far group	8087.5 .m
Streamer depth	7 m
Number of groups	648
Group interval	12.5 m
Centre source to centre near group	130 m
Number of Streamers	1

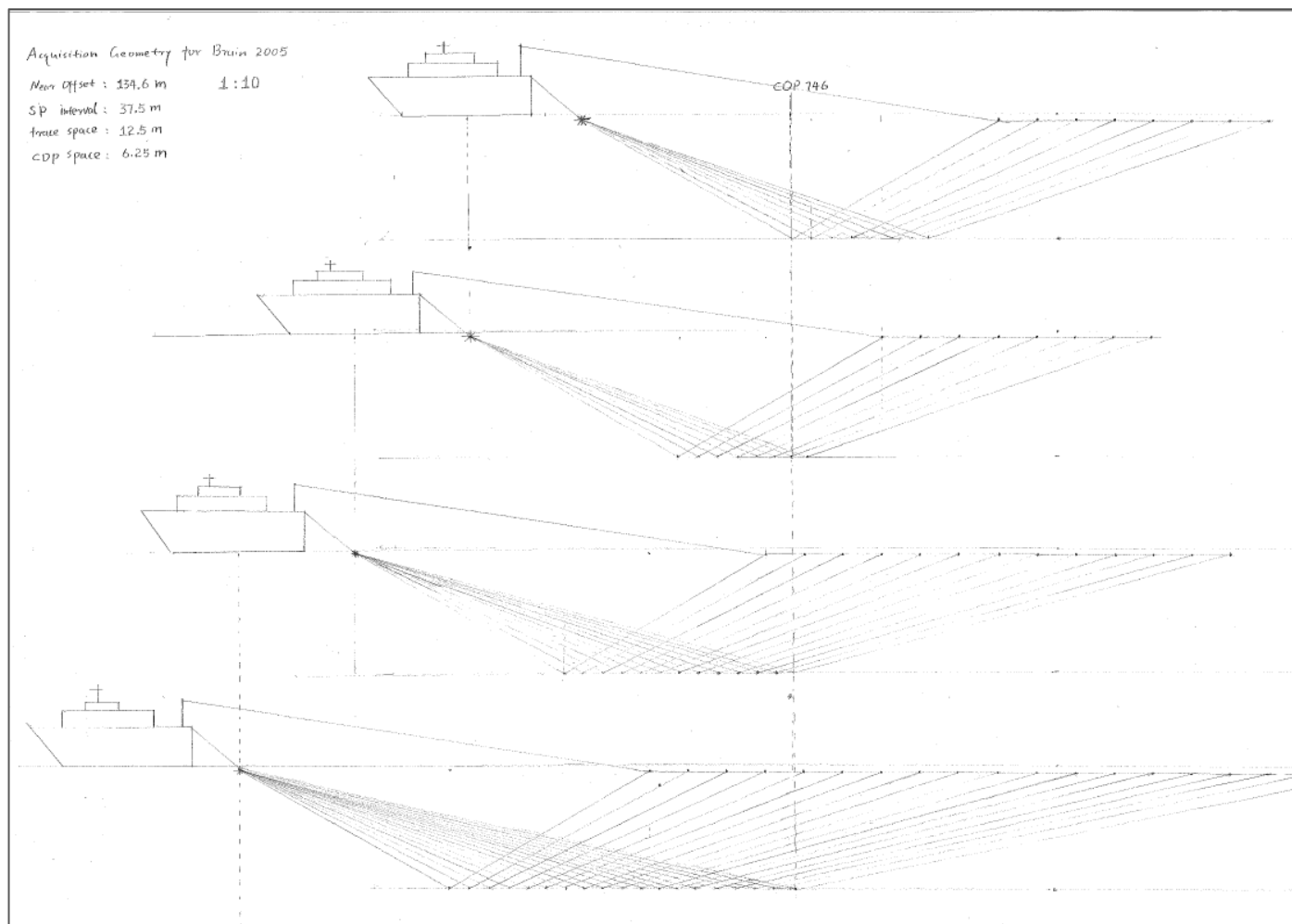


Figure 4.2: Acquisition geometry of Bruin 2005 seismic survey

4.2 Data processing

4.2.1 Introduction

Geophysical methods can be used in the identification and assessment of a gas hydrate province. For example, various types of seismic surveys, including 2D/3D conventional seismic, ocean bottom seismic and vertical seismic profiling can be used. 2D/3D conventional seismic surveys are the most popular method used in hydrocarbon exploration as they are useful for creating a map of the structure beneath the Earth's surface. These methods are able to detect BSRs, and are also useful for reconstructing P-wave velocity fields that assist with further detection of gas hydrates.

This chapter describes the primary seismic processing sequence adopted to create a high-resolution seismic image and velocity file from raw shot gathers. Seismic lines from the Bruin 2006 2D multi-channel seismic survey were used in this research. More specifically, five seismic lines that show clear BSRs were chosen for reprocessing, aiming at obtaining higher resolution seismic images and velocity files. Initial processing parameter testing was performed on line BR05-33. The processing platform used at all stages of seismic analysis was GLOBE Claritas – a package capable of 2D and 3D land and marine seismic data processing. GLOBE Claritas is developed and supported by GNS Science, which is a crown research institute of New Zealand that is responsible for geosciences.

4.2.2 Multichannel seismic data processing

4.2.2.1 Geometry

The processing geometry was defined from a UKOOA (United Kingdom Offshore Operators Association) format file, an industry standard format for seismic survey positioning data. When making the wiggly line gathers, the CDP (Common Depth Point) line is fitted to the hit-points, so before making the “wiggly line”, hit-points must be defined. Automatic picking, a module within Claritas, was used for the picking of hit-points. Then a “wiggly line” survey was developed from individual geographical positions of both shot points and receivers, by adopting the CDP spacing of 6.25 m. The

processing geometry of line BR05-33 is shown in Figure 4.3 where it is plotted in a Cartesian coordinate system with the middle shot placed at the origin (0,0). The maximum fold for CDPs on this “wiggly line” is defined as 110.

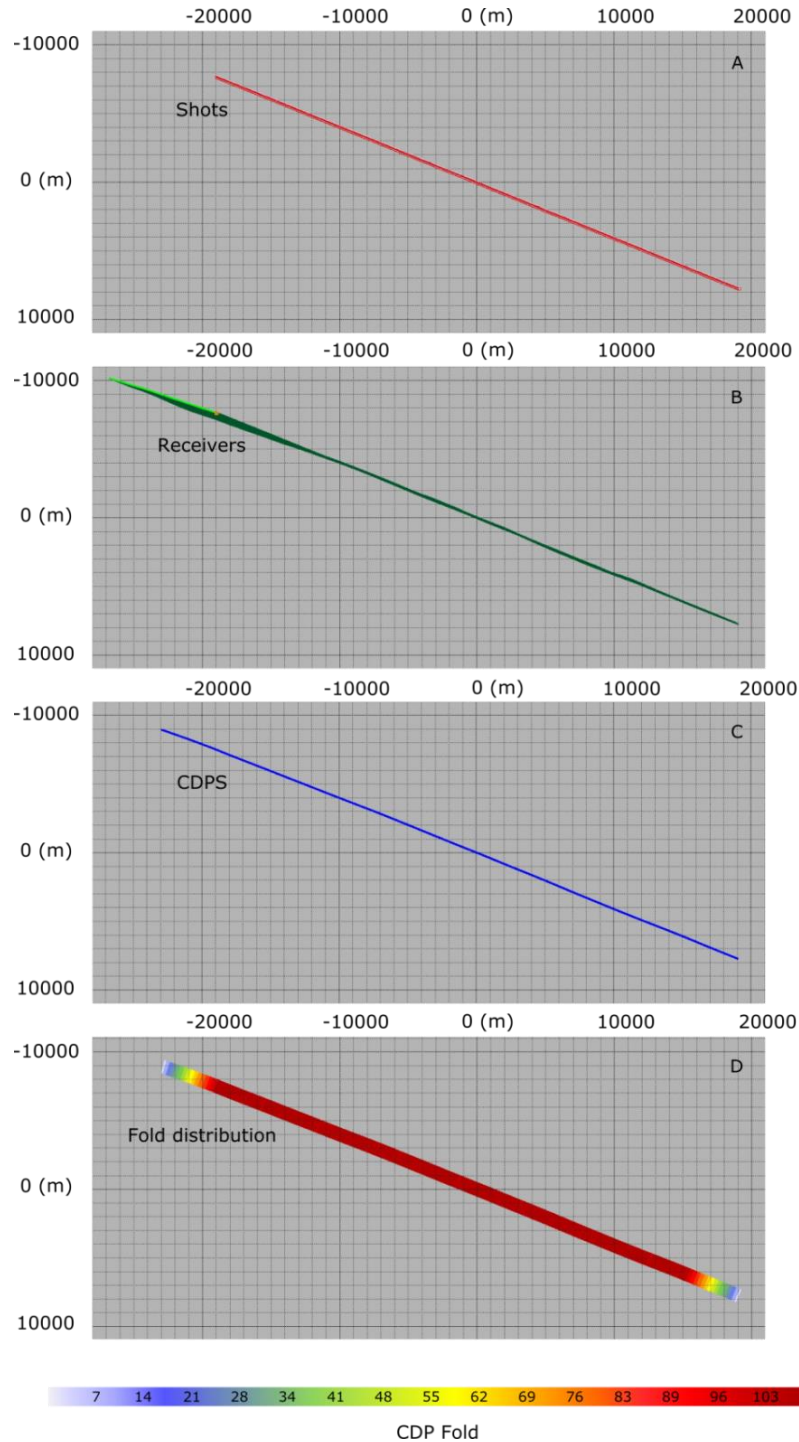


Figure 4.3: Processing geometry of Line BR05-33. A) Distribution of shot points in Cartesian coordinate system (grid squares are 1000 m by 1000 m). B) Distribution of receiver points in the same Cartesian grid. C) Distribution of CDPs, defined from the shot point and receiver point locations. D) Areal fold distribution, where the maximum fold is 110.

4.2.2.2 Seismic shot quality control

Shots were read from digital linear tapes in SEG-D format and converted to SEG-Y format, then written out to disk. Initial shot quality control checks were performed by ensuring that shots had the correct number of traces, trace ordering and offset distribution. The non-live traces and bad shots were removed as well. Geometry information defined in Section 4.2.2.1 was added to the shot-domain data. A Butterworth filter with corner frequencies of 4, 12, 150 and 200 Hz was utilized to remove the low-frequency swell noise and other high-frequency noise. The shot data were shifted up 50 ms and then a compensation module for spherical divergence, caused by propagation of the seismic wave through subsurface layers, was applied. Figure 4.4 shows the result of the processing applied on shot 1662.

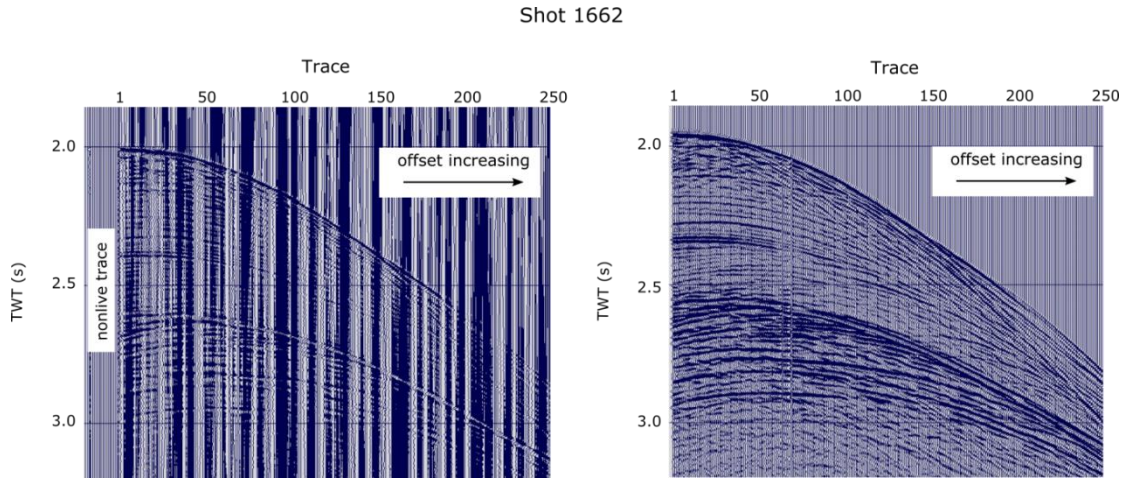


Figure 4.4: Variable area wiggle display of shot 1662. A) Part of raw shot gather. B) Same part of raw shot gather as (A) but filtered with a Butterworth filter and other processing. The bulk of the improvement from (A) to (B) comes from the removal of low frequency swell noise.

4.2.2.3 Near trace stack and post-stack time migration

Each CDP was truncated to the near offset traces. More specifically, the farthest offset for each CDP was defined as 450 m. This process is necessary as a precursor to stacking in order to avoid “NMO-stretch” and produce the best possible representation of normal incidence reflectivity. The effect of source-receiver offset was corrected for by applying a normal move-out correction (NMO), assuming a constant velocity of 1500 ms^{-1} . Detailed velocity analysis was not required at this stage as only the near traces were

included. Next, NMO-corrected traces in each CDP gather were summed and normalised to create one trace per CDP, which is referred to as conventional stacking. In order to shift seismic events to their correct subsurface position in time and space, a finite difference, post-stack, time migration algorithm was applied to stacked sections. The migration algorithm produces a near-trace, post-stack-time migrated section. An example of this section is given in Figure 4.5

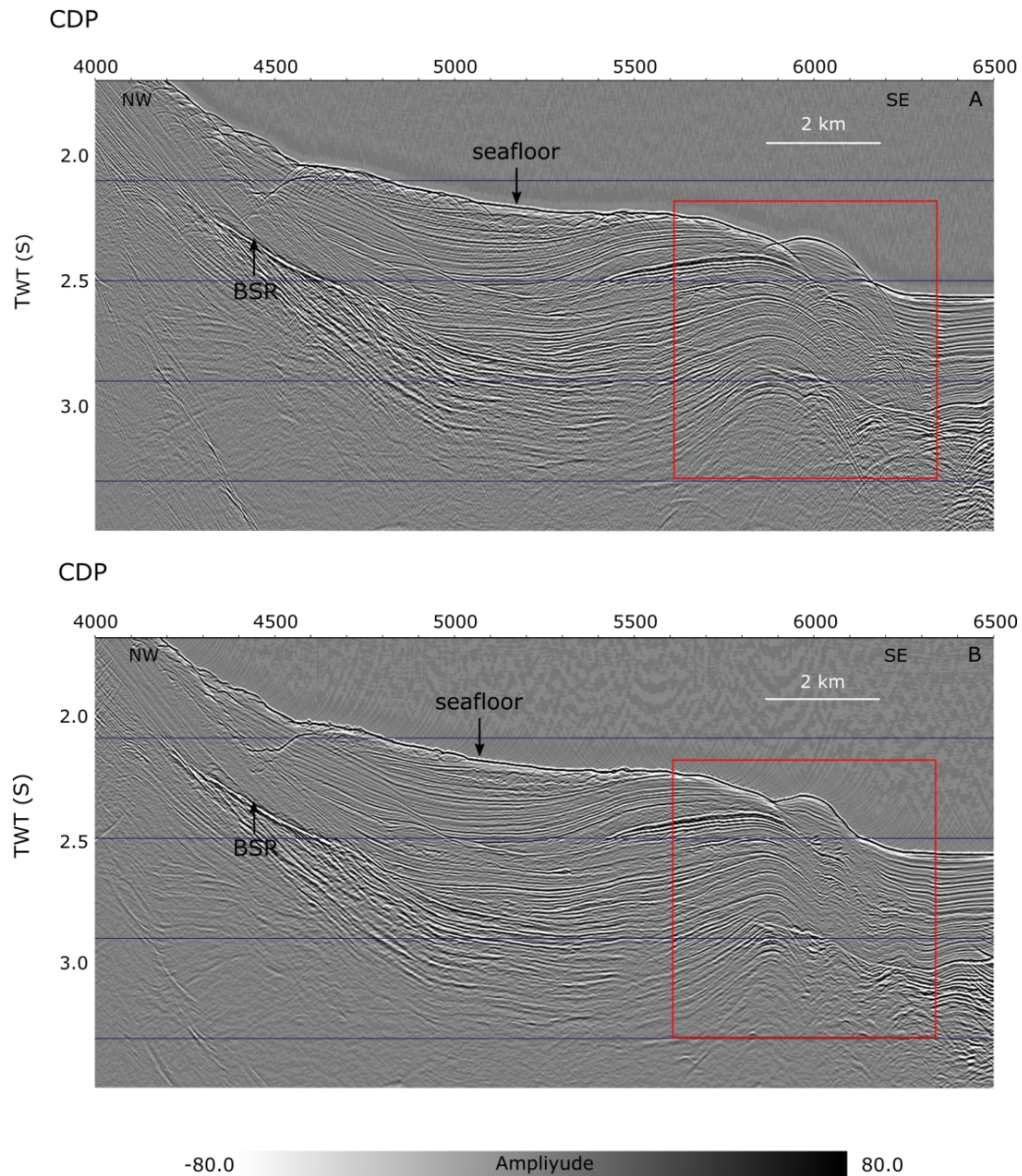


Figure 4.5: Comparison between near trace stacked seismic section and seismic section after post-stack time migration. A) A near-trace stacked section between CDPs 4000 and 6500. A pronounced BSR is annotated. B) Near-trace section with post-stack time migration in the same display and CDP range as (A). The results of post-stacktime migration are apparent along the seafloor and in the red box area, as the subsurface seismic events were shifted to their supposedly correct positions.

4.2.2.4 Pre-stack time migration

The post-stack time migration does not provide as accurate an image of subsurface structure as a pre-stack migration, due to the presence of complex structures within the research area that are a result of the strong convergence. In order to enhance the accuracy of seismic events and obtain higher resolution seismic section, pre-stack time migration was applied. An example is given in Figure 4.6.

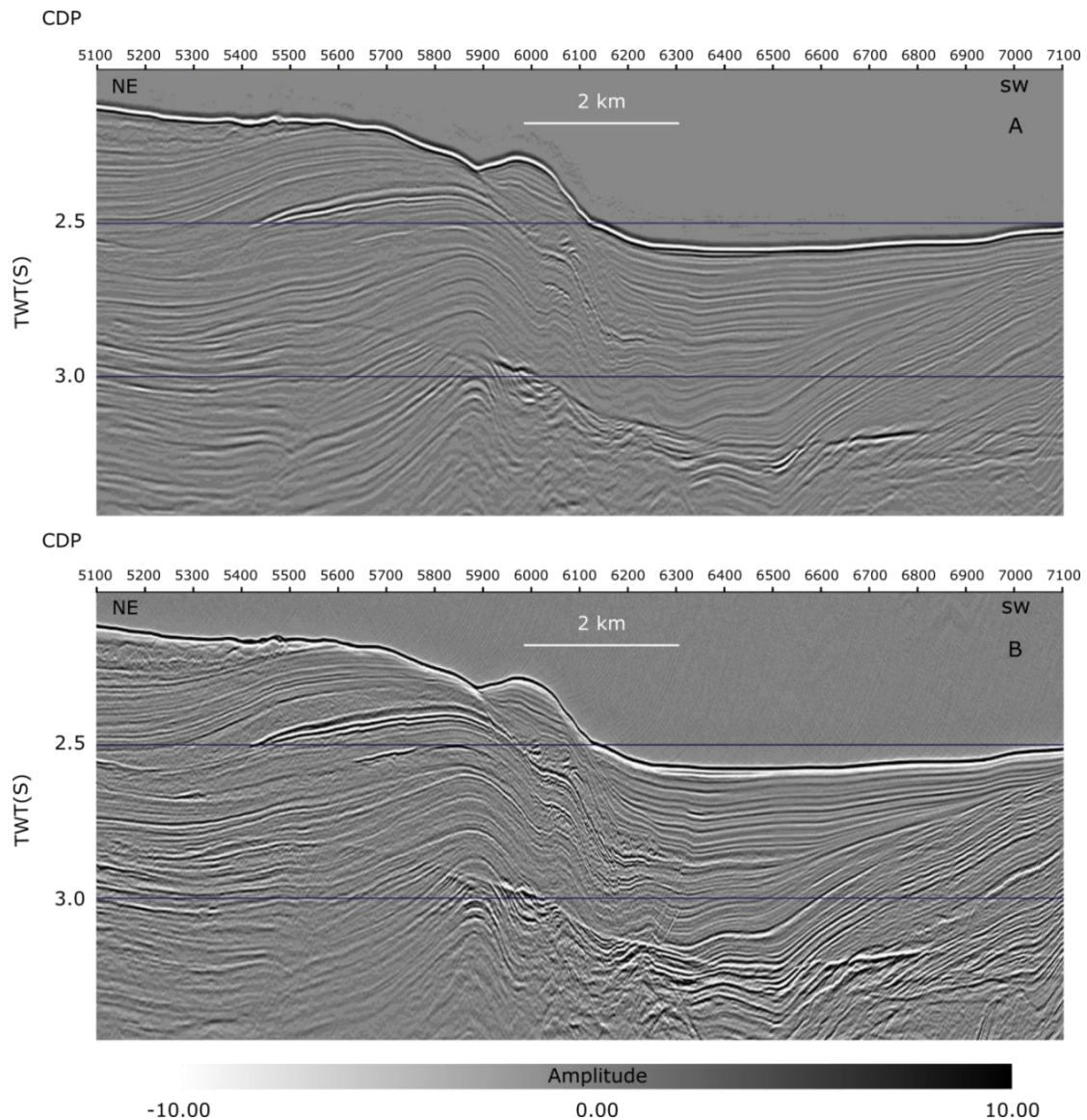


Figure 4.6: Comparison between original industry-processed seismic section and our reprocessed seismic section after pre-stack time migration. A) Original industry seismic section of BR05-33 between CDP 5100-7100. B) Seismic section processed with pre-stack time migration in the same display and CDP range as (A). The processed seismic section has higher resolution, especially in the display of faults and this is important for the following interpretation stage.

4.2.3 Seismic velocity analysis

Conventional seismic processing methods are able to help us to obtain an accurate imaging of subsurface structures and strata that can be used to understand the tectonic evolution. Velocity analysis is an important step in the processing sequence, as it is required for migration stage. However, the seismic velocity itself can also be useful for both qualitative and quantitative seismic interpretation, since seismic velocities provide information on the nature of the sediments or rocks as well as the fluid that fills their pore spaces.

$$V_{rms} = \sqrt{\frac{\sum_{k=1}^n V_k^2 t_k}{\sum_{k=1}^n t_k}}$$

Traditionally, root mean square P-wave velocity (V_{rms} , above, where t_k is the vertical 2-way time through the k th layer) is estimated from the normal move out analysis of CDP gathers in offset-time domain and the output is V_{rms} versus two-way zero-offset travel time (Yilmaz, 2001). Next, Dix's (1955) equation is used to estimate interval velocity, which can provide a higher resolution. However, interval velocity analysis may loss accuracy in the complex geologic region, because the lack of dip information (Reshef and Rüger, 2008). In this research, we used an automatic velocity picking routine (section 4.2.3.1) and it allows that the velocities picks were made by computer, therefore, the influence from subjectivity of people is avoided. For more information on this technique, the reader is referred to Crutchley et al. (2014).

4.2.3.1 Automatic velocity picking

Before the automatic velocity picking, pre-processing is necessary to reduce spatial aliasing and enhance the coherency of reflections in gathers (Figure 4.7 A). In order to reduce the spatial aliasing, two virtual offsets were interpolated in the interval of original offsets (Figure 4.7 A and B). The interpolation was done in the time domain and a least squares polynomial was used to fit to the values in the input traces. After this stage, CDP gathers displayed with much lower spatial aliasing (Figure 4.7 B). Next, a narrow Butterworth filter with corner frequencies of 5, 10, 40 and 60 Hz was applied

to the gathers to remove a significant part of the high-frequency component.

An automatic semblance picking (Figure 4.7 C) routine that is part of the Globe Claritas suite of processing tools was used to pick stacking velocities from the semblance spectra. The picking was limited to a window extending from the seafloor to a defined lower boundary, which contains most of the seismic events that will be used in the following interpretation stage. Figure 4.7 D shows NMO correction of CDP 5700 with stacking velocities from our automatic picking.

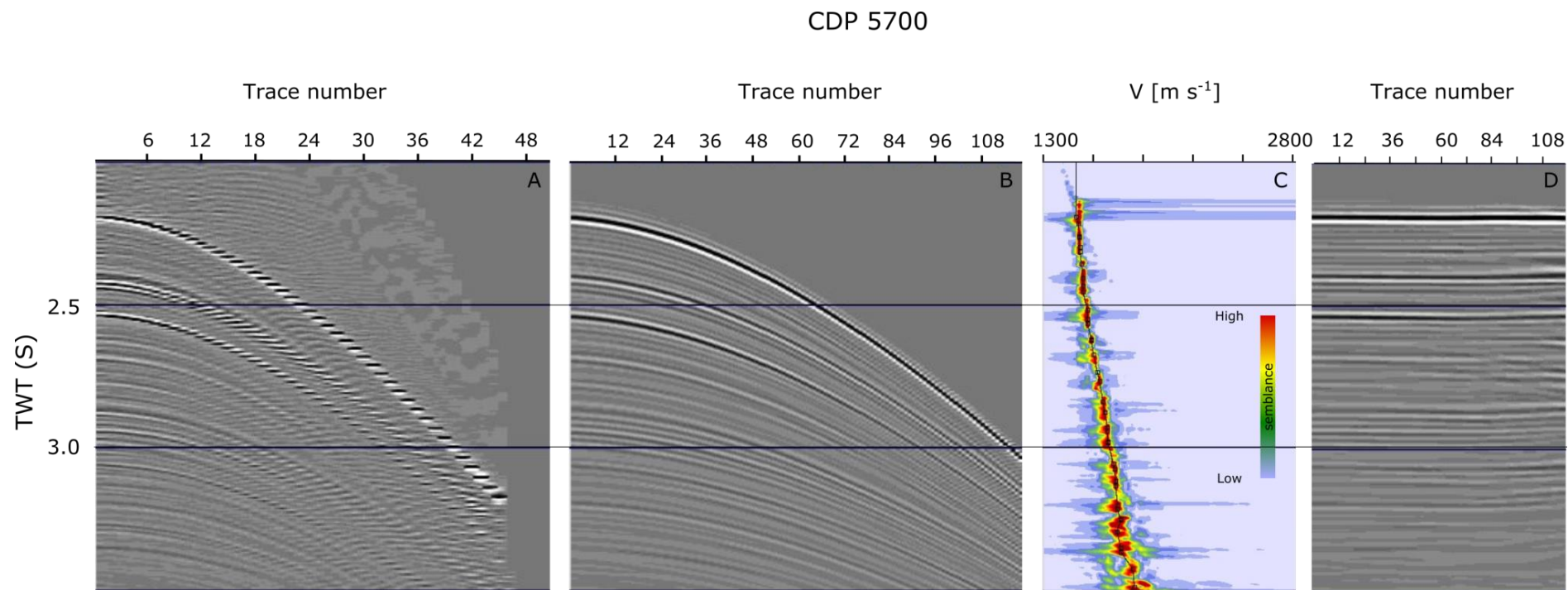


Figure 4.7: Preparation for automatic velocity picking A) Original pre-stacktime migrated CDP 5700 gather from Line BR05-33. Spatial aliasing is apparent. B) Pre-processed gather of CDP 5700 in the same display as (A). Much spatial aliasing was removed and the coherency of the gather was improved. C) The semblance spectrum of CDP 5700, showing the best stacking velocities for different reflections (black line). D) The same gather as in (B) after normal move-out correction using the stacking velocities from automatic picking in (C).

4.2.3.2 Conversion of velocity file

In the final stage of processing, the stacking velocity field was converted to an interval velocity field. The interval velocity is the average velocity of an interval or layer and it can be computed from V_{rms} using Dix's (1955) equation, where the interval is defined in terms of the two-way travel time rather than by discrete differences in depth (Khan and Akhter, 2011).

$$V_{n-layer} = \left(\frac{V_n^2 - V_{n-1}^2 t_{n-1}}{t_n - t_{n-1}} \right)^{1/2}$$

The equation above is the Dix equation, where V_{n-1} and V_n are the stacking, or V_{rms} velocities from the datum to reflectors above and below the layer and t_{n-1} and t_n are reflection arrival times.

A range of plausible interval velocities for the shallow sub-seafloor sediments of interest was defined in order to be able to remove erroneous velocities. For this research, the minimum interval velocity was set as 1200 ms^{-1} (i.e. much lower than any expected interval velocities) and the maximum interval velocity as 4500 ms^{-1} (higher than any velocities expected within the gas hydrate zone). Therefore, any stacking velocity that generates interval velocities outside of the range between 1200 ms^{-1} to 4500 ms^{-1} were edited out of the stacking velocity field before converting to the interval velocity field.

At small-scales lateral velocity jumps (Figure 4.8 A) are caused by uncertainty in stacking velocity picks, so a smoothing filter in the horizontal direction was applied to smooth out these jumps. The result for the application of a smoothing filter is shown in Figure 4.8 B, and Figure 4.8 C shows the result of the velocity conversion. A low velocity zone related to the BSR (black line) is shown on the interval velocity plot, and the location of the zone coincides with the location of enhanced seismic reflections underlying the BSR in the seismic section (Figure 4.8 D).

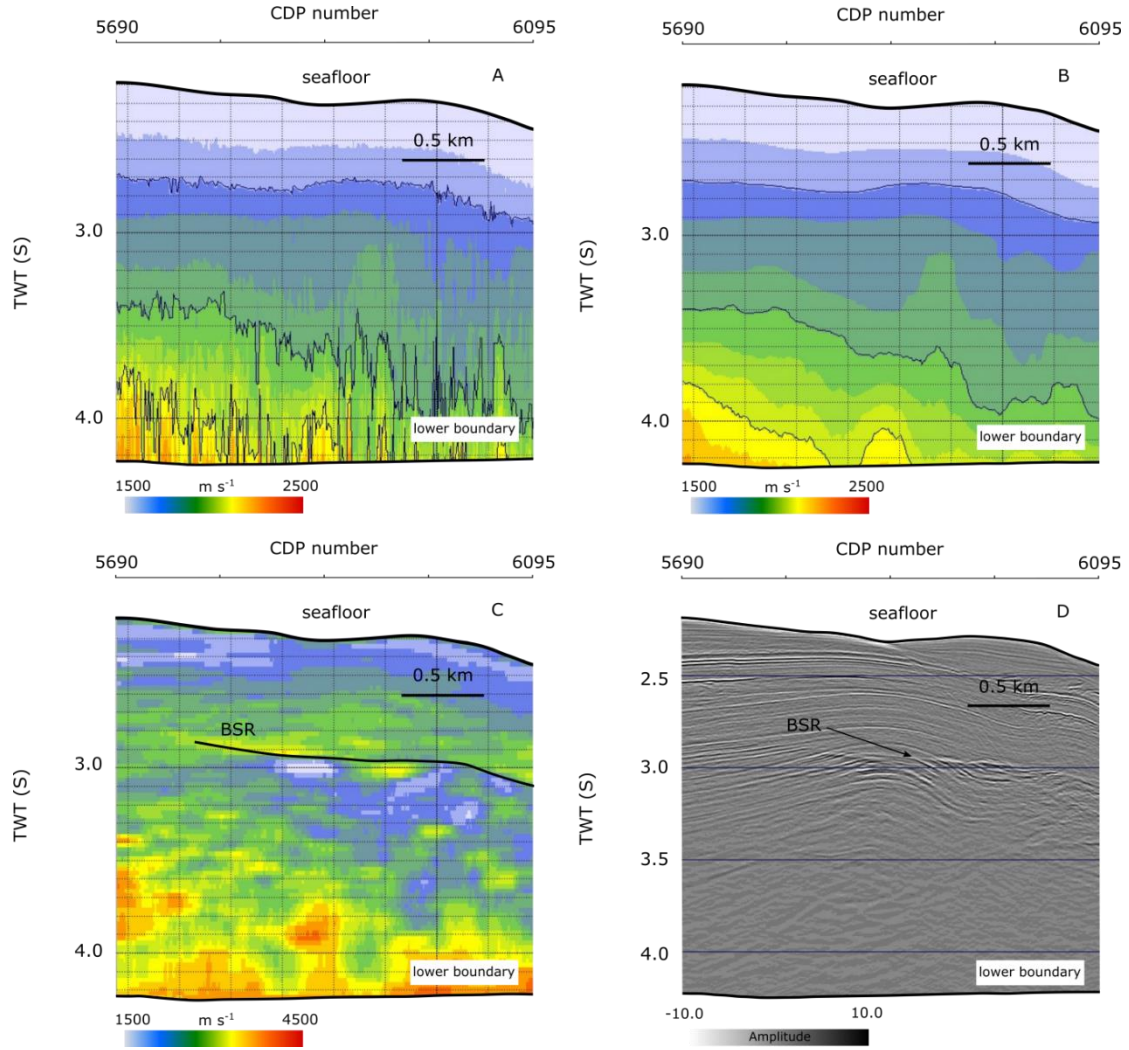


Figure 4.8: Converting stacking velocities to interval velocities. A) A plot of multiple automatic velocities picks between CDP 5690 and 6095 from BR05-33. A number of small-scale velocity jumps is shown on the plot. B) The stacking velocity field from Figure 4.8 A after application of a horizontal smoothing filter. C) Interval velocity field obtained from Dix conversion of the stacking velocities. BSR (black line) is shown on the plot and the contrasting velocities of broad lithological features are identifiable. D) High resolution seismic section from the same extent as Figure 4.8 C, for comparison with the velocities in (C).

5 RESULTS

5.1 Distribution of BSRs

The distribution of gas hydrate related BSRs is dependent on several conditions such as the distribution of gas and water supply, geothermal gradient and water depth. Figure 5.1 shows the distribution of the BSRs on our chosen seismic lines. It is apparent that in this study area, the BSRs are normally located in the deeper water, beyond the approximately 1000 meters depth. We also found that the observations of the BSRs are usually correlated with geological features that are favourable to focus fluid flow such as dipping strata and anticlines. Moreover, gas packets, which were represented by the enhanced reflections (or bright spots) on the seismic sections, are often observed beneath the BSRs with high amplitude.

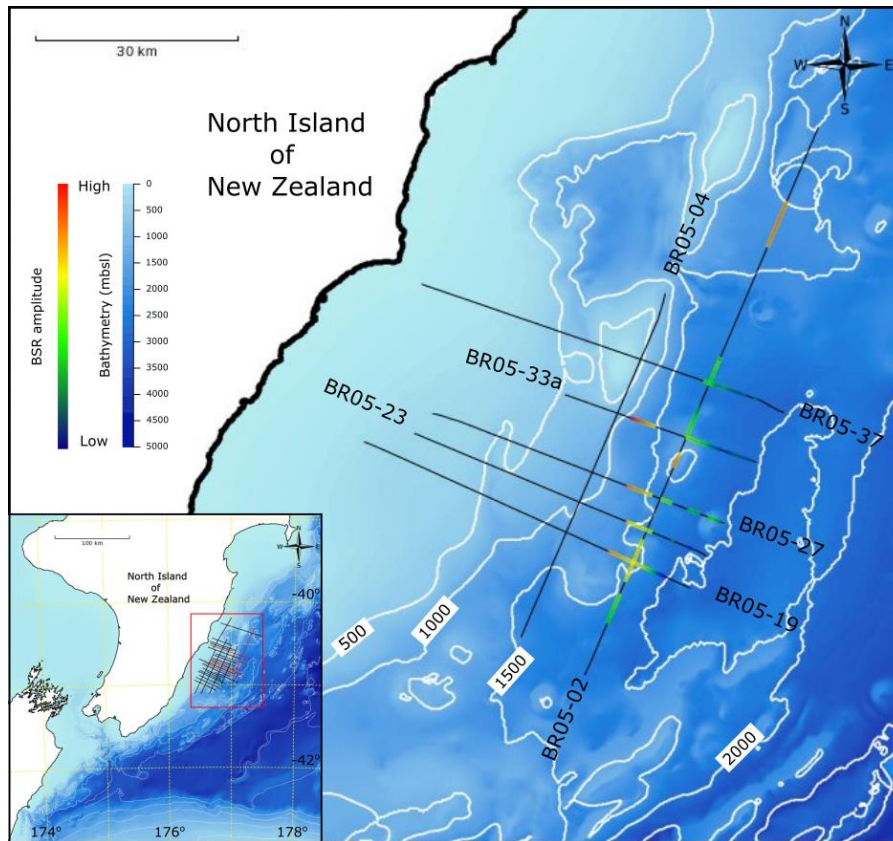


Figure 5.1: The base map shows the distribution and amplitudes of BSRs on the chosen seismic lines. The colour bars show the bathymetry (blue shades) and the amplitude of BSRs (blue to red shades).

5.2 Observation of BR05-37

This section shows complicated structures, caused by thrust faults (Figure 5.2). The re-processed seismic data reveal well defined reflections and the distribution of BSRs. Three weak BSRs are observed on this section that disappear to the northwest. A double BSR beneath one of the BSRs is observed at the most southeast extent (Figure 5.3). On the velocity plot the contrasting velocities of broad lithological features are identifiable. Moreover, we observed two low velocity anomalous zones beneath the BSRs (Figure 5.3).

5.3 Observation of BR05-33

This section shows relatively simpler structures (Figure 5.4) compared to parallel line 37 described above. A dipping strata zone is located in the northwest of this section and in this zone we observed a strong BSR (Figure 5.5). Moreover, enhanced reflections are located beneath the BSR. On the velocity plot, the corresponding zone shows a low-velocity anomalous zone. In the southeast part of this section, the structures become complicated due to thrust faults (Figure 5.6). Weaker BSRs, compared with the strong one discussed before, are observed in this region and on the velocity plot we also observed a low-velocity anomalous zone below BSRs, and high velocity zone above BSRs.

5.4 Observation of BR05-27

The seafloor of the chosen seismic section (Figure 5.7) is lower than those of the two sections discussed before. This section shows complicated structures, which is also caused by thrust faults. Relatively weak BSRs, are observed in the middle part of this section (Figure 5.8) and it is difficult to identify BSRs in the southeast part of this section. On the velocity plot, velocity structures related to BSRs and broad structures are identifiable. A strong reflection was observed above the BSR of the gas hydrate stability zone, and on the velocity plot a high velocity anomalous zone is existent between the BSR and the strong reflection (Figure 5.8).

5.5 Observation of BR05-23

The section (Figure 5.9) shows that the seafloor is continuously falling down to southwest. Complicated structures related to thrust faults are still existent on this section. However, there is only one BSR that is identifiable (Figure 5.10). BSRs are hard to identify, due to structural complexity. On the velocity plot, a high velocity anomalous zone is located above the BSR, while a low velocity anomalous zone is located below the BSR.

5.6 Observation of BR05-19

The seafloor of this section is the deepest in the five seismic sections. It means that the seafloor in the research area is downward oblique from northwest to southeast. The structures are relatively simpler than the nearest seismic section (BR05-23), and therefore it is easier to identify the BSRs (Figure 5.11). However, thrust faults are still developed on this section. A continuous BSR, mimicking the seafloor and crossing reflections of sediments, is identified. On the velocity plot we observed two low velocity anomalous zones beneath the BSR (Figure 5.12).

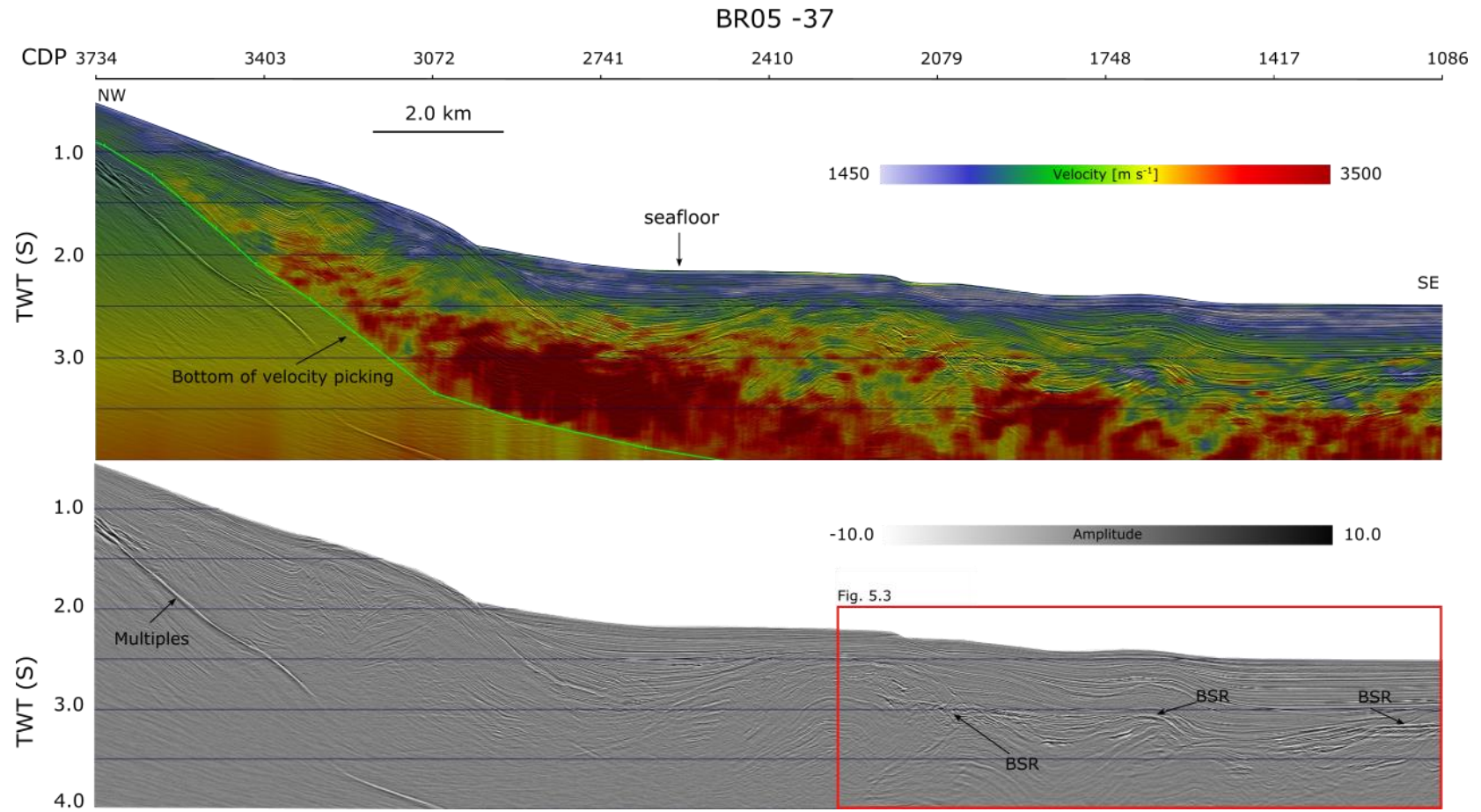


Figure 5.2: High-resolution velocity analysis from BR05-37. This section includes 2648 CDPs (16.55 km) and the beginning is at the cross point with BR05-04. This section displayed as a colour plot interval velocities (above) and a grey scale variable-density plot of the seismic data (below). The colour bar show that the range of velocities is between 1450 to 3500 ms^{-1} . The bottom of velocity picking is shown as the green solid line. Arrows point out the BSR. Figure 5.3 shows an enlargement from the red box.

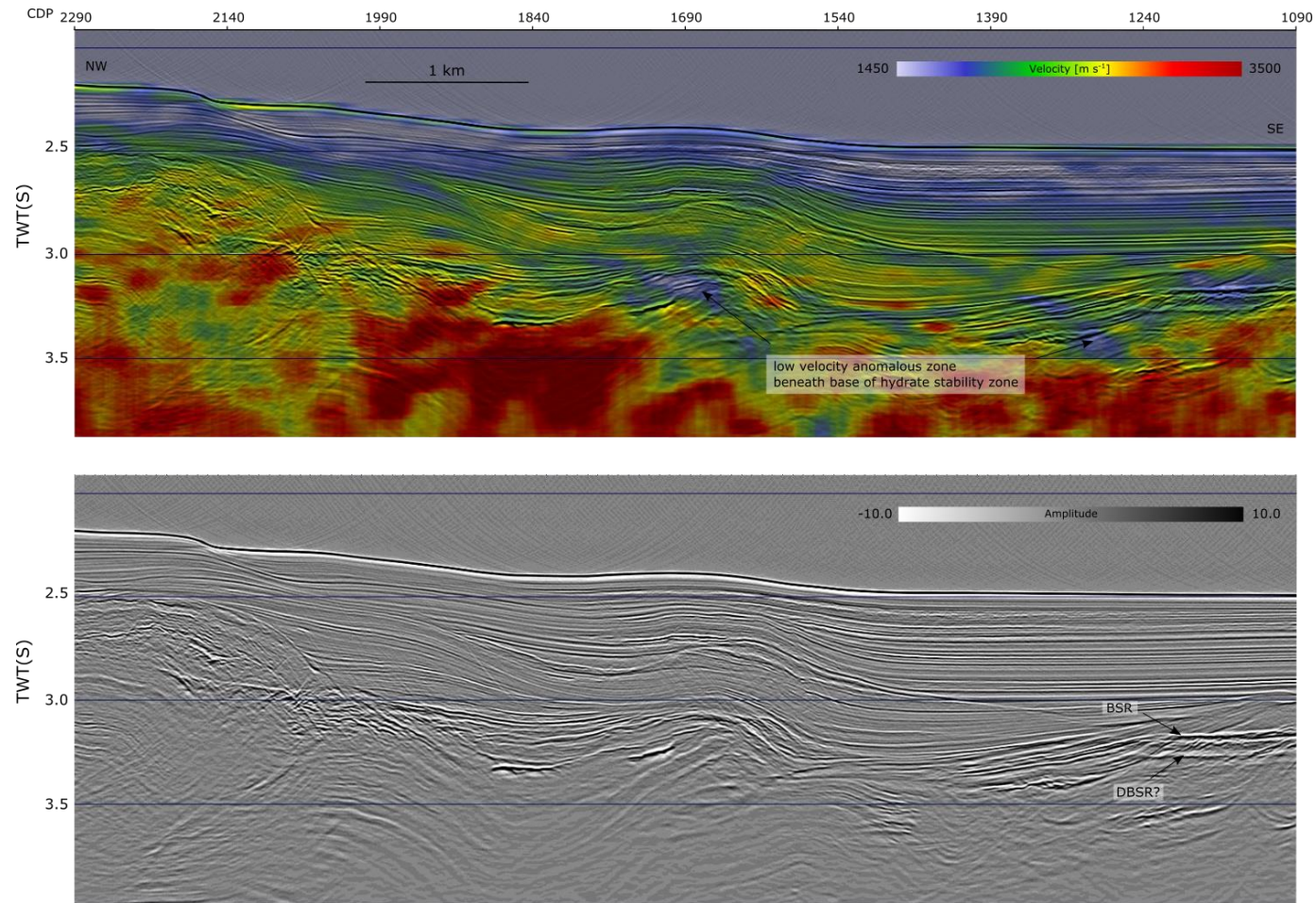


Figure 5.3: High-resolution velocity analysis from zoomed in zone of Figure 5.2. This section displayed as a colour plot interval velocities (above) and a grey scale variable - density plot of the seismic data (below). White and blue solid lines represent observed BSRs and DBSR. Blue dash lines on grey scale section represent the inferred BSRs that mimic to the seafloor and connect observed BSRs together. Two low velocity anomalous zones were pointed out by arrows.

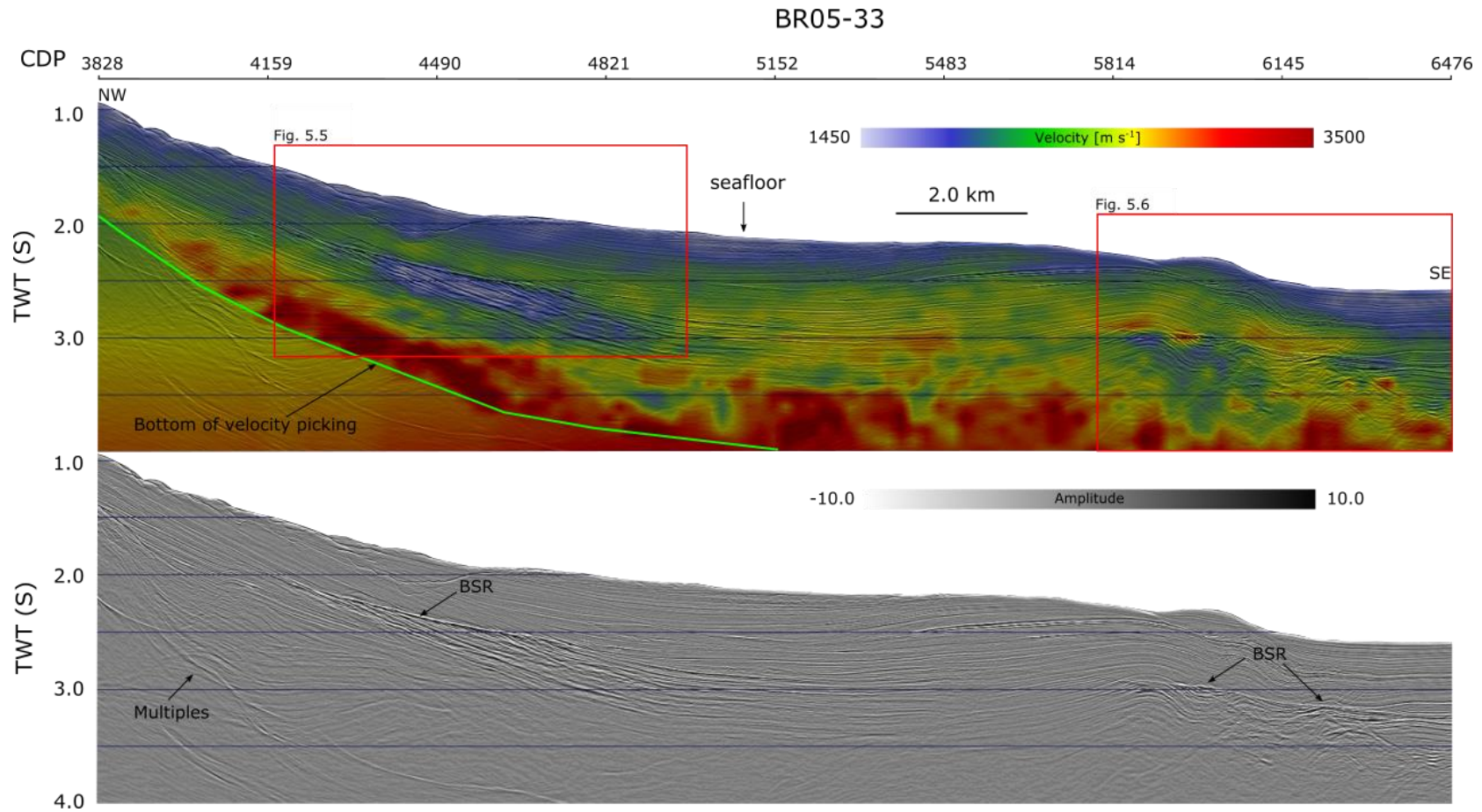


Figure 5.4: High-resolution velocity analysis from BR05-33. This section includes 2648 CDPs (16.55 km) and the beginning is at the cross point with BR05-04. This section is displayed as a colour plot of interval velocities (above) and a grey scale variable-density plot of the seismic data (below). The colour bar show that the range of velocities is between 1450 to 3500 ms^{-1} . The bottom of velocity picking is show shown as the green solid line. Enlargements from the left red box and right red box are shown in Figure 5.5 and Figure 5.6, respectively.

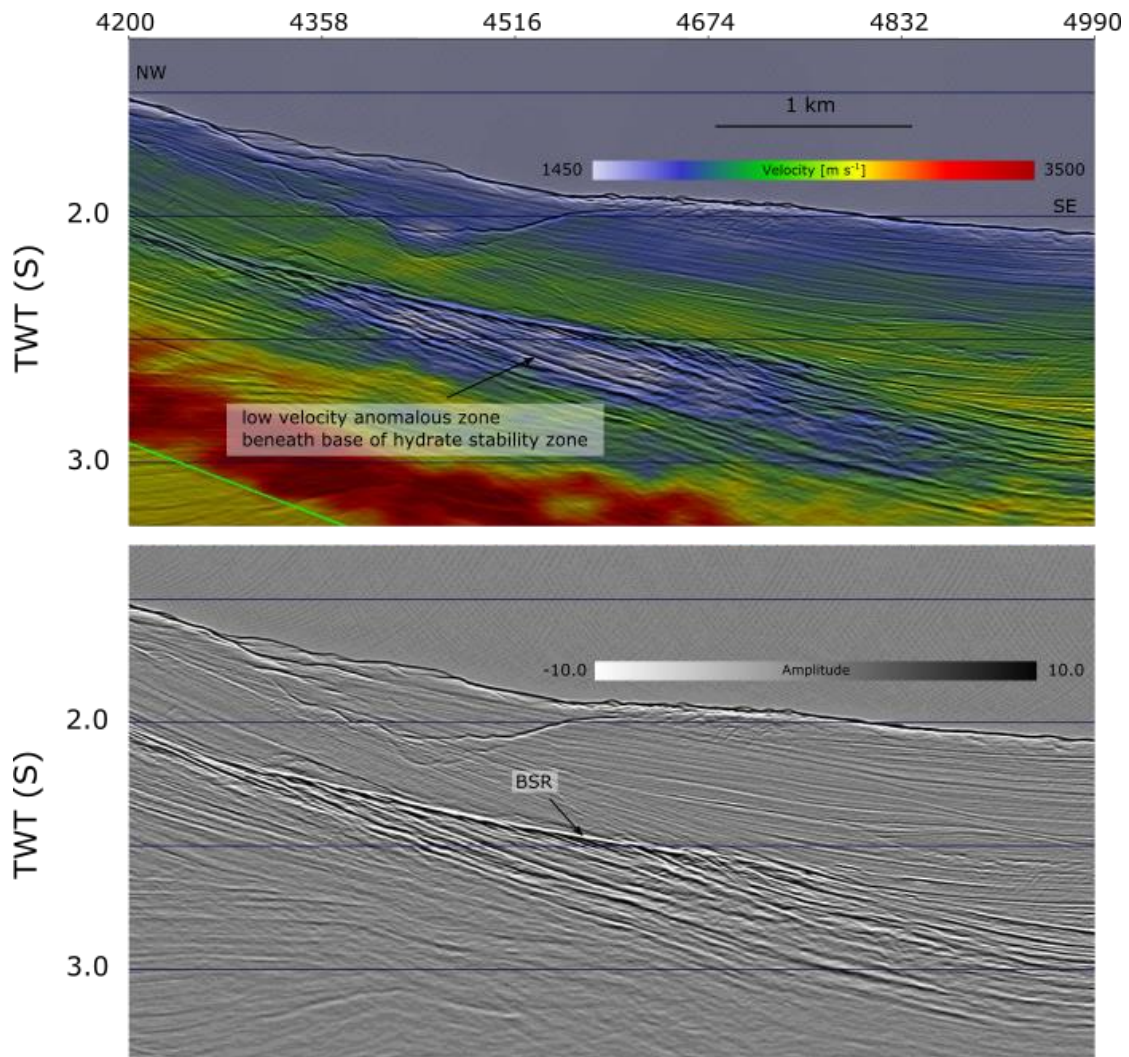


Figure 5.5: High-resolution velocity analysis from left red box in Figure 5.4 (Line BR05-33). White and blue solid lines represent observed BSRs on velocity plot and grey scale section, respectively. A low velocity anomalous zone is pointed out by the arrow. The colour bar shows that the range of velocities, between 1450 to 3500 ms^{-1}

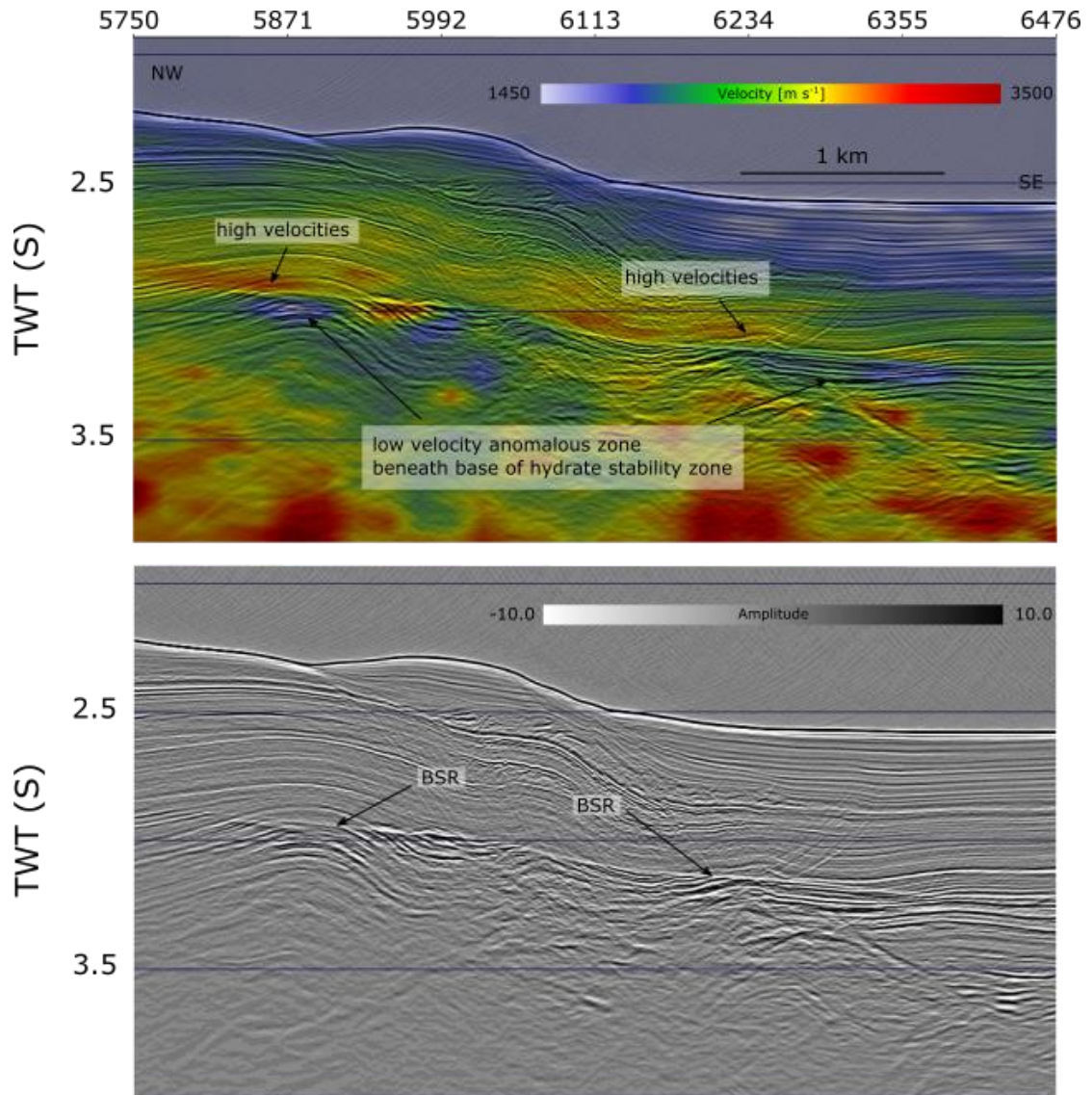


Figure 5.6: High-resolution velocity analysis from right red box in Figure 5.4 (Line BR05-33). White and blue solid lines represent observed BSRs on velocity plot and grey scale section, respectively. Low velocity anomalous zones and high velocity zones are pointed out by arrows. The colour bar shows that the range of velocities, between 1450 to 3500 ms^{-1} .

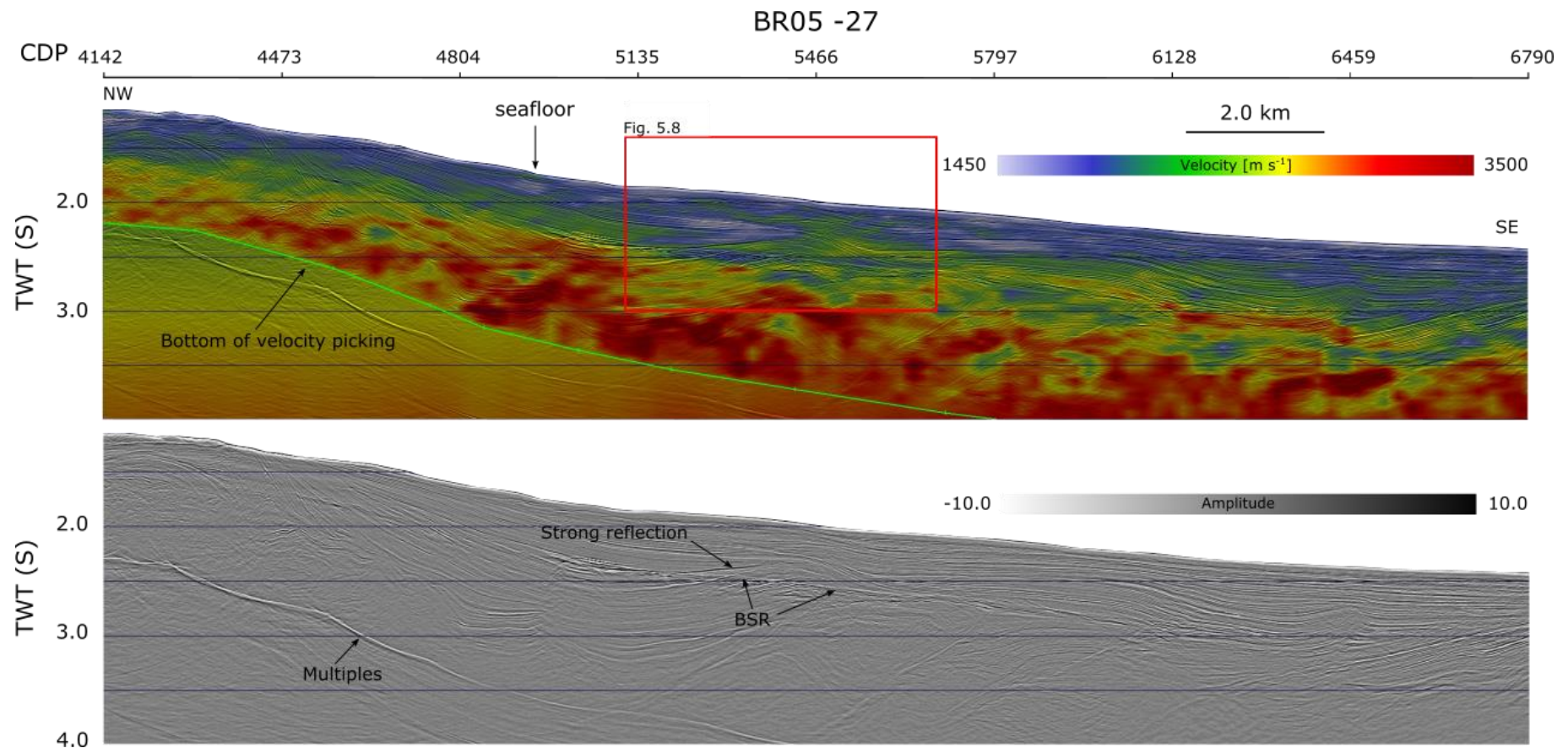


Figure 5.7: High-resolution velocity analysis from BR05-27. This section includes 2648 CDPs (16.55 km) and the beginning is at the cross point with BR05-04. This section is displayed as a colour-plot of interval velocities (above) and a grey scale variable-density plot of the seismic data (below). The colour bar show a range of velocities between 1450 and 3500 ms⁻¹. The bottom of velocity picking is shown as the green solid line. A strong reflection, pointing out with arrow, is located above the BSR. The red box shows the location of an enlargement given in Figure 5.8.

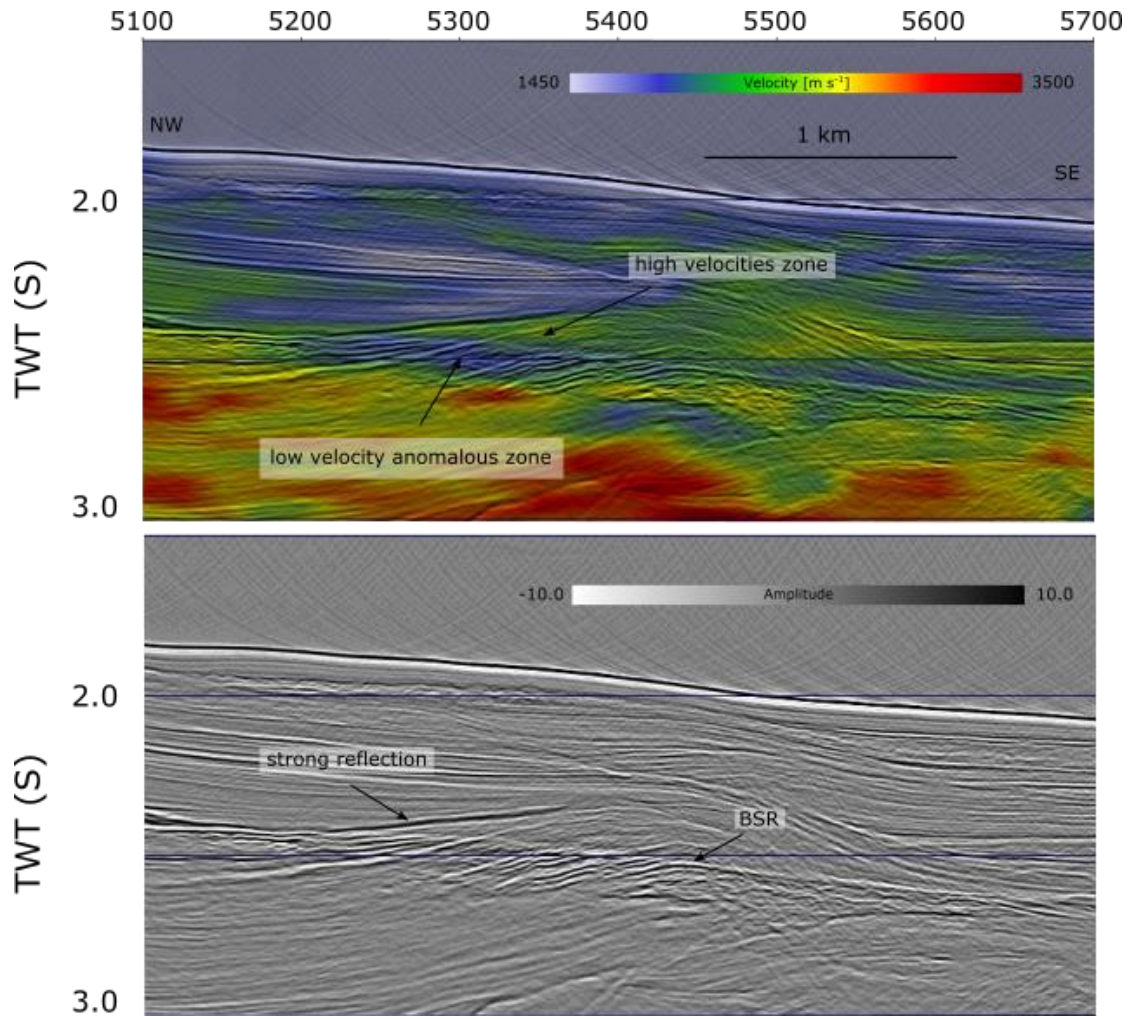


Figure 5.8: High-resolution velocity analysis from zoomed in part of Figure 5.7 (Line BR05-27). White and blue solid lines represent observed BSRs on velocity plot and grey scale section, respectively. Strong reflection is represented by a green dashed line. The low velocity zone beneath the BSR and the high velocity zone above the BSR are pointed out by arrows.

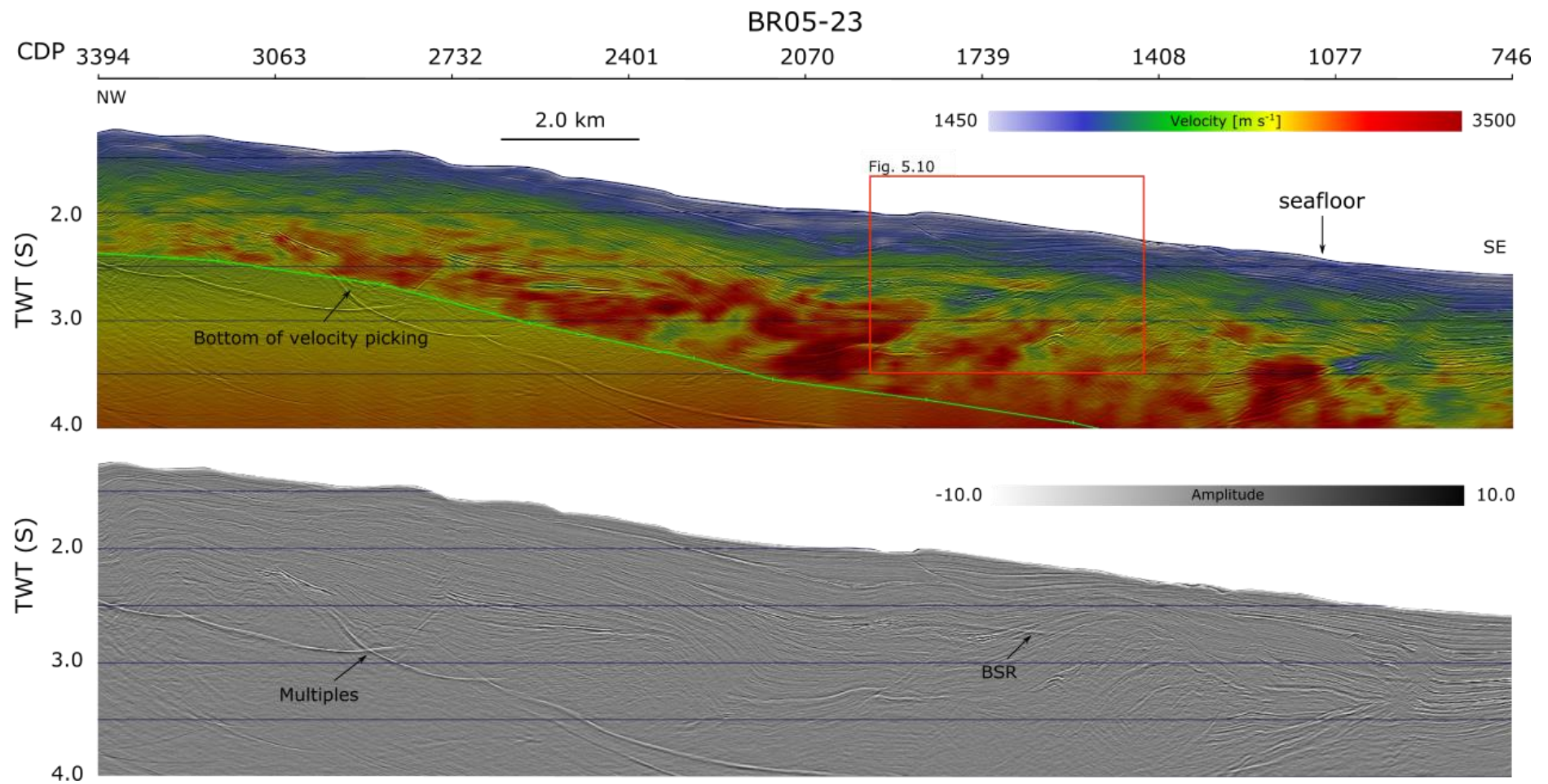


Figure 5.9: High-resolution velocity analysis from BR05-23. This section includes 2648 CDPs (16.55 km) and the beginning is at the cross point with BR05-04. This section is displayed as a colour-plot of interval velocities (above) and a grey scale variable-density plot of the seismic data (below). The colour bar shows a range of velocities between 1450 to 3500 ms^{-1} . The bottom of velocity picking is shown as the green solid line. The red box shows the location of an enlargement given in Figure 5.10.

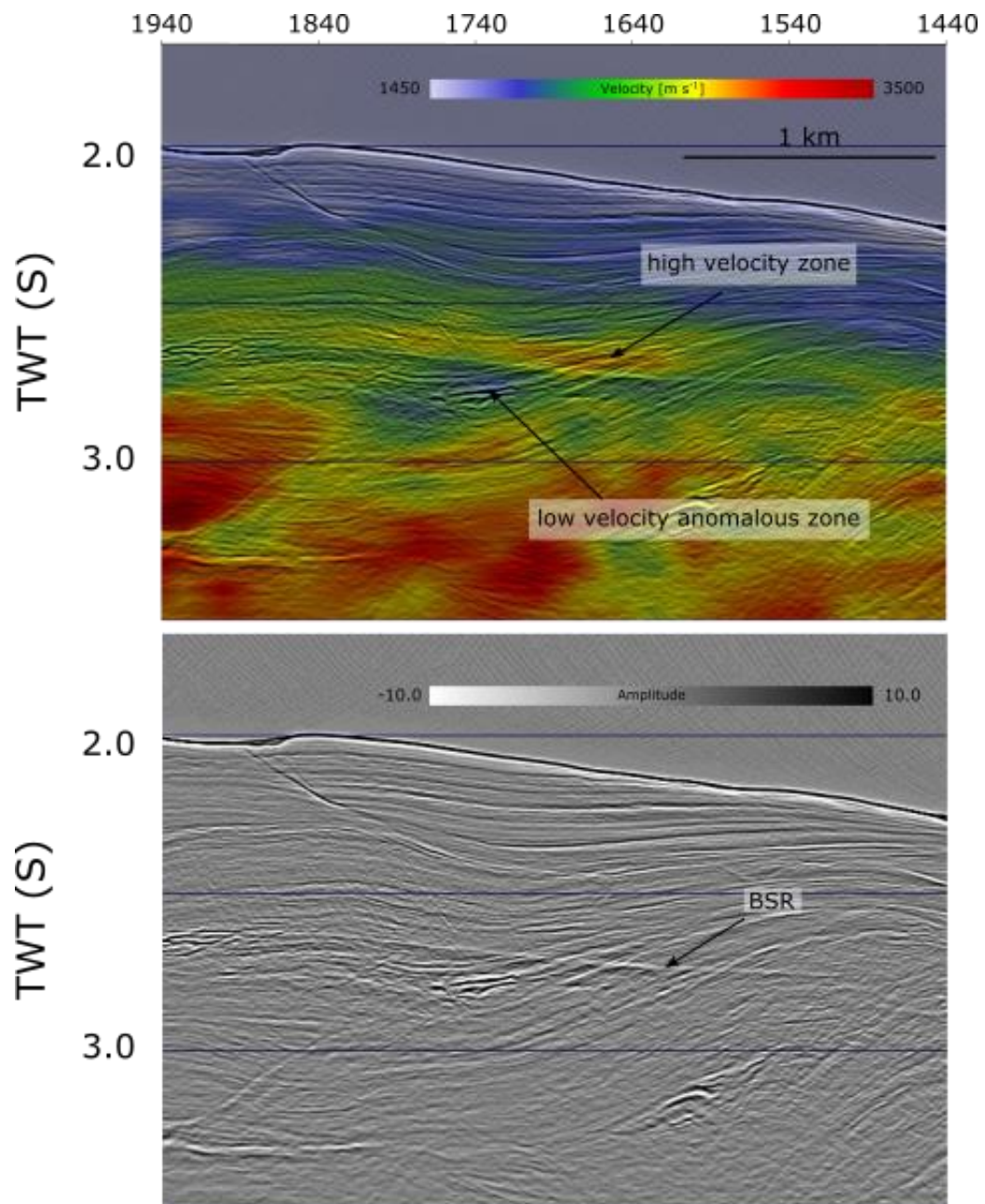


Figure 5.10: High-resolution velocity analysis from zoomed in part of Figure 5.9 (Line BR05-23). White and blue solid lines represent observed BSRs on the velocity plot and grey scale section, respectively. A high velocity zone and low velocity zone are shown by arrows.

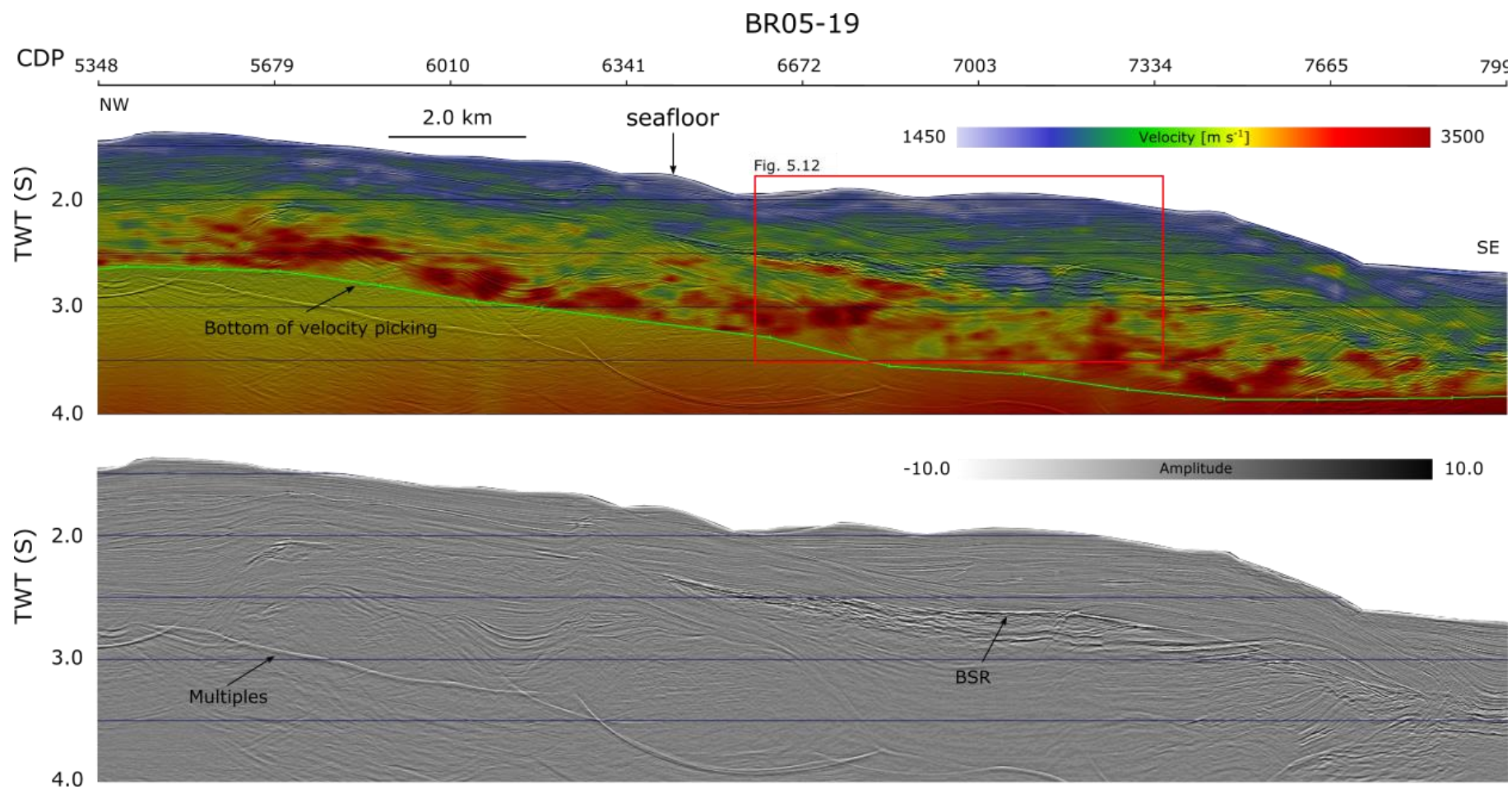


Figure 5.11: High-resolution velocity analysis from BR05-19. This section includes 2648 CDPs (16.55 km) and the beginning is at the cross point with BR05-04. This section is displayed as a colour plot interval velocities (above) and a grey scale variable-density plot of the seismic data (below). The colour bar shows a range of velocities between 1450 and 3500 ms^{-1} . The bottom of velocity picking is shown as the green solid line. The red box shows the location of an enlargement in Figure 5.12.

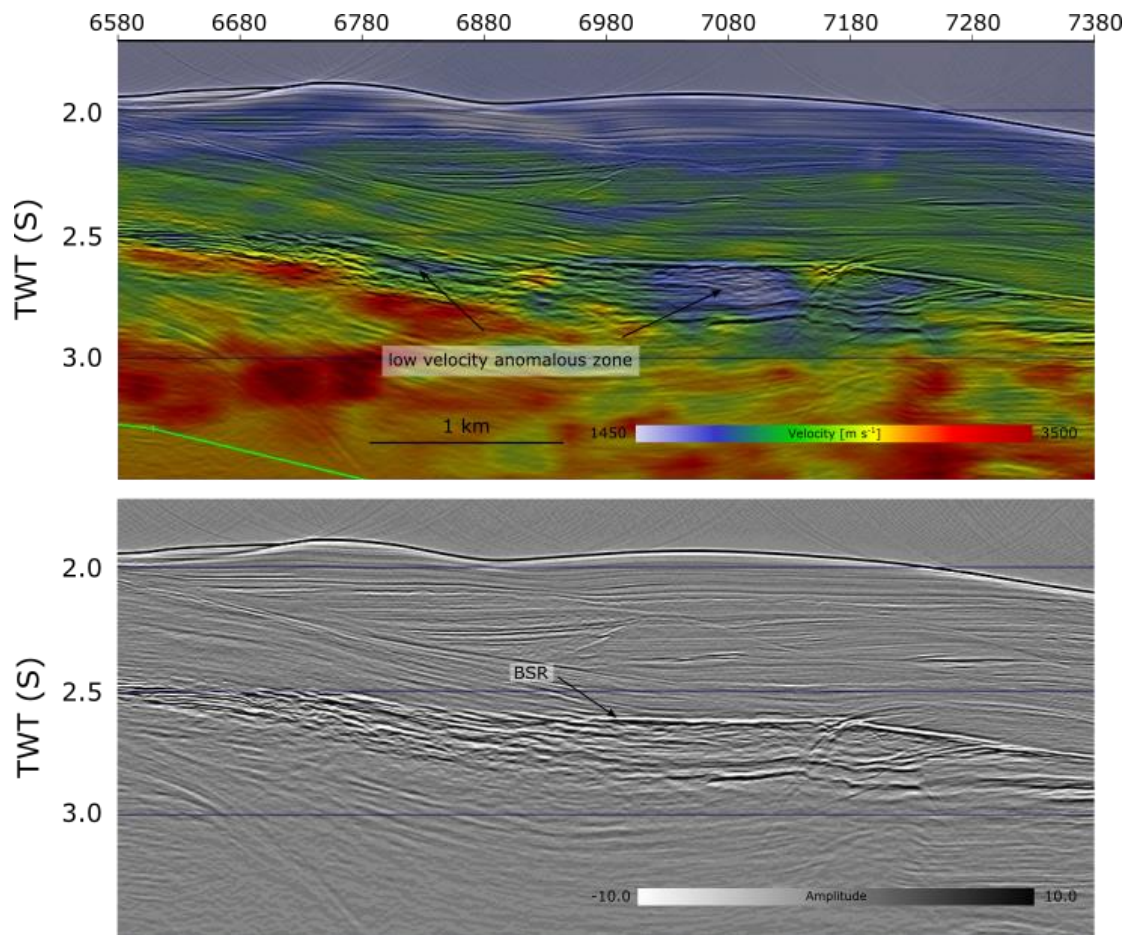


Figure 5.12: High-resolution velocity analysis from red box in Figure 5.11 (Line BR05-19). White and blue solid lines represent observed BSRs on velocity plot and grey scale section, respectively. Low velocity zones are indicated by arrows.

5.7 Observation of BR05-02

The seismic line BR05-02 is a strike-line with respect to faulting and structure, and was used to link the five primary seismic lines together. We also used this line to provide more evidence for the presence of gas hydrates. As the line is long, we have divided it into five sections to show all the key features. Over all, the structures on these sections are simpler than those on the seismic sections in the dip direction.

5.7.1 *Section 1 (CDP 746-3394) of BR05-02*

This section (Figure 5.13) is the southernmost part of BR05-02 and the cross-point with dip direction line BR05-19 is at CDP 3012. As expected, structures on this section are simpler than those on the sections in dip direction. Thrust faults are not as apparent as on the dip direction sections, but a number of small normal faults are identifiable. Channels are developed in the research area (Formann and Pecher, 2012) and we observed two primary channels on this section (Figure 5.13). Two BSRs above the observed channels are identified and we observed a blanking zone above the BSR, and enhanced reflections beneath the BSR (Figure 5.14). In Figure 5.14, we observe that individual reflectors display a polarity switch when crossing the BSR. On the velocity plot, we observe the locations of low velocity anomalous zones usually coincide with the sediments in channels and high velocities are usually above BSRs.

5.7.2 *Section 2 (CDP 3395-6043) of BR05-02*

This section (Figure 5.15) includes two cross points at CDP 3844 and CDP 4654 with BR05-23 and BR05-27, respectively. Few big thrust faults were observed, but small to medium normal faults are developed. An anticline is located at the most northeastern part of this section and we observe a strong BSR beneath the anticline (Figure 5.16). In Figure 5.16, it is also apparent that there are shallow normal faults within the anticline and most of these faults cross cut the BSR. On the velocity plot, a low velocity anomalous zone below the BSR was observed, while a high velocity zone is located above the BSR. We also observe that the velocity of the sediments above the anticline is relatively low (Figure 5.16). We think this is caused by the uncertainty of predicting

velocities with our method, an issue that will be discussed in the Discussion section.

5.7.3 Section 3 (CDP 6044-8692) of BR05-02

This section (Figure 5.17) includes one cross point at CDP 7638 with BR05-37, and this section is the last section of BR 05-02 within our research area. Dipping strata dominate the southwest part of this section, while an anticline is observed at the northeastern part. Small normal faults are developed on this section. We observe a clear BSR at the most southwest of this section in dipping strata and enhanced reflections are located below the BSR. In Figure 5.18, the velocity plot a low-velocity zone is located below the BSR and a high velocity zone exists above the BSR.

5.7.4 Section 4 (CDP 8693-11341) of BR05-02

A submarine channel is located on the seafloor at the southeast part of this section (Figure 5.19). Structures on this section are not complicated, and few faults are observed. The section is dominated by coherent, laterally extensive sedimentary reflections. The observation of BSRs is limited.

5.7.5 Section 5 (CDP 11342-14186) of BR05-02

An anticline is located at the most southeast of this section (Figure 5.20). We observe a long BSR beneath the anticline and a fault-zone above the anticline. Beneath the BSR, enhanced reflections are observed and a blanking zone is existent above the BSR. On the velocity plot, a low velocity zone is located below the BSR, while several high velocity zones are observed above the BSR. We also observe a fault-zone above the anticline.

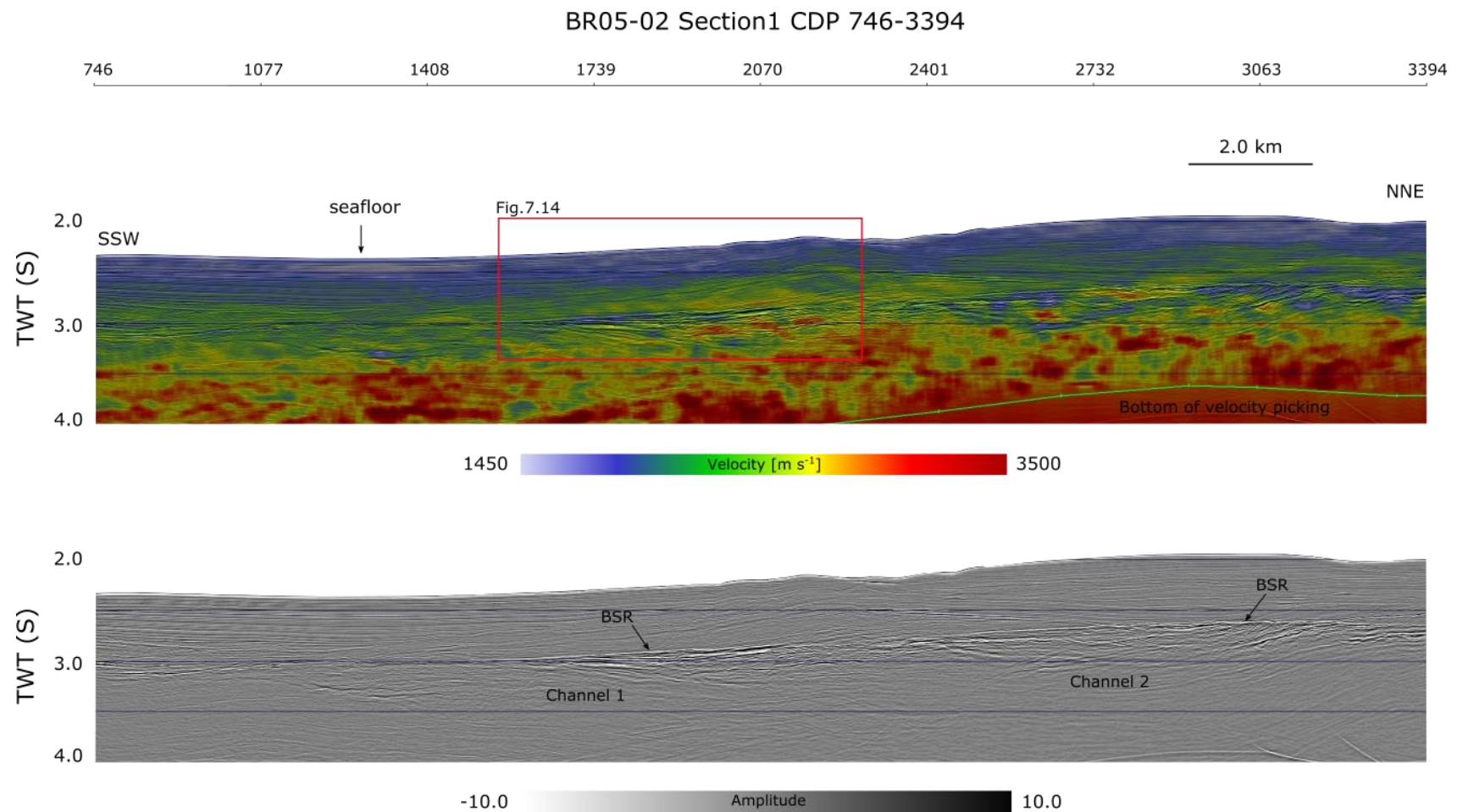


Figure 5.13: High-resolution velocity analysis from BR05-02 section 1. This section includes 2648 CDPs (16.55 km). This section is displayed as a colour plot of interval velocities (above) and a grey scale variable-density plot of the seismic data (below). The colour bar shows a range of velocities between 1450 and 3500 ms⁻¹. BSR is pointed by arrows and the green solid lines on the grey section delineate the outlines of channels. The red box shows the location of an enlargement in Figure 5.14.

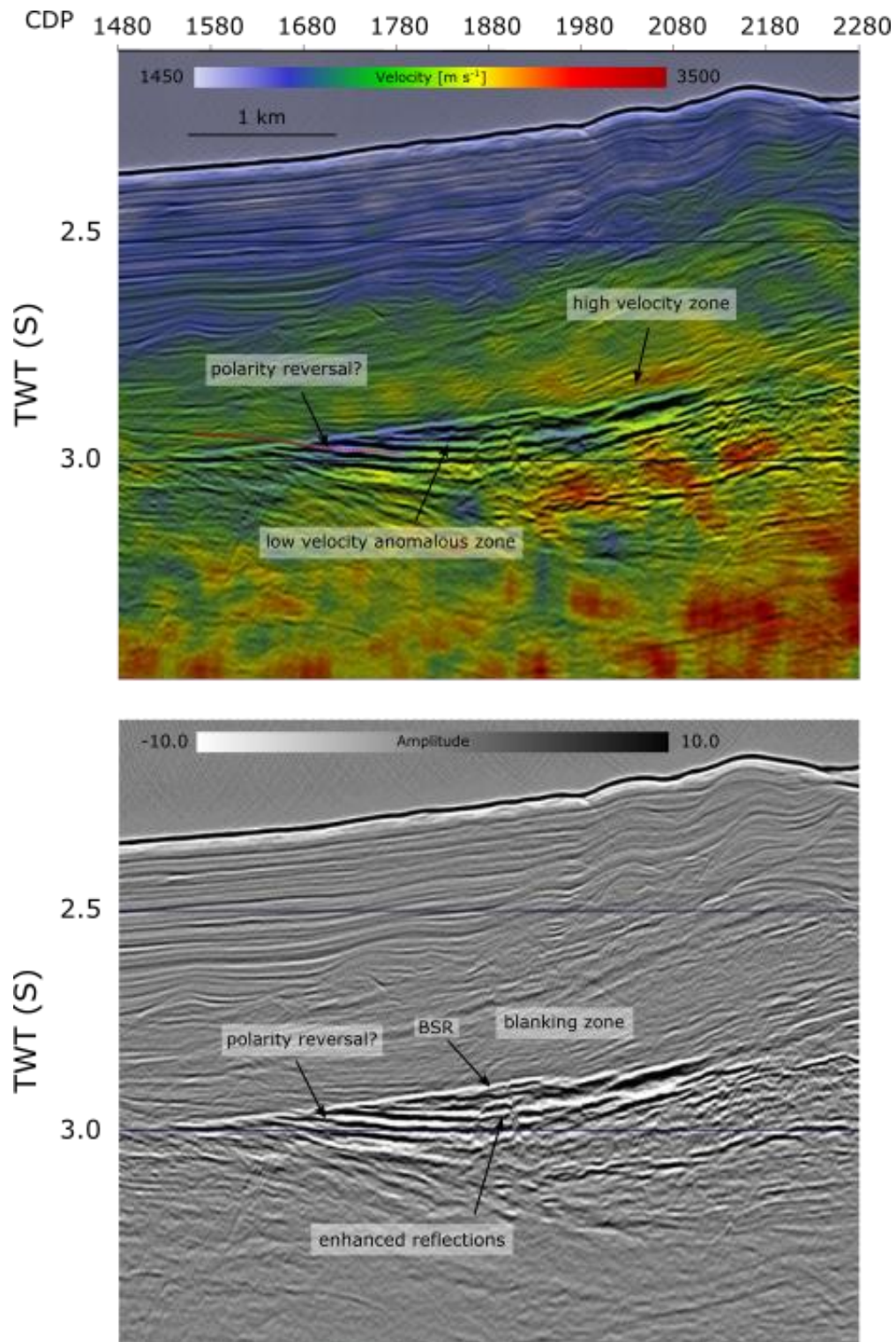


Figure 5.14: High-resolution velocity analysis from the red box in Figure 5.13 (part of BR05-02 section 1). White and blue solid lines represent observed BSRs on velocity plot and grey scale section, respectively. Low velocity anomalous zones and high velocity zones are pointed out by arrows on the velocity plot. The location of enhanced reflections coincides with that of the low velocity anomalous zone. The red dashed line highlights a reflection whose polarity appears to flip when it crosses the BSR

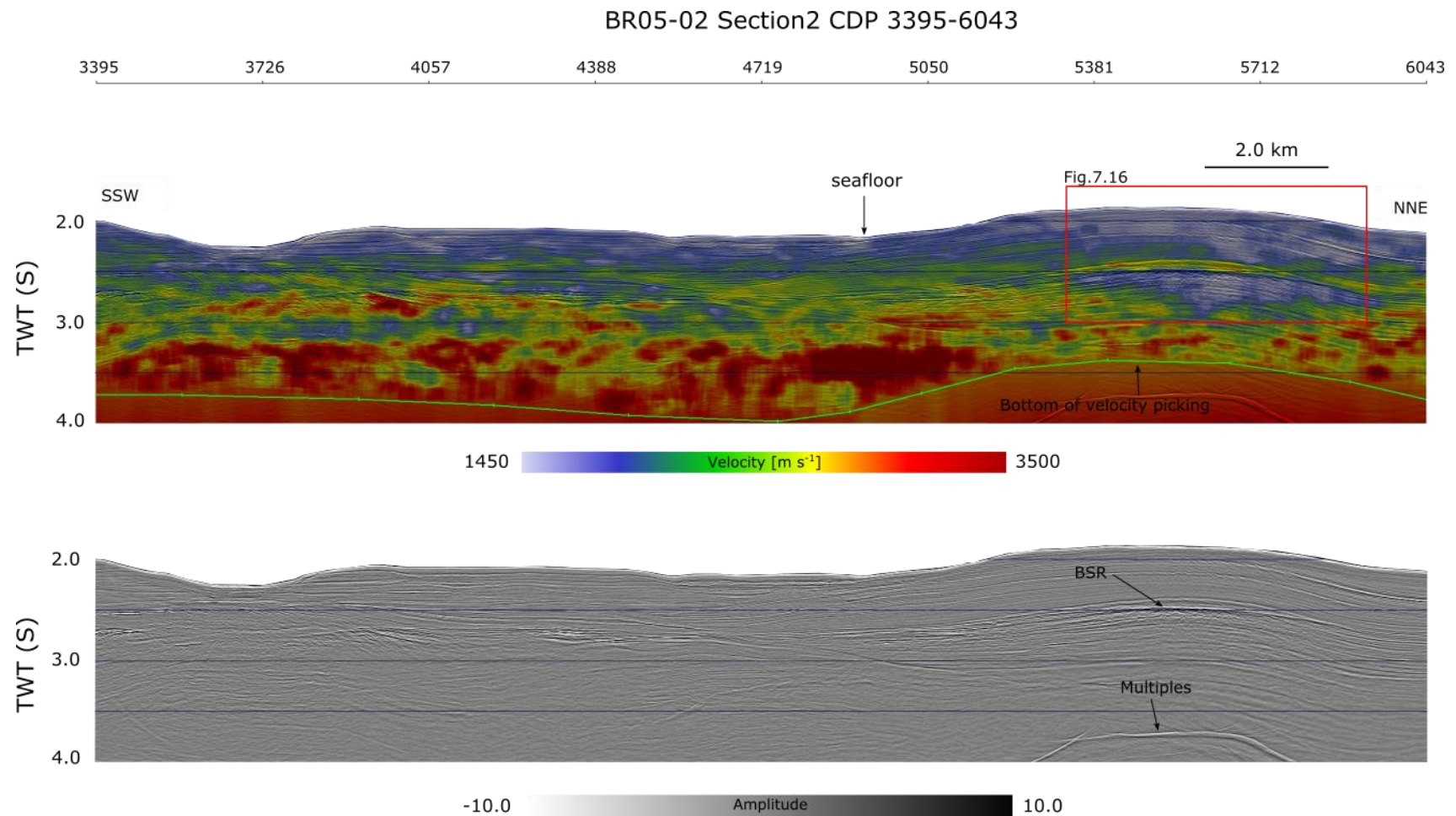


Figure 5.15: High-resolution velocity analysis from BR05-02 section 2. This section is displayed as a colour-plot of interval velocities (above) and a grey scale variable-density plot of the seismic data (below). The colour bar shows that a range of velocities between 1450 to 3500 ms^{-1} . The BSR is pointed out by arrows and the green lines on the colour section represent the bottom of velocity picking. The red box shows the location of the enlargement in Figure 5.16.

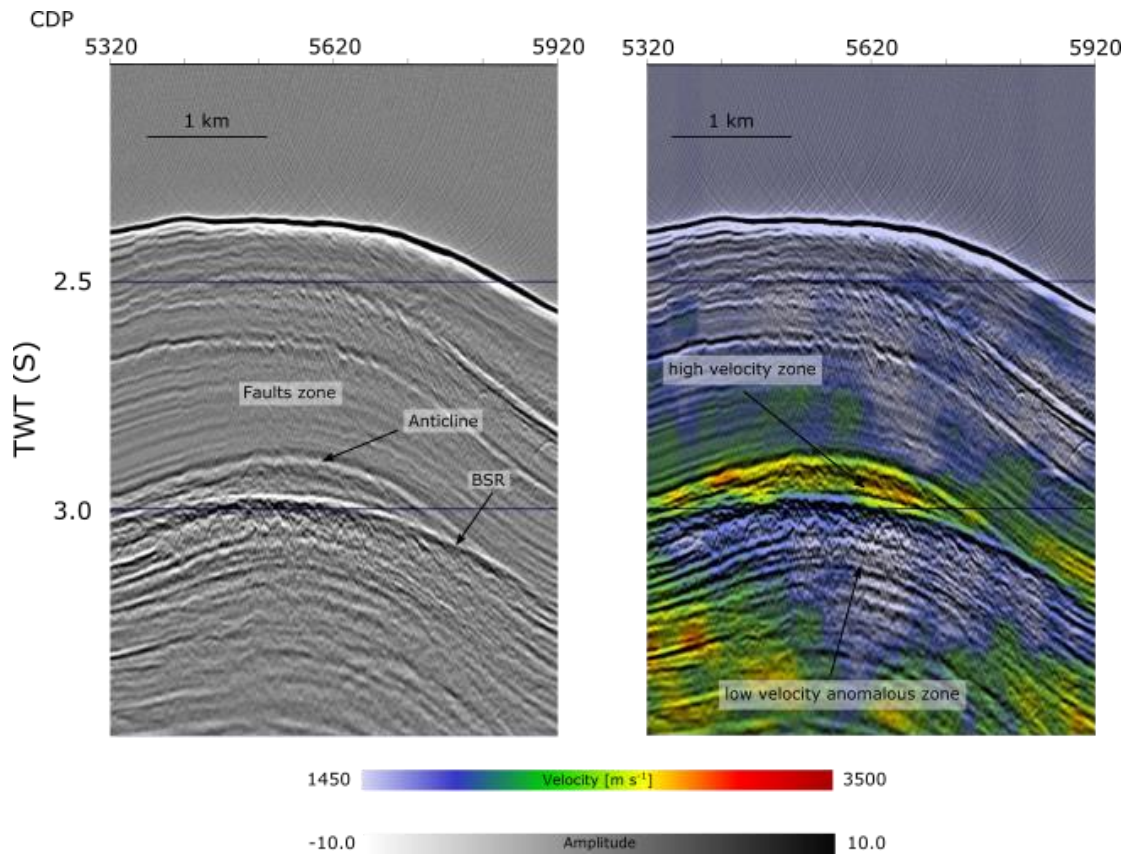


Figure 5.16: High-resolution velocity analysis from red box in Figure 5.15 (part of BR05-02 section 2). White and blue solid lines represent observed BSRs on the velocity plot and grey scale section, respectively. Low velocity anomalous zones and high velocity zones are pointed out by arrows on the velocity plot. A faulted zone is located above the anticline. The black line on the grey section highlights a prominent reflection within the anticline.

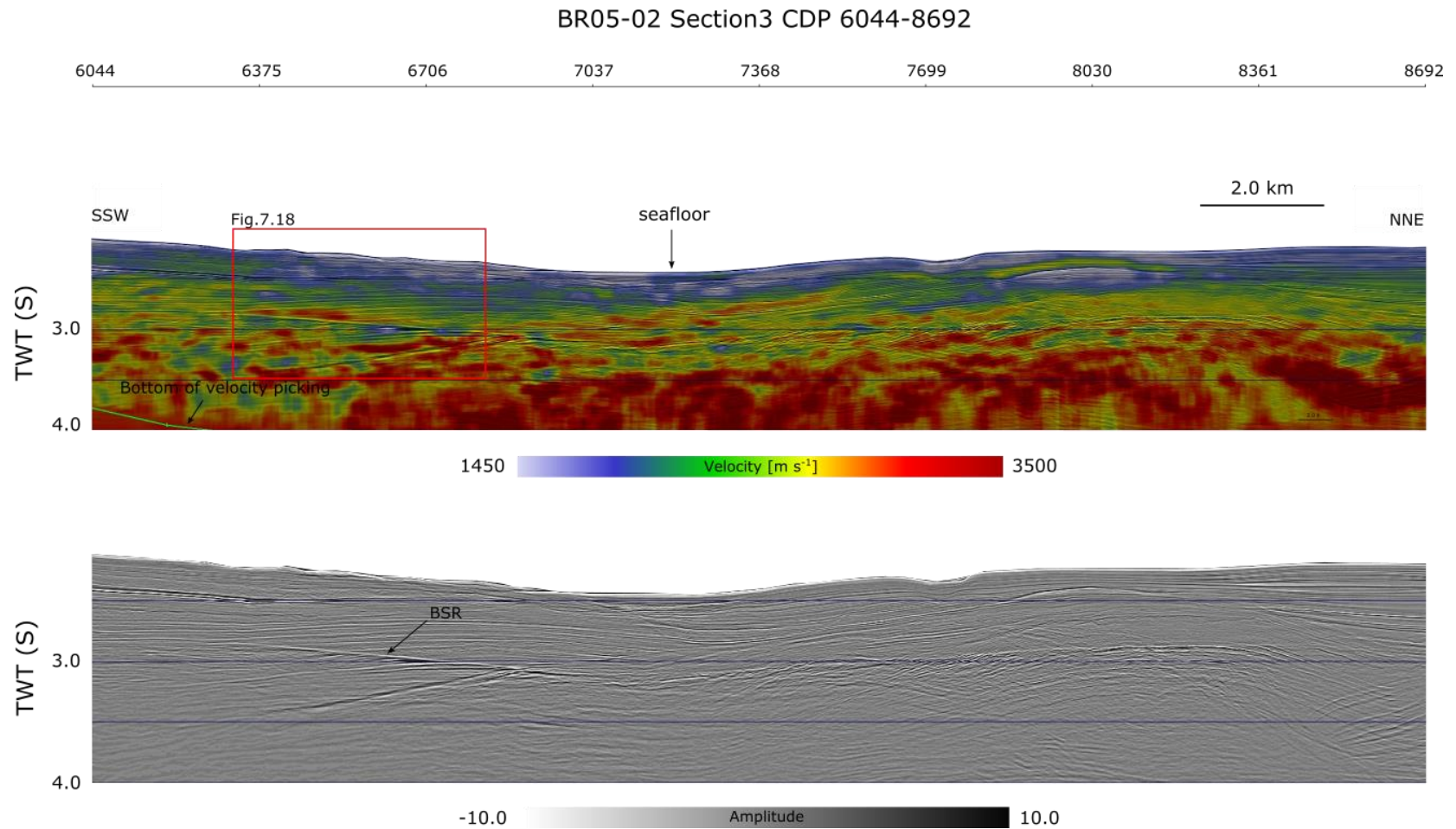


Figure 5.17: High-resolution velocity analysis from BR05-02 section 3. This section is displayed as a colour-plot of interval velocities (above) and a grey scale variable-density plot of the seismic data (below). The colour bar shows a range of velocities between 1450 to 3500 ms^{-1} . A clear BSR is pointed out by the arrow. The red box highlights the location of the enlargement given in Figure 5.18.

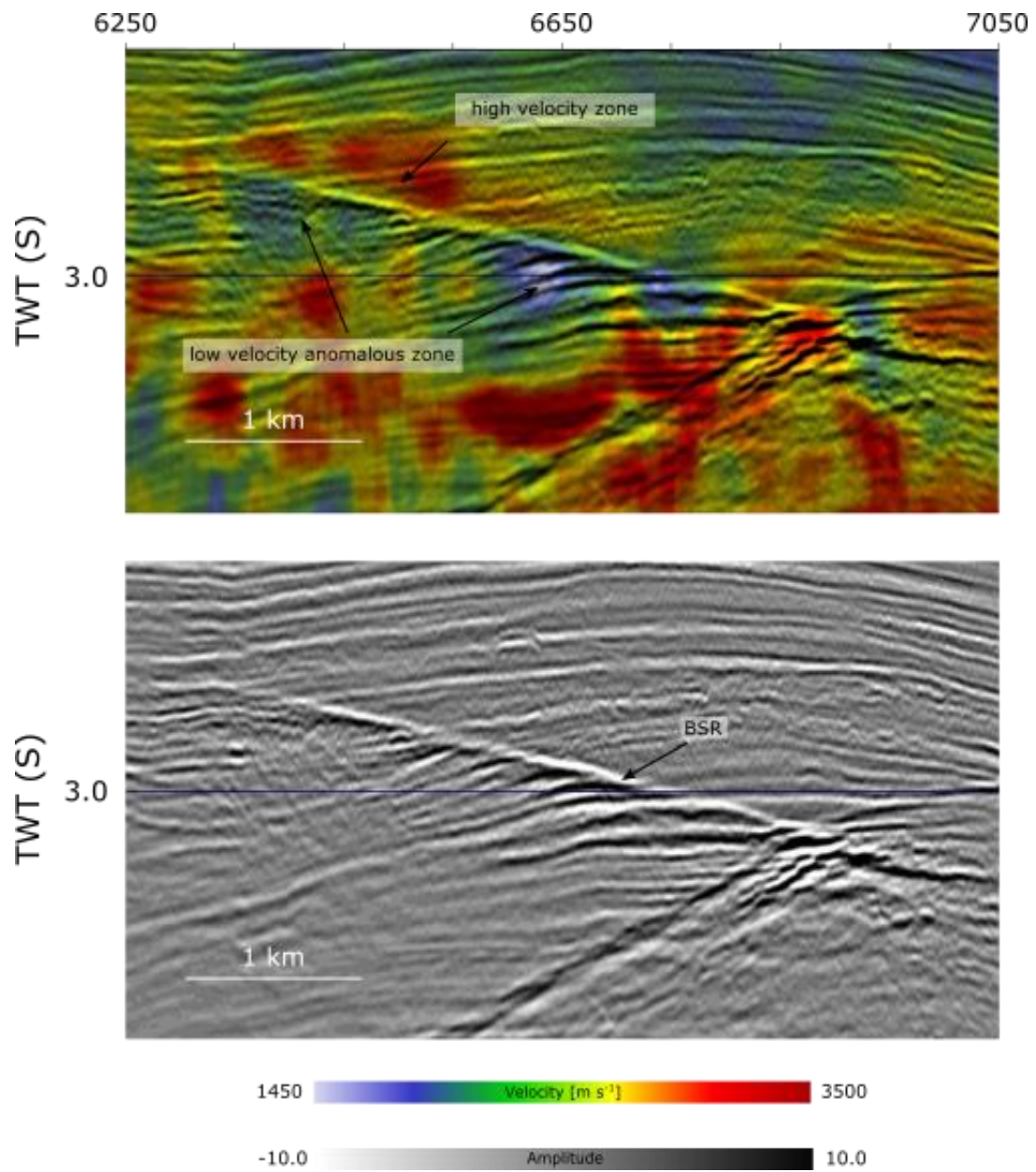


Figure 5.18: High-resolution velocity analysis from red box in Figure 5.17 (part of BR05-02 section 3). White and blue solid lines represent observed BSRs on the velocity plot and the grey scale section, respectively. Low velocity anomalous zones and high velocity zones are pointed out by arrows on the velocity plot.

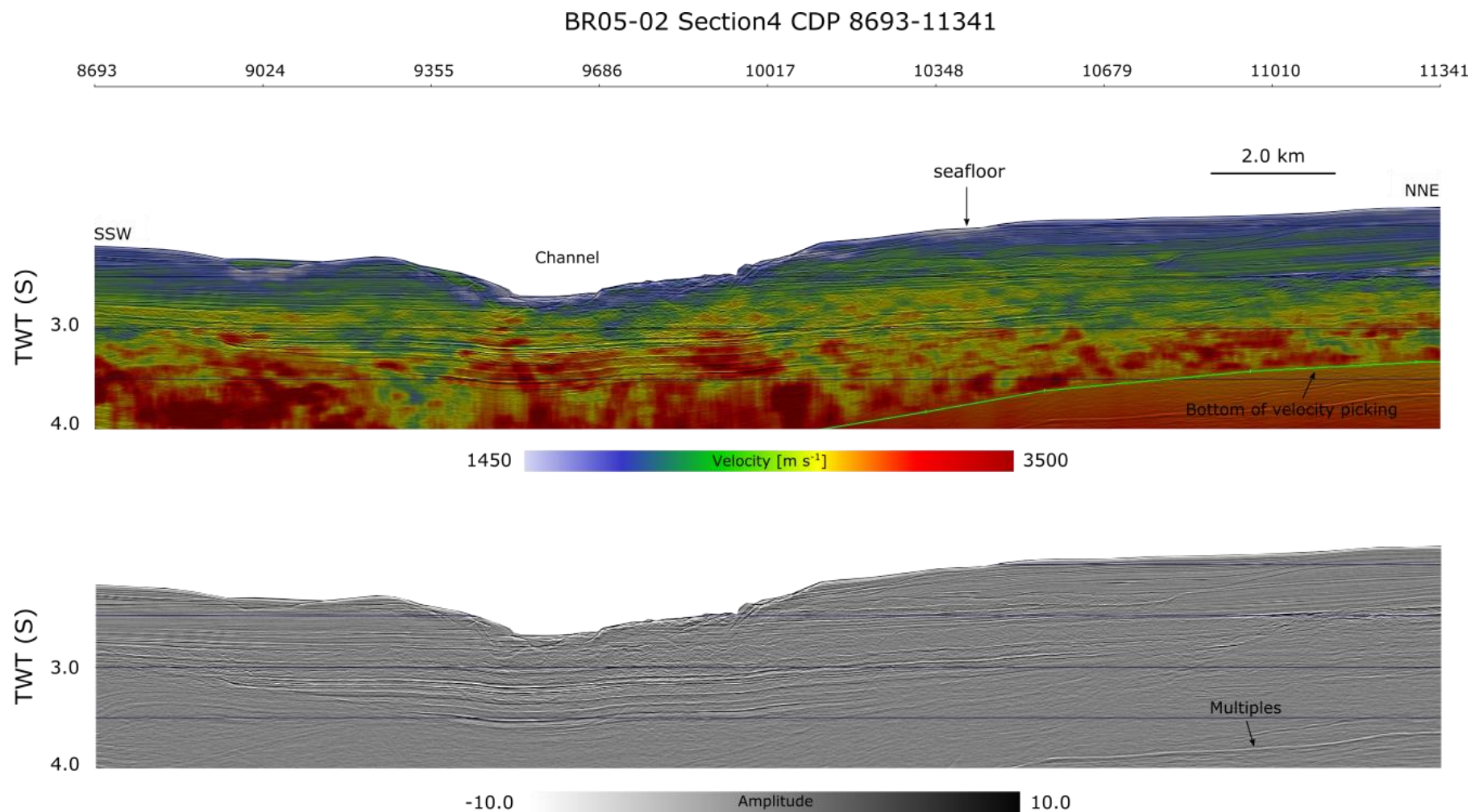


Figure 5.19: High-resolution velocity analysis from BR05-02 section 4. This section is displayed as a colour-plot of interval velocities (above) and a grey scale variable-density plot of the seismic data (below). The colour bar shows a range of velocities between 1450 to 3500 ms^{-1} . Green line represents the bottom of velocity picking.

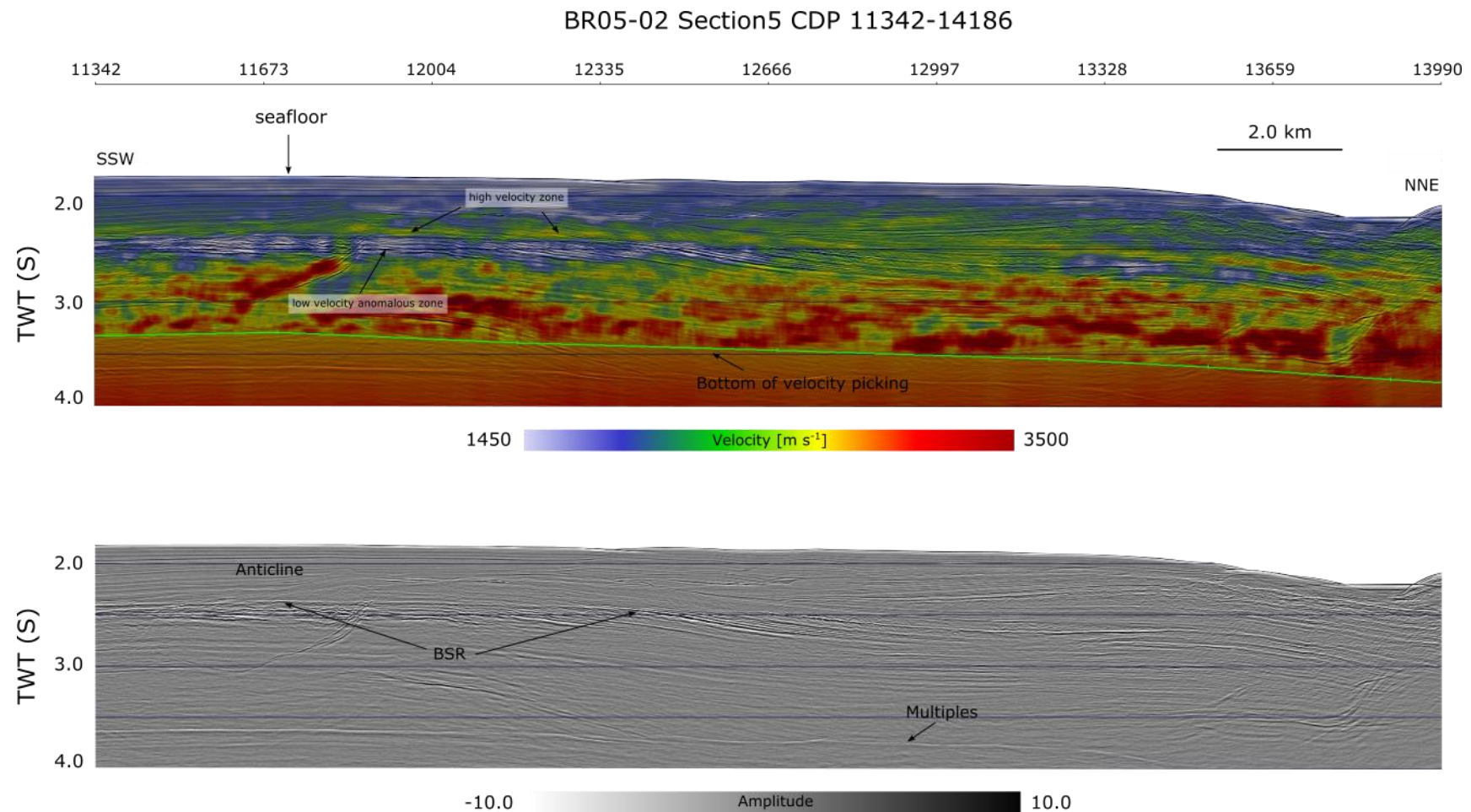


Figure 5.20: High-resolution velocity analysis from BR05-02 section 5. This section is displayed as a colour-plot of interval velocities (above) and a grey scale variable-density plot of the seismic data (below). The colour bar shows a range of velocities between 1450 to 3500 ms⁻¹. Green line represents the bottom of velocity picking. Black line on the grey section represents the outline of an anticline.

6 DISCUSSION

Two key attributes that have historically helped in the identification of highly concentrated gas hydrate deposits are: 1) strong BSRs and 2) structures that focus fluid flow (Pecher and Henrys, 2003). Anomalous reflectivity such as enhanced reflections beneath BSRs (Wood et al., 2002) and blanking zone above BSRs (Lee and Dillon, 2001) provide more evidence for the presence of gas hydrate deposits. Both free gas and gas hydrates within the gas hydrate system may be considered economically viable resources (Beggs, 2008). In this chapter several observations related to gas hydrate on our chosen seismic lines will be interpreted and discussed.

6.1 Double-BSRs system

Anticlines associated with thrust faulting and compressional deformation are seen in the research area (Figure 6.1). The flat strata and undisturbed seafloor above the anticline indicate that compressive is no longer active in this region. Two reflections that are parallel to the seafloor, and have reversed polarity compared to seafloor, are interpreted as double-BSRs. The BSRs beneath the anticline indicate the presence of gas-charged fluids migrating into the anticline system. The observations of enhanced reflections beneath the BSRs provide further evidence for the presence of gas. On the velocity plot, the low velocity zones beneath BSR1 and BSR2, that correspond spatially with the enhanced reflections, are interpreted as free gas accumulations (Figure 6.1 C).

We consider that the formation of BSR2 was earlier than that of BSR1 and that both BSRs were caused by the formation of gas hydrate. When the gas migrated into the gas hydrate stability zone and met enough water, free gas was gradually converting into gas hydrate and BSR2 was formed. On the velocity plot we still can see a high velocity zone between BSR2 and BSR1, which suggests the presence of gas hydrate above BSR2 but beneath BSR1. The formation of a double-BSR could be associated with the admixing of thermogenic gas from a leaky hydrocarbon reservoir or alternatively by depressurization caused by uplift (Macmahon et al., 2015).

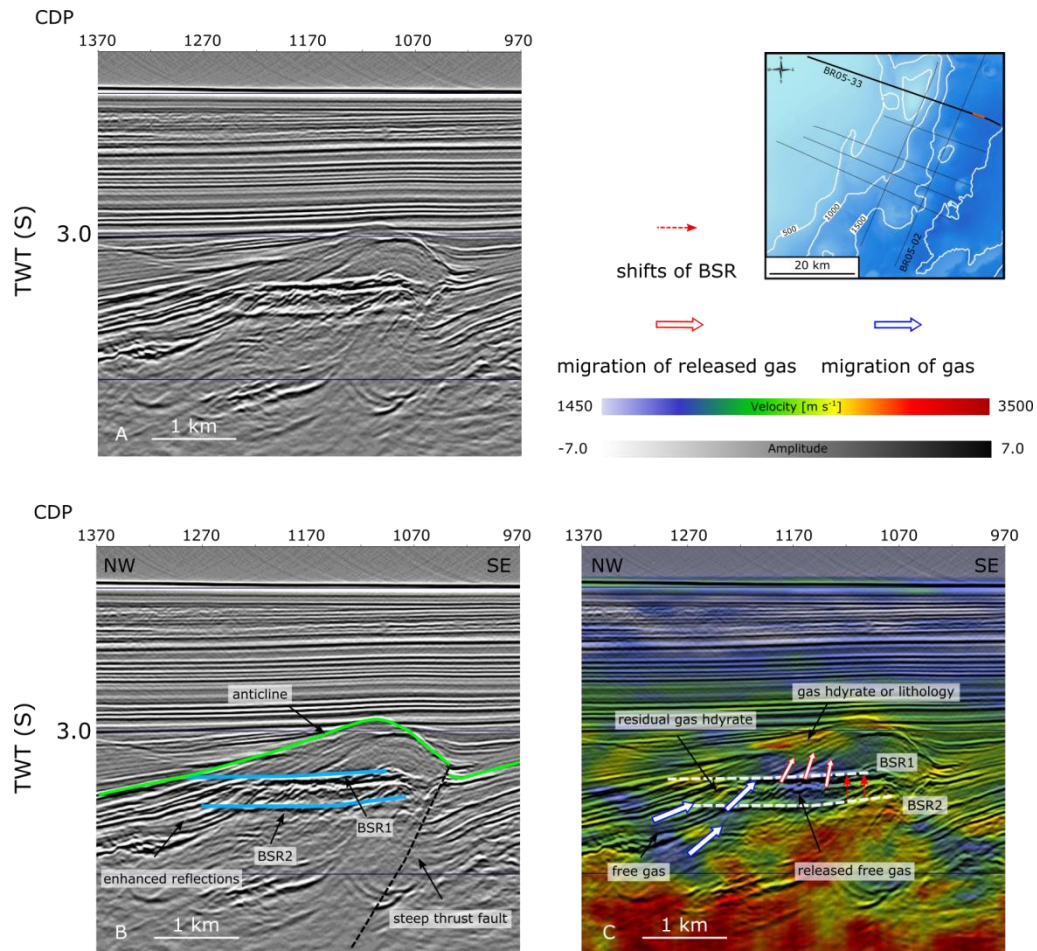


Figure 6.1: Double-BSRs system from BR05-37. A) Top left: Seismic section without interpretation. B) Bottom left: The seismic data with interpretations. Green solid line represents the outline of the anticline and the black dashed line represents the thrust fault. C) Bottom right: Velocity analysis results for the same section. White arrows with blue outlines show the interpreted migration of free gas into the hydrate system. White arrows with red outlines represent the migration of released gas from gas hydrate during uplift at the fault. Red arrows highlight the shift of the base of hydrate stability from BSR2 to BSR1.

Neither scenario can be ruled out, but we prefer the interpretation that the double BSR is caused by uplift and depressurisation in tandem with movement on the thrust fault (Figure 6.1). The double BSR is only observed in the hanging wall of the fault, i.e. the region that has been uplifted and depressurised. In this scenario, the sediments in the hanging wall were depressurised at the time of movement along the fault, resulting in new pressure conditions for the gas hydrate system, and subsequent uplift of the base of hydrate stability and the BSR. The deeper BSR is therefore interpreted as representing the base of hydrate stability before the latest stage of significant movement on the fault, while the shallow BSR represents the present day pressure conditions. The depressurization would have resulted in the release of free gas from gas hydrate. The

released free gas, represented by the low velocity zone between BSR1 and BSR2 (Figure 6.1 C), kept moving up to the location of BSR1. Intriguingly, the low velocity zone above BSR1 may also provide evidence for free gas above BSR1. If this is this case, then the present day base of hydrate stability may actually be above BSR1. The high velocity zones near the top of anticline could be associated with gas hydrate near the base of hydrate stability, but they may also just be locally high velocities from more indurated sediments within the upthrust anticline.

6.2 Indication of concentrated gas hydrate deposits

Seismic section BR05-27 shows classical geophysical characteristics of a gas hydrate deposit. An anticline was observed and it is likely related to thrust faulting that is common in the research area (Figure 6.2 B). This anticline may act as a preferred location for fluid migration and gas hydrate formation. Below the anticline is a reflection parallel to the seafloor reversed polarity reflection, compared to the seabed, that we interpret as a BSR. Several steep thrust faults that cross-cut the BSR were identified (Figure 6.2 B). These faults may act as preferential fluid conduits for the migration of gas and water from greater depths. A reflector displays a polarity reversal when crossing the BSR (Figure 6.2 B). We also observed that the part of this reflector above the BSR has relatively strong reflectivity, of the same polarity as the seabed reflection (Figure 6.2 B). This is a typical geophysical indicator for the presence of a concentrated gas hydrate deposit (e.g.(Boswell et al., 2014)). This strong reflector is likely to be associated with the top of a concentrated gas hydrate deposit. On the velocity plot, we interpret the low velocity zone beneath the BSR as the free gas (Figure 6.2 C). A high velocity zone is observed between the strong reflector and BSR, which we interpret as the region within which a concentrated gas hydrate deposit exists. This gas hydrate reservoir may have commercial potential in the future exploration.

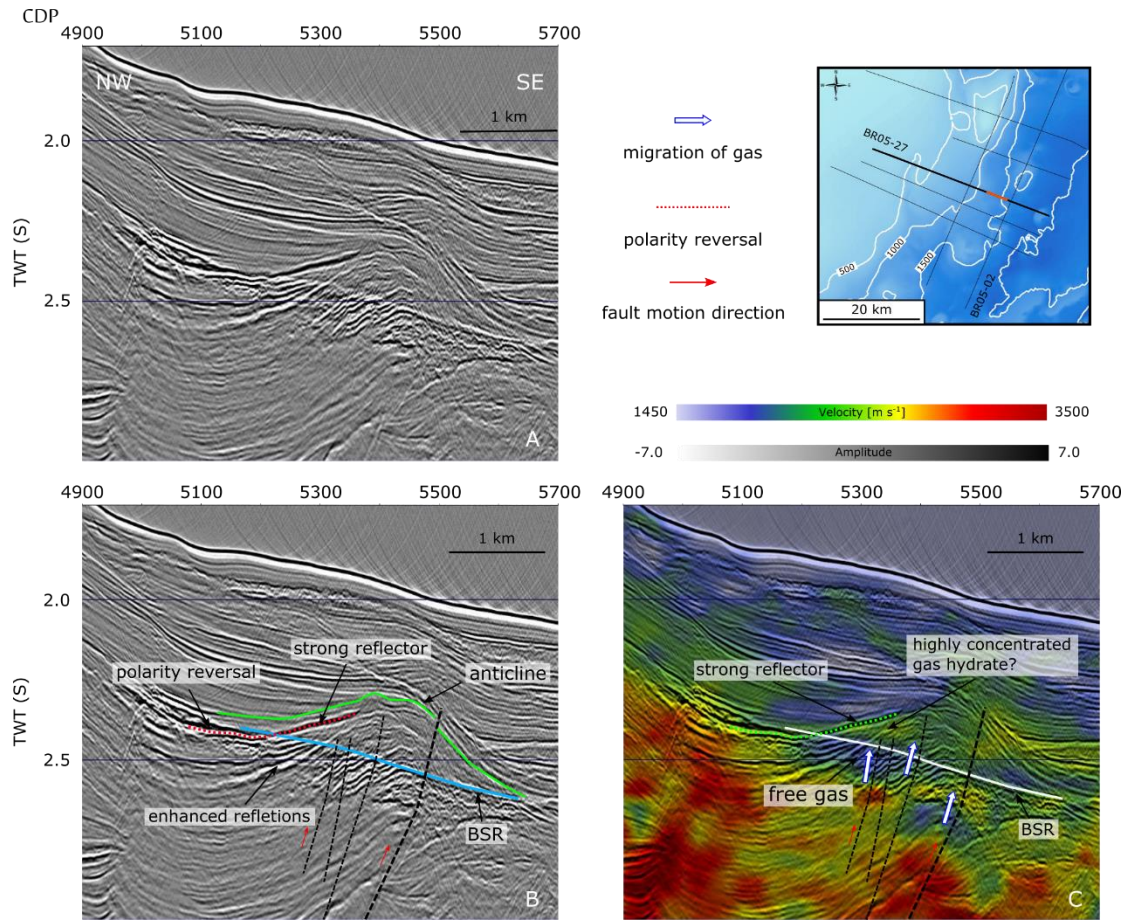


Figure 6.2: Interpreted concentrated gas hydrate deposit at an anticline structure on Line BR05-27. A: The original seismic section without interpretation. B: The seismic data with interpretation. Blue solid line represents the observed BSR. Green solid line delineates the outline of an anticline. The red dotted line shows a reflector that displays polarity reversal as it crosses the BSR. C: Velocity analysis for the same section from plot B. White arrows with blue outlines indicate the interpreted migration of gas. Red arrows highlight motion direction of faults. The green dotted line shows the same reflection as that highlighted by the red dotted line in (B).

According to our observations and interpretations, we identify the following geophysical signatures for locating concentrated gas hydrate deposits: (a) existence of BSRs; (b) strong reflections above BSRs in gas hydrate stability zone; (c) enhanced reflections (bright spots) below BSRs; (d) appropriate velocity anomalies associated with the enhanced reflections above the BSR.

6.3 Importance of dipping strata and faulting in the formation of gas hydrate

6.3.1 Dipping strata

BSR1 observed on Line BR05-33 has formed in dipping strata (Figure 6.3). Reflections of sediments cross-cutting BSR1 help us to identify the BSR and the high amplitude of BSR1 indicates a strong impedance contrast between the sediments above BSR1 and those below it. Enhanced reflections and a low velocity anomaly are also observed below the BSR (Figure 6.3 B). These observations indicate the existence of gas within the extent of the low velocity zone. Although anomalously high velocity zones above the BSR are not obvious, there are some irregular, strong reflections directly above the BSR (Figure 6.3 C). These short reflection segments (Figure 6.3 C) point towards the presence of gas hydrates very close to the BSR. The top of this zone likely represents the top of localised gas hydrate deposits.

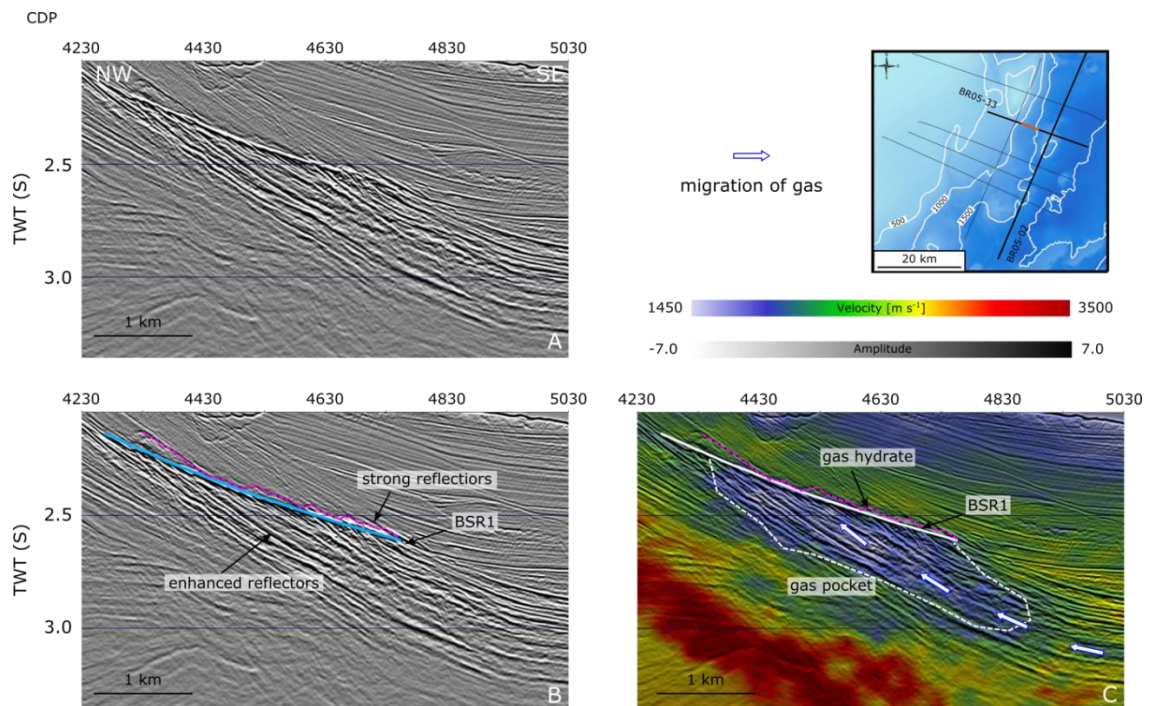


Figure 6.3: Gas hydrate system in dipping strata of Line BR05-33. A: The original seismic section without interpretation. B: The seismic data with interpretation. Blue solid line represents the observed BSR. Dashed purple line delineates strong reflectors above the BSR. C: Velocity analysis results for the same section from plot B. White solid line represents the BSR. Blue arrows indicate the migration of gas. White dashed line delineates the gas pocket beneath the BSR.

It has been suggested that gas hydrate is able to form an effective seal (Grauls, 2001), and free gas may be trapped beneath the hydrate layer. The self-sealing nature of a hydrate cap (Swinkels and Drenth, 2000) is favourable to the accumulation of gas. Therefore, we believe it is likely that biogenic gas (and possibly also deeper thermogenic gas) has accumulated in a thick package beneath the BSR due to a permeability contrast caused by overlying gas hydrates that clog the pore space. Even in the absence of highly-concentrated gas hydrate deposits at this location, the gas pocket below the BSR could be a potential target for future exploration.

6.3.2 Faulting

A section of Line BR05-02 (Figure 6.4) shows a fold structure that is favourable to focus fluids. A flexural extension fault zone, which was produced by the extension, dominates the upper section from 2.0 to 2.5 s TWT (Figure 6.4 B). A reflection located at around 2.5 s TWT is interpreted as a BSR, as it is parallel to the seabed and has reversed polarity compared to the seafloor (Figure 6.4 B). Faults are developed in the extension zone and we picked out a number of small faults, which display clear offset on the reflections (Figure 6.4 B). On the velocity plot, high velocity zones are observed above the BSR, while a low velocity zone is located beneath the BSR (Figure 6.4 C). It appears the low velocity zone is associated with free gas beneath the BSR, as some enhanced reflections, which are caused by free gas are also observed. The high velocity zones above BSR are likely to coincide with concentrated gas hydrate deposits. However, it is difficult to discriminate between gas hydrate effects and lithology effects, as high velocity sediments such as carbonates also can cause a high velocity zone.

Several faults crossing the BSR are observed (Figure 6.4 B) and we think they play a role in creating pathways for the migration of free gas from the free gas zone into the gas hydrate stability zone. These faults likely act as links between the free gas reservoir below and the gas hydrate system above. In terms of the gas reservoir beneath the BSR, the fold structure provides a good place for the accumulation of gas.

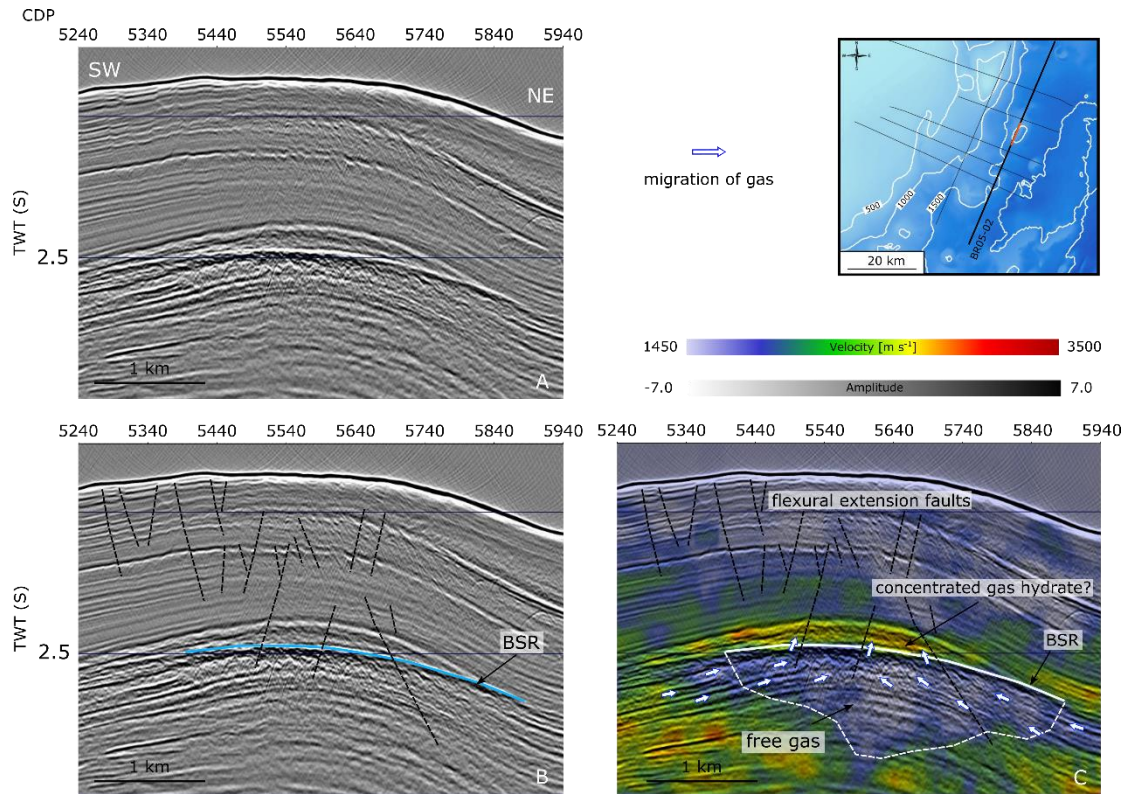


Figure 6.4: Gas hydrate system at a fold structure on Line BR05-02. A: The original seismic section without interpretation. B: The seismic data with interpretation. Blue solid line represents the observed BSR. Faults are represented by black dashed line. C: Velocity analysis results for the same section of plot B. White solid line represents the observed BSR. Blue arrows show the migration of gas. White dashed line delineates the outline of gas pocket beneath BSR. High velocity zones above the BSR are interpreted as the concentrated gas hydrate deposits, while the low velocity beneath BSR is interpreted as the free gas reservoir.

6.4 Distinguishing gas hydrate-derived velocity anomalies from lithologically-derived anomalies

The BSR observed on BR05-33 is located at an anticline (Figure 6.5 B). This anticline is associated with a large-scale thrust fault. Reflections above the anticline indicate that thrust faulting is no longer active or offset below seismic resolution. On the velocity plot, low velocity zones related to free gas are observed below the BSR (Figure 6.5 C). Above the BSR, high velocity zones are observed. We note that these high velocities could be associated with changing lithology, as the reflections in the high velocity zone can be tracked to the northwest to another high velocity zone that appears to be the result of lithological changes (Figure 6.5 C). However, the high velocity zone located further to the northwest could also be explained by higher compaction that is caused by

depth of burial. Thus, although we expect the high velocity zone directly above the BSR to be the result of gas hydrates, we cannot rule out the possibility that the high velocities simply arise from lithological effects.

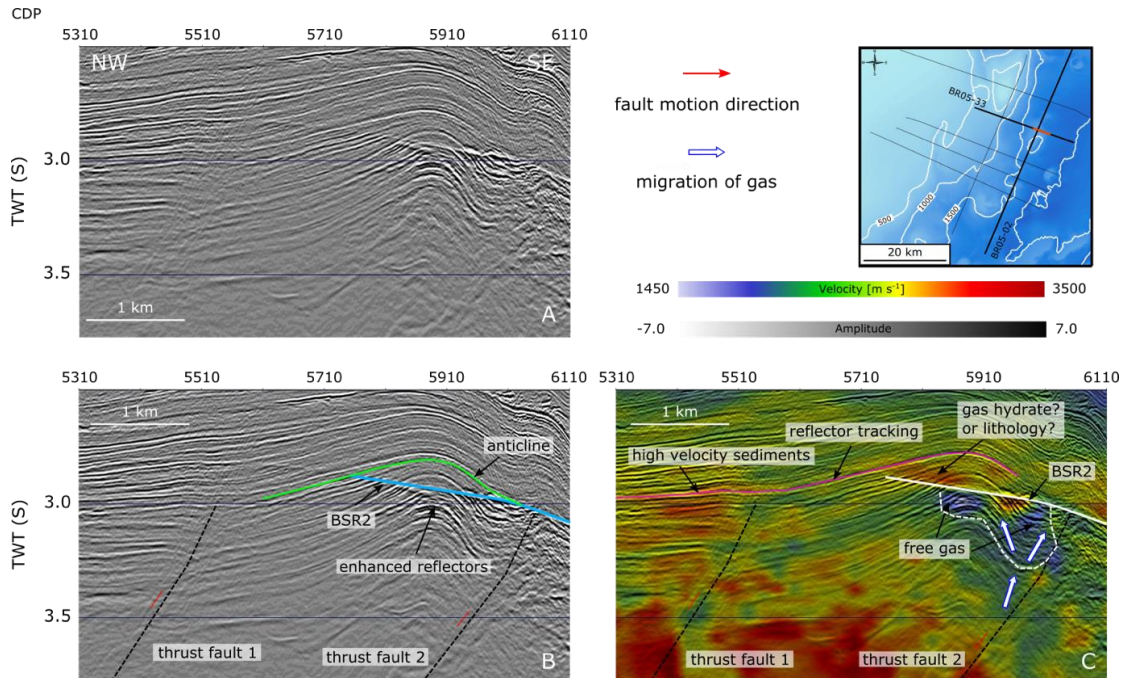


Figure 6.5: Gas hydrate at an anticline structure on Line BR05-33. A: The original seismic section without interpretation. B: The seismic data with interpretation. Blue solid line represents the observed BSR. Green solid line delineates the outline of the anticline. Black dashed lines show the thrust faults. Small red arrows indicate the motion direction of faults. C: Velocity analysis results for the same section from plot B. White solid line represents the BSR. Purple solid line shows the reflector tracking. White arrows indicate the migration of gas. The white dashed line delineates the outline of the gas pocket beneath the BSR.

We propose that the source of the gas in this area could be associated with the deeper hydrocarbon system and also in-situ biogenic gas. Two possible paths, thrust fault 1 and thrust fault 2 (Figure 6.5 B), for the migration of gas from deeper hydrocarbon system were identified. However, we suggest that fault 2 is a more efficient path for gas migration than fault 1. We argue that the low velocities around the foot wall of fault 1 are the result of shallower and younger sediments rather than free gas. We also note that the velocities above the BSR are higher than those at the top of the hanging wall of the fault (Figure 6.5 C). This could be explained by gas hydrate saturation in the sediments. Another explanation for the higher velocities is the effect of combining gas hydrate and lithology (higher velocity sediments). In order to support this point, we show a reflector

tracking from the sediments with high velocities to the gas hydrate deposit (Figure 6.5 C).

6.5 Gas Hydrate deposits in turbidite sequences

In general, turbidite sand sequences can be good reservoir zones for conventional hydrocarbon resources in deep-water. Turbidites characterised by channelized facies are considered as good reservoirs in the East Coast Basin (Uruski and Bland, 2011). Titihaoa-1 drilled in offshore Wairarapa encountered a prominent gas show in Middle Miocene turbidites. Middle and Late Miocene turbidites in Tawatawa-1 also had significant gas shows (Uruski and Bland, 2011). The seismic data in Line BR05-02 (Figure 6.6) show channelized facies that have been analysed previously (Fohrmann and Pecher, 2012). Enhanced reflections are observed within the channel below the BSR (Figure 6.6 B). We interpret these enhanced reflections as free gas, as on the velocity plot the corresponding location is dominated by a low velocity zone (Figure 6.6 C). A polarity reversal, which is characteristic of a gas hydrate related BSR, is observed at the most southwest part of the section (Figure 6.6 B). One prominent reflector (red dotted line) displays a polarity reversal when crossing the BSR. On the velocity plot, the locations of low velocity zones and high velocity zones are consistent with that shown previously by Fohrmann and Pecher (2012) (e.g. their Figure 6). Low velocity zones are located beneath the BSR, while high velocity zones primarily lie above the northeast part of the BSR (Figure 6.6 C).

The high velocity zones were interpreted as concentrated gas hydrate deposits by Fohrmann & Pecher (2012). However, as argued in the earlier section, the combination of lithology and gas hydrate is likely to contribute to high-velocity zones. On the velocity plot, we also observed that the high velocity zones are usually located near faults (Figure 6.6 C). It is therefore likely that there is a relationship between faults and the distribution of gas hydrate deposits, as faults are able to provide pathways for the migration of fluids.

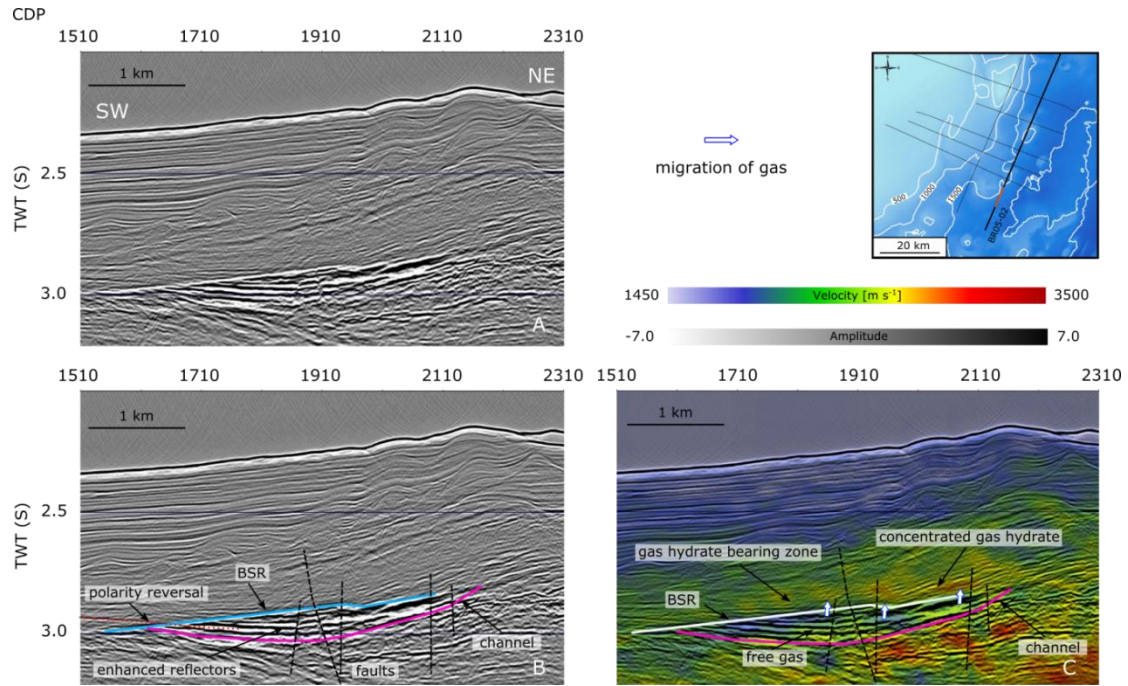


Figure 6.6: Gas hydrate system in turbidite deposits from BR05-02. A: The original seismic section without interpretation. B: The seismic data with interpretation. Blue solid line represents the observed BSR. The red dotted line represents the polarity reversal. Faults are represented by black dashed lines. The purple solid line delineates the outline of the channel interpreted in Fohrmann and Pecher (2012). C: Velocity analysis for the same section from plot B. White solid line represents the observed BSR. Blue arrows show the migration of gas. The location of low velocity zones and high velocity zones are similar to the observation from (Fohrmann and Pecher, 2012).

6.6 Blanking zone and amplitude variation

The seismic sections (Figure 6.7) from BR05-23 show relatively complicated structures, which are dominated by thrust faults. A reflection parallel to the seafloor was observed and this reversed polarity reflection is interpreted as a BSR (Figure 6.7 B). On the seismic section, two primary thrust faults and a number of smaller faults were identified (Figure 6.7 B). Some of these faults cross cut the observed BSR and could play a role in providing pathways for the migration of fluids. On the velocity plot, two low velocity zones were observed, while we only observed one high velocity zone above the BSR (Figure 6.7 C). As the low velocity zones correspond to regions of enhanced reflections in the seismic data (Figure 6.7 B), we interpret the low velocity zones as sediments bearing free gas. We interpret the high velocity zone as sediments bearing gas hydrate. The amplitude of the BSR weakens towards the northwest until it eventually disappears. We propose that this is the result of a reduction in the saturation of free gas in the

sediments to the northwest. As the saturation of free gas in the sediments in the northwest is predicted to be low, no overlying high velocity zone (such as that seen further to the southeast) is absent (Figure 6.7 C). The BSR is located in dipping strata, which is favourable for focusing fluid flow into the gas hydrate system. The strongest high velocity anomaly above the BSR exists near the south-eastern end of the section, in an area where relatively steeply-dipping strata cross-cut the BSR. We suggest that the high angle of these strata with respect to the BSR means that they are efficient pathways for upward migration of gas-charged fluids into the hydrate stability zone. This process, we interpret, results in a zone of concentrated gas hydrate in these steeply-dipping strata.

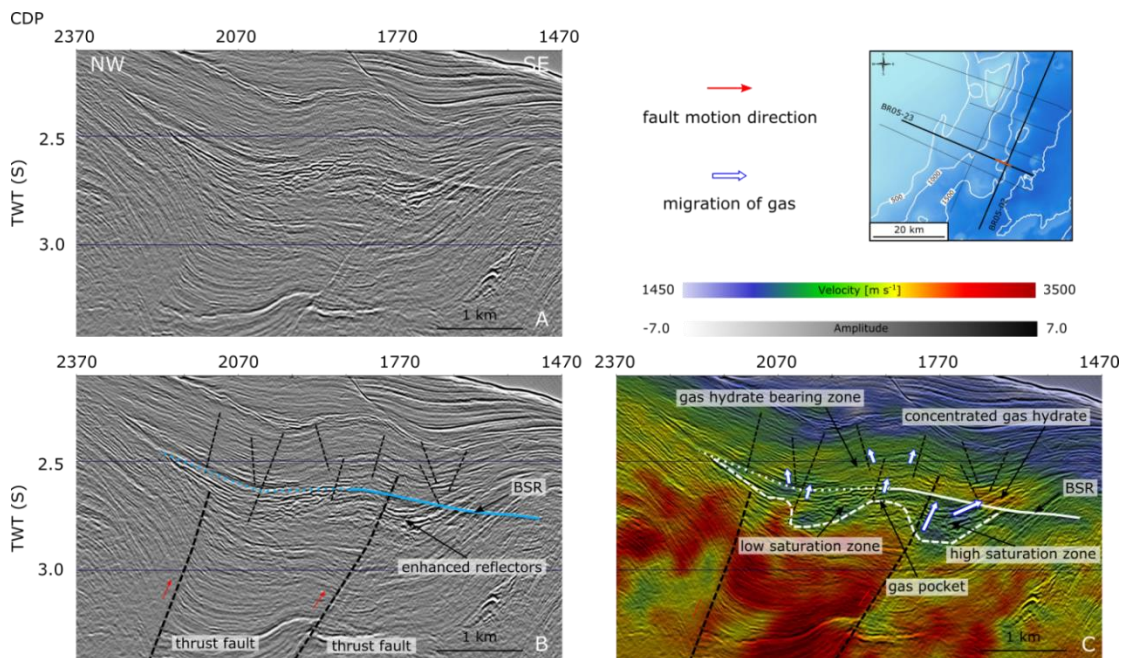


Figure 6.7: Concentrated gas hydrate deposit and low saturation gas hydrate deposits from BR05-23. A: The original seismic section without interpretation. B: The seismic data with interpretation. Blue solid line represents the observed BSR, while blue dot line represents the weakening BSR. Faults are represented by black dash line. C: Velocity analysis for the same section from plot B. White dash line delineates the outline of gas pocket beneath BSR. Blue arrows show the migration of gas.

6.7 Idealized scenarios for the formation of concentrated gas hydrate

Figure 6.8 is a cartoon for the formation of concentrated gas hydrate deposits in dipping strata, based on our observation of dipping strata from seismic line BR05-33 (Figure 6.3). The layers are interpreted as interbedded permeable sandstones and relatively

impermeable shales. Gas migrates upwards along the sandstone layers. When the gas crosses the BSR and enters into the gas hydrate stability zone, it converts into gas hydrate deposits. Due to the increasing saturation of gas hydrate in the sandstone above BSR, the permeability of the sandstone is decreased. Therefore, it creates a seal for the permeable layers and these layers will become gas charged beneath the BSR.

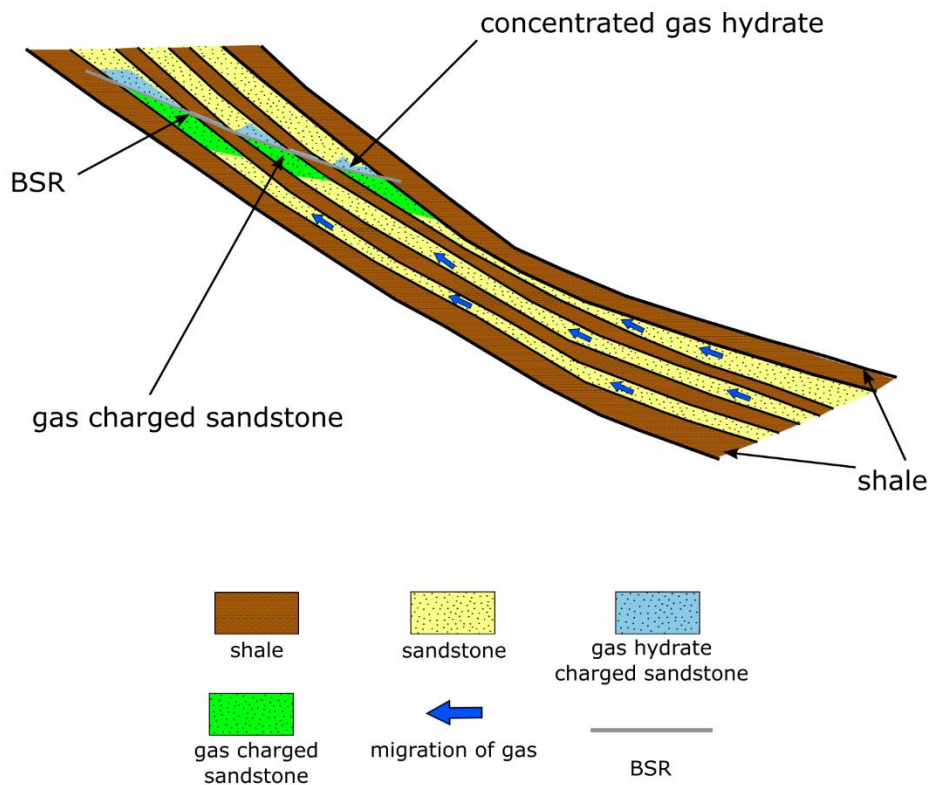


Figure 6.8: Cartoon for the formation of concentrated gas hydrate deposits that are based on Figure 6.3. The diagram shows interbedded sandstone and shale. The blue arrows represent the migration of gas along the permeable layers. The blue solid line represents the BSR that is the bottom of gas hydrate stability zone. Gas builds up in the sandstone beneath the BSR, and the sandstone above the BSR hosts concentrated gas hydrate that forms from migration of gas from below.

Figure 6.9 is a cartoon for the formation of gas hydrate deposits in fold structures, which is based on Figure 6.4 from seismic line BR05-02. The fold structure shows a developed system of extensional faults, which is produced by flexure of the folded strata. The faults crossing the BSR play an important role for the formation of gas hydrate, as they can provide a pathway for the migration of gas from beneath the BSR into the gas hydrate stability zone. When sufficient gas enters the gas hydrate stability zone, the gas will cause the deposition of concentrated gas hydrate deposits. The self-sealing ability

of gas hydrate might decrease the permeability of the sandstone layers and the faults, and thereby create a seal for the gas which would result in accumulation of gas below the BSR. The combination of gas accumulating process and reduction of permeability caused by formation of gas hydrate (sealing) could increase the fluid pressure within fault, which can trigger fault slip (Hornbach et al., 2004). Therefore, we propose that periodic reactivation of these faults as permeable fluid pathways into the hydrate system might be driven by the process of gas accumulation beneath the hydrate layer.

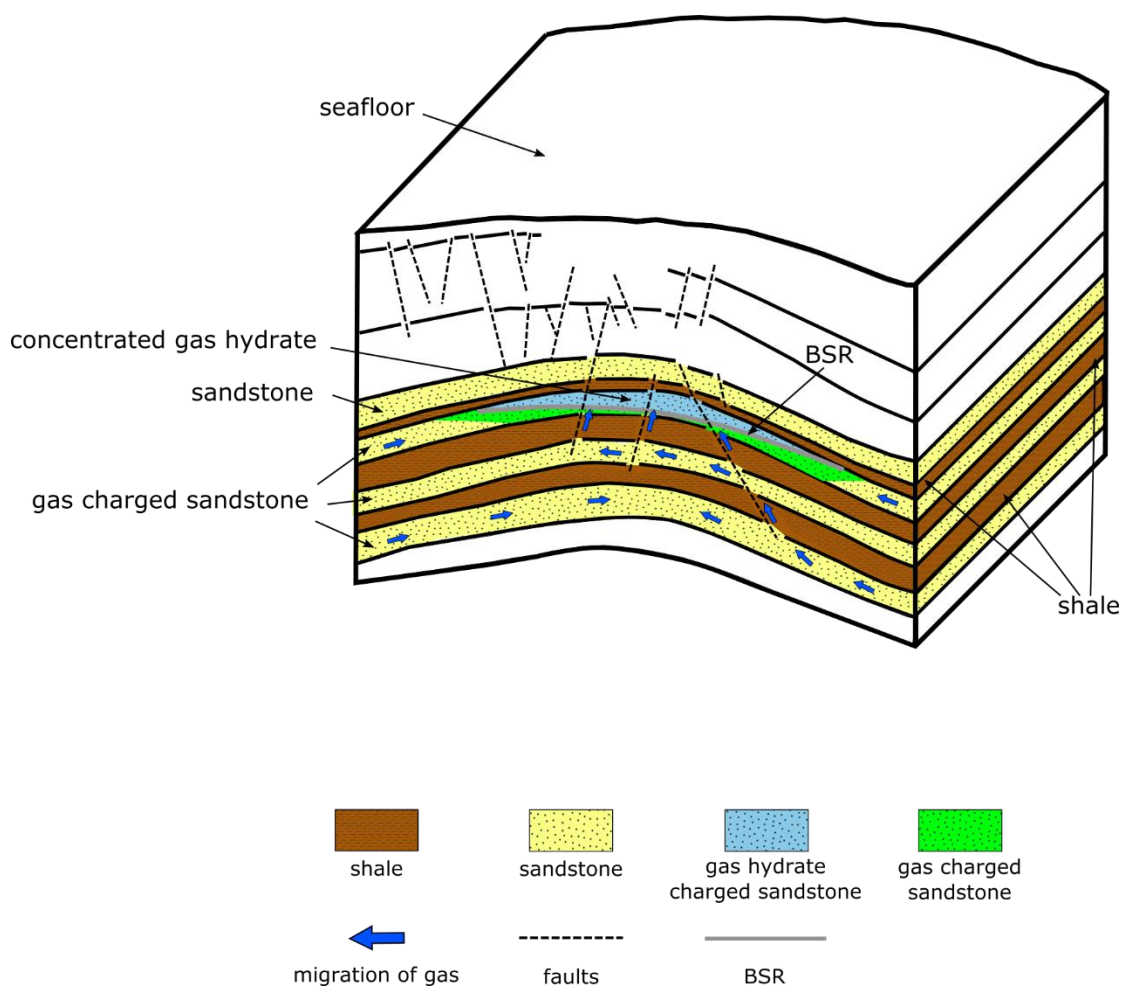


Figure 6.9: Cartoon for the formation of concentrated gas hydrate deposits within folded sediments characterised by flexural extensional faulting (based on observations in Figure 6.4). The diagram shows a fold structure, which is dominated by flexural extension faults. The blue arrows represent the migration of gas along permeable layers (depicted as sandstone layers) and faults (black dashed lines). The grey solid line represents the BSR that is the bottom of gas hydrate stability zone. Gas charged sandstone layers develop beneath the BSR, while layers (possibly sandstones) above the BSR become partially saturated with gas hydrate.

The above discussion described the process for the formation of gas hydrate deposits above the bottom gas hydrate stability zone. However, it raised a question, if the gas hydrate form within the carrier beds and block the flow of further gas, how does the gas migrate through gas hydrate within the stability zone?

Previous study at ODP (Ocean Drilling Program) Site 1249 have provided the evidence for the presence of co-existed free gas with gas hydrate, using PCS (Pressure Core Sampler) (Milkov et al., 2004). Milkov et al. (2004) also proposed a mechanism for high saline water carrying free gas through gas hydrate deposits, as the increased salinity in pore water may prevent gas from dissolving into water. In this case we suggest that the gas may migrate upwards with saline water from deeper sources along dipping strata or faults and form gas hydrate. When mixed fluid (saline water and gas) encountered the pore water with lower salinity, the gas dissolved into water and form gas hydrate deposits. Another explanation for the formation of thick or concentrated gas hydrate deposits could be associated with in-situ biogenic gas. A previous study at ODP Site U1325 presented a model that can match the amount of gas hydrate in sand layers and it suggested the organic matters in sediments is possible to generate sufficient microbial methane for the formation of gas hydrate (Malinverno, 2010).

As the phase of gas hydrate is dynamic, it raised another question: Once the balance of gas hydrate stability is broken, what trap type (dipping strata or structural) is more vulnerable to release gas into water column?

We suggest that the structural traps such as anticlines may be favorable to prevent gas from migrating into water column. In contrast, the trap type of dipping strata that caused by the loss of permeability of rocks within gas hydrate stability zone may be easier to release gas into water column. More specifically, the reduced permeability was caused by the formation of gas hydrate in rocks, but the permeability could regain once the balance of gas hydrate stability is broken, which can lead the melt of gas hydrate. Consequently, the released gas and gas below gas hydrate stability zone might migrate upwards along the dipping strata.

7 CONCLUSIONS

- Our analysis of seismic lines on the southern Hikurangi Margin of New Zealand shows widespread evidence for bottom simulating reflections (BSRs), which are an important geophysical indicator of gas hydrate deposits. We find that BSRs usually occur in locations that are favourable for focusing fluid flow, such as dipping strata and anticline structures. In addition, our results also provide other evidence such as polarity reversals and strong reflections both above and beneath BSRs, to directly or indirectly support the presence of gas hydrate deposits.
- Gas hydrate systems, which are similar to petroleum systems, are discussed in our research. The origin of gas hydrate could be from in-situ biogenic gas or deeper thermogenic gas, or (likely) a combination of both. In terms of thermogenic gas, the source rocks are considered as the Late Cretaceous - Paleocene organic rich mudstones and shales in the Whangai and Waipawa formations. Early Cretaceous marine shales are also considered as potential source rocks. Potential reservoir rocks for hydrate formation are Neogene turbidite sands and Mid-Miocene turbidites, which were encountered by the Titihaoa-1 drill hole.
- Velocity analyses help us to delineate several low velocity zones, which are associated with free gas reservoirs beneath BSRs. We also used the velocity results to identify potentially concentrated gas hydrate deposits, which might be considered as commercially feasible for future exploration. However, we are also aware that some high velocity zones are likely to be caused by lithology rather than concentrated gas hydrate deposits, and it is difficult to discriminate between the two.
- We find faults play an important role for the formation of gas hydrate deposits, as concentrated gas hydrate reservoirs tend to occur preferentially near major thrust faults. We consider that faults crossing BSRs are able to provide a path for the migration of free gas from free gas reservoirs to the gas hydrate stability zone. Therefore, such faults are an important factor in controlling the distribution of

concentrated gas hydrate deposits, and they can be used to explain the localization of gas hydrate deposits.

- In terms of identifying concentrated gas hydrate deposits, we propose the identification of the following seismic attributes: 1) existence of BSRs, 2) strong reflections above BSRs in the gas hydrate stability zone, 3) enhanced reflections below BSRs, 4) appropriate velocity anomalies (i.e. low velocity zones beneath BSRs and localized high-velocity zones above BSRs).
- Lastly, we observed several gas hydrate deposits that are potentially attractive for future economic exploration. A cartoon (Figure 7.1) of four main gas hydrate deposition styles we observed in our research region, and the relevant geophysical features, is presented in Figure 7.1.

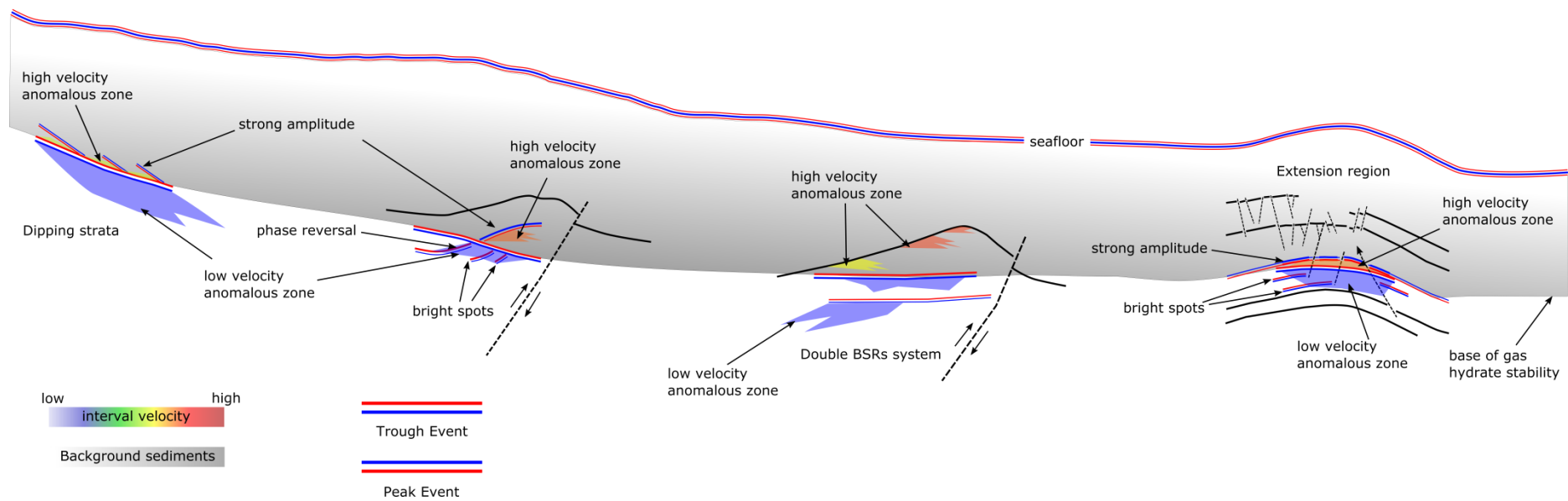


Figure 7.1: The main gas hydrate deposition styles that we identified in our research region and their corresponding seismic expressions. Sketch style adopted after (Boswell et al., 2014).

8 REFERENCE

- Bailleul, J., Robin, C., Chanier, F., Guillocheau, F., Field, B., and Ferriere, J., 2007, Turbidite systems in the inner forearc domain of the Hikurangi convergent margin (New Zealand): New constraints on the development of trench-slope basins: *Journal of Sedimentary Research*, v. 77, no. 3-4, p. 263-283.
- Barnes, P. M., Lamarche, G., Bialas, J., Henrys, S., Pecher, I., Netzeband, G. L., Greinert, J., Mountjoy, J. J., Pedley, K., and Crutchley, G., 2010, Tectonic and geological framework for gas hydrates and cold seeps on the Hikurangi subduction margin, New Zealand: *Marine Geology*, p. 26-48.
- Barnes, P. M., Nicol, A., and Harrison, T., 2002, Late Cenozoic evolution and earthquake potential of an active listric thrust complex above the Hikurangi subduction zone, New Zealand: *Geological Society of America Bulletin*, v. 114, no. 11, p. 1379-1405.
- Beggs, M., 2008, A roadmap for the commercial development of New Zealand's gas hydrate resources: Lower Hutt, New Zealand, GNS Science.
- Berndt, C., Bünz, S., Clayton, T., Mienert, J., and Saunders, M., 2004, Seismic character of bottom simulating reflectors: examples from the mid-Norwegian margin: *Marine and Petroleum Geology*, p. 21(26), 723-733.
- Boswell, R., 2013, Japan completes first offshore methane hydrate production test—Methane successfully produced from deepwater hydrate layers: *Center for Natural Gas and Oil*, v. 412, p. 386-7614.
- Boswell, R., Saeki, T., Shipp, C., Frye, M., Shedd, B., Collett, T., Shelandier, D., and McConnell, D., 2014, Prospecting for Gas Hydrate Resources: Fire in the Ice: *Methane Hydrate Newsletter*, v. 15, no. 2, p. 11.
- Collett, T., Johnson, A., Knapp, G., and Boswell, R., 2009, Natural gas hydrates: energy resource potential and associated geological hazards: *AAPG Memoir*, v. 89.
- Collett, T. S., 2002, Energy resource potential of natural gas hydrates: *Aapg Bulletin*, v. 86, no. 11, p. 1971-1992.
- Crutchley, G. J., 2009, Seismic analysis of gas hydrate "sweet spots" on the Hikurangi Margin [PHD: Otago University].
- Dallimore, S., Collett, T., and Taylor, A., 2005, Scientific results from the Mallik 2002 gas hydrate production research well program, Mackenzie Delta, Northwest Territories, Canada, Geological Survey of Canada Ottawa, Ontario, Canada.
- Davy, B., and Wood, R., 1994, Gravity and Magnetic Modeling of the Hikurangi Plateau: *Marine Geology*, v. 118, no. 1-2, p. 139-151.
- Dillon, W. P., and Max, M. D., 2003, Natural gas hydrate in oceanic and permafrost environments, London, Kluwer.
- Dix, C. H., 1955, Seismic velocities from surface measurements: *Geophysics*, p. 68-86.
- Domenico, S. N., 1977, Elastic properties of unconsolidated porous sand reservoirs: *Geophysics*, p. 42, 1339–1368.

- Finley, P., and Krasen, J., 1989, Basin Analysis, Formation and Stability of Gas Hydrates: Summary; Geological Evolution and Analysis of Confirmed or Suspected Gas Hydrate Localities. Volume 15. US Department of Energy: DOE/MC/21181-1950.
- Fohrmann, M., and Pecher, I. A., 2012, Analysing sand-dominated channel systems for potential gas-hydrate-reservoirs using an AVO seismic inversion technique on the Southern Hikurangi Margin, New Zealand: *Marine and Petroleum Geology*, v. 38, no. 1, p. 19-34.
- Formann, M., and Pecher, A., 2012, Analysing sand-dominated channel systems for potential gas-hydrate-reservoirs using an AVO seismic inversion technique on the Southern Hikurangi Margin, New Zealand: *Marine and Petroleum Geology*, p. 38 (2012) 2019-2034.
- Fugro, 2006, PR 3414: Bruin 2D Seismic Survey.
- Grauls, D., 2001, Gas hydrates: importance and applications in petroleum exploration: *Marine and Petroleum Geology*, v. 18, no. 4, p. 519-523.
- Hammerschmidt, E., 1934, Formation of gas hydrates in natural gas transmission lines: *Industrial & Engineering Chemistry*, v. 26, no. 8, p. 851-855.
- Haq, B. U., 2000, Natural Gas Hydrate in Oceanic and Permafrost Environments, in Max, M., ed., *Climate impact of Natural Gas Hydrate*. : Washington, DC, Kluwer Academic Publisher.
- Henry, A. S., Woodward, D., and Pecher, A. I., 2009, Variation of bottom-simulating reflector (BSR) strength in a high-flux methane province, Hikurangi margin, New Zealand, In: Collett, T., Johnson, A., Knapp, C., Boswell, R. (Eds.), *Natural Gas Hydrates: Energy Resource Potential and Associated Geologic Hazards*. AAPG Special Publication.
- Holbrook, W. S., Gorman, A. R., Hornbach, M., Hackwith, K. L., Nealon, J., Lizarralde, D., and Pecher, I. A., 2002, Seismic detection of marine methane hydrate: The Leading Edge, p. 21, 686-689.
- Hornbach, M. J., Holbrook, W. S., Gorman, A. R., Hackwith, K. L., Lizarralde, D., and Pecher, I., 2003, Direct seismic detection of methane hydrate on the Blake Ridge: *Geophysics*, v. 68, no. 1, p. 92-100.
- Hornbach, M. J., Saffer, D. M., and Holbrook, W. S., 2004, Critically pressured free-gas reservoirs below gas-hydrate provinces: *Nature*, v. 427, no. 6970, p. 142-144.
- Hyndman, R. D., and Davis, E. E., 1992, A mechanism for the formation of methane hydrate and seafloor bottom - simulating reflectors by vertical fluid expulsion: *Journal of Geophysical Research: Solid Earth*, v. 97, no. B5, p. 7025-7041.
- Kennett, J. P., Cannariato, K. G., Hendy, I. L., and Behl, R. J., 2003, BOOK TOOLS.
- Khan, K. A., and Akhter, G., 2011, Work flow shown to develop useful seismic velocity models: *Oil and Gas Journal*, p. 109(116), 152-161.
- King, G. C., Stein, R. S., and Lin, J., 1994, Static stress changes and the triggering of earthquakes: *Bulletin of the Seismological Society of America*, v. 84, no. 3, p. 935-953.

- Klauda, J. B., and Sandler, S. I., 2005, Global distribution of methane hydrate in ocean sediment: *Energy & Fuels*, v. 19, no. 2, p. 459-470.
- Kroeger, K. F., Plaza-Faverola, A., Barnes, P. M., & Pecher, I. A., 2015, Thermal evolution of the New Zealand Hikurangi subduction margin: Impact on natural gas generation and methane hydrate formation—A model study: *Marine and Petroleum Geology*, p. 63, 97-114.
- Kvenvolden, K. A., 1993, Gas hydrates—geological perspective and global change, *Reviews of Geophysics*, p. 31(32), 173-187.
- Kvenvolden, K. A., Carlson, P. R., Warden, A., and Threlkeld, C. N., 1998, Carbon isotopic comparisons of oil products used in the developmental history of Alaska: *Chemical Geology*, v. 152, no. 1-2, p. 73-84.
- Kvenvolden, K. A., and Rogers, B. W., 2005, Gaia's breath - global methane exhalations: *Marine and Petroleum Geology*, v. 22, no. 4, p. 579-590.
- Lee, M. W., and Dillon, W. P., 2001, Amplitude blanking related to the pore-filling of gas hydrate in sediments: *Marine Geophysical Researches*, v. 22, no. 2, p. 101-109.
- Lelieveld, J., Crutzen, P. J., and Dentener, F. J., 1998, Changing concentration, lifetime and climate forcing of atmospheric methane: *Tellus B*, v. 50, no. 2, p. 128-150.
- Lewis, K., and Pettinga, J., 1993, The emerging, imbricate frontal wedge of the Hikurangi margin: *Sedimentary basins of the world*, v. 2, p. 225-250.
- Lewis, K. B., and Barnes, P. L., 1999, Kaikoura Canyon, New Zealand: active conduit from near-shore sediment zones to trench-axis channel: *Marine Geology*, v. 162, no. 1, p. 39-69.
- Lewis, K. B., Collot, J. Y., and Lallemand, S. E., 1998, The dammed Hikurangi Trough: a channel-fed trench blocked by subducting seamounts and their wake avalanches (New Zealand-France GeodyNZ Project): *Basin Research*, v. 10, no. 4, p. 441-468.
- Macmahon, J., Pecher, I., Crutchley, G., Mountjoy, J., Krastel, S., and Henrys, S., 2015, Quantitative seismic analysis of double-BSRs on the Hikurangi Margin, *Advantage*.
- Makogon, I. U. r. F., 1981, Hydrates of natural gas.
- Malinverno, A., 2010, Marine gas hydrates in thin sand layers that soak up microbial methane: *Earth and Planetary Science Letters*, v. 292, no. 3, p. 399-408.
- Mestdagh, T., 2015, Evaluation and modelling of the response of gas hydrate reservoirs to changing environmental conditions across a high-latitude continental margin [Master: Ghent University].
- Milkov, A. V., 2004, Global estimates of hydrate-bound gas in marine sediments: how much is really out there?: *Earth-Science Reviews*, v. 66, no. 3-4, p. 183-197.
- Milkov, A. V., Dickens, G. R., Claypool, G. E., Lee, Y.-J., Borowski, W. S., Torres, M. E., Xu, W., Tomaru, H., Tréhu, A. M., and Schultheiss, P., 2004, Co-existence of gas hydrate, free gas, and brine within the regional gas hydrate stability zone at Hydrate Ridge (Oregon margin): evidence from prolonged degassing of a pressurized core: *Earth and Planetary Science Letters*, v. 222, no. 3, p. 829-843.

- Nicol, A., and Beavan, J., 2003, Shortening of an overriding plate and its implications for slip on a subduction thrust, central Hikurangi Margin, New Zealand: *Tectonics*, v. 22, no. 6.
- Nicol, A., Mazengarb, C., Chanier, F., Rait, G., Uruski, C., and Wallace, L., 2007, Tectonic evolution of the active Hikurangi subduction margin, New Zealand, since the Oligocene: *Tectonics*, v. 26, no. 4.
- Paull, C., Ussler III, W., and Borowski, W., 1993, Sources of biogenic methane to form marine gas hydrates: In situ production or upward migration?: North Carolina Univ., Chapel Hill, NC (United States).
- Pecher, I., Henrys, S., Ellis, S., Chiswell, S., and Kukowski, N., 2005, Erosion of the seafloor at the top of the gas hydrate stability zone on the Hikurangi Margin, New Zealand: *Geophysical Research Letters*, v. 32, no. 24.
- Pecher, I. A., and Henrys, S. A., 2003, Potential gas reserves in gas hydrate sweet spots on the Hikurangi Margin, New Zealand: Institute of Geological and Nuclear Sciences.
- Pecher, I. A., Henrys, S. A., Wood, W. T., Kukowski, N., Crutchley, G. J., Fohrmann, M., Kilner, J., and Faure, K., 2010, Focussed fluid flow on the Hikurangi Margin, New Zealand - Evidence from possible local upwarping of the base of gas hydrate stability: *Marine Geology*, p. 99-113.
- Reddi, S. I., 2001, Reprocessing of multi-channel seismic data of ONGC for gas hydrate exploration part II, NGRI Technical Report.
- Reshef, M., and Rüger, A., 2008, Influence of structural dip angles on interval velocity analysis: *Geophysics*, v. 73, no. 4, p. U13-U18.
- Rogers, K. M., Collen, J. D., Johnston, J. H., and Elgar, N. E., 1999, A geochemical appraisal of oil seeps from the East Coast Basin, New Zealand: *Organic geochemistry*, v. 30, no. 7, p. 593-605.
- Sassen, R., and MacDonald, I. R., 1994, Evidence of structure H hydrate, Gulf of Mexico continental slope: *Organic Geochemistry*, v. 22, no. 6, p. 1029-1032.
- Sassen, R., Sweet, S. T., Milkov, A. V., DeFreitas, D. A., and Kennicutt, M. C., 2001, Thermogenic vent gas and gas hydrate in the Gulf of Mexico slope: Is gas hydrate decomposition significant?: *Geology*, v. 29, no. 2, p. 107-110.
- Schoderbek, D., Farrell, H., Hester, K., Howard, J., Raterman, K., Silpnargmlert, S., Martin, K., Smith, B., and Klein, P., 2013, ConocoPhillips gas hydrate production test final technical report: in, United States Department of Energy.
- Shipley, T. H., 1979, Seismic evidence for widespread possible gas hydrate horizons on continental slopes and rises: *American Association of Petroleum Geologists*, p. 63(12), 2204-2213.
- Shuey, R., 1985, A simplification of the Zoeppritz equations: *Geophysics*, v. 50, no. 4, p. 609-614.
- Sloan, E. D., 1998, Physical/chemical properties of gas hydrates and application to world margin stability and climate change: *Geological Society of London Special Publications*, 137, 31-50.
- Sloan, E. D., 2003, Fundamental principles and applications of natural gas hydrates: *Nature*, v. 426, no. 6964, p. 353-359.

- Stern, T., Stratford, W., and Salmon, M., 2006, Subduction evolution and mantle dynamics at a continental margin: Central North Island, New Zealand: *Reviews of Geophysics*, v. 44, no. 4.
- Sultan, N., Cochonat, P., Canals, M., Cattaneo, A., Dennielou, B., Haffidason, H., Laberg, J. S., Long, D., Mienert, J., Trincardi, F., Urgeles, R., Vorren, T. O., and Wilson, C., 2004, Triggering mechanisms of slope instability processes and sediment failures on continental margins: a geotechnical approach: *Marine Geology*, v. 213, no. 1-4, p. 291-321.
- Sultan, N., Voisset, M., Marsset, T., Vernant, A. M., Cauquil, E., Colliat, J. L., and Curinier, V., 2007, Detection of free gas and gas hydrate based on 3D seismic data and cone penetration testing: An example from the Nigerian Continental Slope: *Marine Geology*, v. 240, no. 1-4, p. 235-255.
- Swinkels, W. J. A. M., and Drenth, R. J. J., 2000, Thermal Reservoir Simulation Model of Production From Naturally Occurring Gas Hydrate Accumulations: *SPE Reservoir Evaluation & Engineering*, v. 3, no. 06.
- Thakur, N. K., and Rajput, S., 2011, *Exploration of Gas Hydrates*, Springer.
- Uruski, C., and Bland, K., 2011, Pegasus basin and the prospects for oil and gas: Ministry of Economic Development New Zealand unpublished Petroleum Report PR4326.
- USDE, 2011, *Energy Resource Potential of Methane Hydrate*: Washington, DC, USA, United State Department of Energy.
- Wood, W. T., Gettrust, J. F., Chapman, N. R., Spence, G. D., and Hyndman, R. D., 2002, Decreased stability of methane hydrates in marine sediments owing to phase-boundary roughness: *Nature*, v. 420, no. 6916, p. 656-660.
- Wood, W. T., and Ruppel, C., 2000, Seismic and thermal investigation of the Blake Ridge gas hydrate, *Proceedings of the Ocean Drilling Program, Scientific Results*.
- Xu, W. Y., and Germanovich, L. N., 2006, Excess pore pressure resulting from methane hydrate dissociation in marine sediments: A theoretical approach: *Journal of Geophysical Research-Solid Earth*, v. 111, no. B1.
- Yamamoto, 2013, Japan completes first offshore methane hydrate production test - methane successfully produced from deepwater hydrate layers: *Fire in the ice*: Department of Energy, Office of Fossil Energy, National Energy Technology Laboratory, *Methane Hydrate News Letter*, p. 1-2.
- Yilmaz, O., 2001, *Seismic Data Analysis: Processing, Inversio, and Interpretation of Seismic Data*: 2nd Edn, Tulsa, Society of Exploration Geophysicists.
- Zhang, W., Durham, W., Stern, L., and Kirby, S., 1999, Experimental deformation of methane hydrate: New results: *Eos Trans. AGU*, v. 80, p. 17.